

**Upconversion Quantum Yield and Luminescence  
of  $\beta$ -NaYF<sub>4</sub>:Yb<sup>3+</sup>,Er<sup>3+</sup> Nanoparticles:  
Influence of Environment and Dopant Concentration**

vorgelegt von  
Diplom-Physiker  
Martin Kaiser

von der Fakultät II – Mathematik und Naturwissenschaften  
der Technischen Universität Berlin

zur Erlangung des akademischen Grades  
Doktor der Naturwissenschaften  
– Dr. rer. nat. –

genehmigte Dissertation

Promotionsausschuss:

Vorsitzende: Prof. Dr. Ulrike Woggon

Gutachter: Prof. Dr. Axel Hoffmann

Gutachter: Prof. Dr. Oliver Benson

Gutachterin: Dr. Ute Resch-Genger

Tag der wissenschaftlichen Aussprache: 16.12.2020

Berlin 2021

This thesis is dedicated to my daughter, Sophie Kaiser.

*"Science is the process that takes us from confusion to understanding."*

**Brian Greene**

---

# Abstract

Lanthanide-based upconversion (UC) nanometer (nm)-sized particles (UCNPs) exhibit the unique ability to emit one higher-energy photon after the sequential absorption of two or more near-infrared (NIR) photons. This UC luminescence (UCL) makes UCNPs very attractive for the use as optical probes in the biomedical area. In this respect, the main advantages of UCNPs are the suppression of environment-based background fluorescence as well as their excitability with NIR-light allowing imaging applications in deep tissue layers of several centimeters (cm).

The future progress in the development of brightly-luminescent UCNPs requires reliable quantification methods of their optical properties to ensure comparability on an international level. For this purpose, in the first study of this thesis an integrating sphere setup (ISS), as well as corresponding relevant guidelines for the measurement conditions, has been developed enabling the absolute determination of the key parameter upconversion quantum yield  $\Phi_{UC}$  with minimum uncertainty ( $\Phi_{UC} :=$  ratio of emitted high-energy photons to absorbed low-energy photons). The main features of the developed ISS setup present the wide tunability of  $P$  of over four orders of magnitude and a high linear detection range of over 10 orders of magnitude allowing the comprehensive characterization of the nonlinear luminescence behavior of UC materials. As the main subject of the investigations of this thesis served a UC system based on a transparent host lattice  $\beta$ -NaYF<sub>4</sub>, which was doped with trivalent ytterbium ions (Yb<sup>3+</sup>), acting as absorber/antenna, and trivalent erbium ions (Er<sup>3+</sup>), acting as emitter. The suppression of radiationless deactivation processes *via* the particle surface presents a major challenge in the development of brightly-luminescent UCNPs. In order to quantify the luminescence quenching of UCNPs, commercial  $\mu$ m-sized  $\beta$ -NaYF<sub>4</sub>:Yb<sup>3+</sup>(21%),Er<sup>3+</sup>(2%) particles (UC $\mu$ P), with particle diameters large enough to neglect surface effects, were comprehensively optically characterized. In this respect, a maximal absolute  $\Phi_{UC}$  of 10.5% at  $P = 30 \text{ Wcm}^{-2}$ , considering the spectral region from 360 - 900 nm, was measured for these UC $\mu$ P.

New detailed insights of the UC processes of  $\beta$ -NaYF<sub>4</sub>:Yb<sup>3+</sup>,Er<sup>3+</sup> UCNPs were gained in the second and third study by the investigation of high-quality UCNPs sample series with systematical varied parameters. These UCNPs sample series were optically characterized regarding their  $P$ -dependent  $\Phi_{UC}$  and UCL of the different Er<sup>3+</sup> emission bands as well as of the decay behavior of the intensity of the Er<sup>3+</sup> and Yb<sup>3+</sup> emission bands. The computer-assisted simulation of these experimental data by utilizing a coupled rate equation system turned out to be a powerful tool to underpin the photophysical interpretations. A special

---

highlight of this advanced analysis represents the clarification of the conditions for the controversially debated bi- and triphotonic population pathways of the red-emitting  $\text{Er}^{3+} {}^4\text{F}_{9/2}$  energy level. In the following, the main results of these studies are briefly presented.

The second study deals with 23 nm-sized UCNPs with different surrounding environments, its interaction with the particle surface, and the accompanied influence on the UC processes. A main conclusion of this study points out that for UCNPs dispersed in water ( $\text{H}_2\text{O}$ ), at low  $P$ , the  $\text{Er}^{3+} {}^4\text{F}_{9/2}$  energy level is populated biphotonically by a nonresonant  $\text{Yb}^{3+}$ - $\text{Er}^{3+}$  energy transfer (ET) from the low energetic  $\text{Er}^{3+} {}^4\text{I}_{13/2}$  energy level. Thereby, the high population density of the low  $\text{Er}^{3+}$  energy levels is favored due to the coupling of excited  $\text{Er}^{3+}$  ions near the UCNPs particle surface with the O-H vibrational modes of the  $\text{H}_2\text{O}$  molecules. However, the use of very high  $P$  of ca.  $1 \text{ kWcm}^{-2}$  compensates  $\text{H}_2\text{O}$ -induced increase of nonradiative relaxation rates, and consequently, leads to moderately high  $\Phi_{\text{UC}}$  of about 0.5% with a mainly triphotonic activation of the  $\text{Er}^{3+} {}^4\text{F}_{9/2}$  energy level for the UCNPs dispersed in  $\text{H}_2\text{O}$ .

In the third study, the optical properties of 33 nm-sized UCNPs dispersed in toluene as function of the ion-ion distances were investigated. These distances can be directly tuned by variation of the  $\text{Yb}^{3+}$  and the  $\text{Er}^{3+}$  dopant concentrations. In this respect, it was demonstrated that the increase of the  $\text{Yb}^{3+}$  dopant concentration causes an enhancement of the triphotonic activation of the red-emitting  $\text{Er}^{3+} {}^4\text{F}_{9/2}$  energy level. This effect is induced by an increased back energy transfer from  $\text{Er}^{3+}$  to  $\text{Yb}^{3+}$  due to the reduction of the  $\text{Er}^{3+}$ - $\text{Yb}^{3+}$ -distance. Although the  $\Phi_{\text{UC}}$  is reduced by a faster energy migration to the UCNP surface, the overall UCL intensity was overcompensated due to the higher number of absorbing  $\text{Yb}^{3+}$  ions. However, the increase of the  $\text{Er}^{3+}$  concentration resulted in different trends of the relative  $\text{Er}^{3+}$  red emission intensity. The intensity increase, observed at low  $P$ , was attributed to increased biphotonic activation by enhanced nonradiative relaxation of the green-emitting  $\text{Er}^{3+} {}^2\text{H}_{11/2}/{}^4\text{S}_{3/2}$ . Contrary to that, at high  $P$ , the  $\text{Er}^{3+}$  red emission intensity diminishes when the  $\text{Er}^{3+}$  concentration increases. Consequently, a rate equation analysis revealed that this UCL behavior is a sign of a yet unknown depopulation rate.

---

# Zusammenfassung

Lanthanid-basierte upconversion (UC) (oder aufkonvertierende) Nanopartikel (UCNPs) besitzen die spezielle Eigenschaft nach der sequentiellen Absorption von zwei oder mehreren nahinfraroten (NIR) Photonen ein höherenergetisches Photon zu emittieren. Diese UC Lumineszenz (UCL) macht UCNPs sehr attraktiv für den Einsatz als optische Nanosensoren im biomedizinischen Bereich. Hierbei sind die Hauptvorteile von UCNPs die Vermeidung von umgebungsbedingter Hintergrundfluoreszenz sowie deren Anregbarkeit mit NIR-Licht, die bildgebende Verfahren in tieferen Gewebeschichten von mehreren Zentimetern (cm) erlaubt.

Der weitere Fortschritt in der Entwicklung von hell-lumineszierenden UCNPs erfordert die verlässliche Quantifizierung ihrer optischen Eigenschaften um die Vergleichbarkeit auf internationaler Ebene zu gewährleisten. Zu diesem Zweck wurde in der ersten Studie dieser Doktorarbeit ein Ulbrichtkugelaufbau (ISS) sowie relevante Richtlinien für die Messbedingungen entwickelt, die die absolute Bestimmung des Schlüsselparameters upconversion Quantenausbeute ( $\Phi_{UC}$ ) mit minimaler Unsicherheit ermöglichen ( $\Phi_{UC} :=$  Verhältnis von emittierten hochenergetischen Photonen zu absorbierten niederenergetischen Photonen). Die Hauptbesonderheiten dieses ISS Aufbaus sind die weite Durchstimbarkeit der  $P$  über vier Größenordnungen und der große lineare Detektionsbereich von über 10 Größenordnungen, die eine umfassende Charakterisierung des nichtlinearen Lumineszenzverhaltens von UC Materialien gewährleistet. Als Hauptgegenstand dieser Arbeit diente ein UC System basierend auf einem transparenten Wirtskristall  $\beta$ -NaYF<sub>4</sub>, der mit trivalenten Ytterbium-Ionen (Yb<sup>3+</sup>), fungieren als Antenne/Absorber, und trivalenten Erbium-Ionen (Er<sup>3+</sup>), fungieren als Emitter, dotiert ist. Die Vermeidung strahlungsloser Deaktivierungsprozesse über die Partikeloberfläche gilt als einer der größten Herausforderungen in der Entwicklung von hell-leuchtenden UCNPs. Zur Quantifizierung solcher Lumineszenzlöscheffekte von UCNPs wurden kommerzielle  $\mu$ m-große  $\beta$ -NaYF<sub>4</sub>:Yb<sup>3+</sup>(21%),Er<sup>3+</sup>(2%) Partikel (UC $\mu$ P), deren Partikeldurchmesser hinreichend groß ist um Oberflächeneffekte zu vernachlässigen, umfassend optisch charakterisiert. In dieser Hinsicht, wurde für diese UC $\mu$ P eine maximale  $\Phi_{UC}$  von 10.5% bei  $P = 30 \text{ Wcm}^{-2}$  im spektralen Bereich von 360 nm - 900 nm absolut gemessen.

Neue detaillierte Erkenntnisse über die UC Prozesse von  $\beta$ -NaYF<sub>4</sub>:Yb<sup>3+</sup>,Er<sup>3+</sup> UCNPs wurden in der zweiten und dritten Studie anhand von hochqualitativen Probenserien mit systematischen variierten Parametern erlangt. Diese UCNPs Probenserien wurden

hinsichtlich der  $P$ -abhängigen  $\Phi_{UC}$  und UCL der verschiedenen  $Er^{3+}$  Emissionsbanden sowie des Abklingverhaltens der Intensität von den  $Er^{3+}$  und  $Yb^{3+}$  Emissionsbanden untersucht. Die computerunterstützte Simulation der gewonnenen experimentellen Daten mittels eines gekoppelten Ratengleichungssystems erwies sich als ein mächtiges Werkzeug für die Untermauerung der photophysikalischen Interpretationen. Ein besonderes Highlight dieser fortschrittlichen Analyse präsentiert die Klärung der Bedingungen für die kontrovers diskutierten bi- und triphotonischen Populationswege für das rot emittierende  $Er^{3+} {}^4F_{9/2}$  Energielevel. Im Folgenden sind die Hauptergebnisse dieser Studien kurz dargestellt.

Die zweite Studie beschäftigt sich mit 23 nm-großen UCNPs in verschiedenen Partikelumgebungen, sowie dessen Interaktion mit der Partikeloberfläche und den hiermit verbundenen Einfluss auf die UC Prozesse. Eine Hauptergebnis dieser Studie zeigt auf, dass für UCNPs dispergiert in Wasser ( $H_2O$ ) das rot emittierenden  $Er^{3+} {}^4F_{9/2}$  Energielevel bei niedriger  $P$  hauptsächlich biphotonisch über einen nichtresonanten  $Yb^{3+}$  -  $Er^{3+}$  Energietransfer (ET) vom niederenergetischen  $Er^{3+} {}^4I_{13/2}$  Energielevel bevölkert wird. Hierbei wird die hohe Population der niederenergetischen  $Er^{3+}$  Energielevel durch die Kopplung von oberflächennahen angeregten  $Er^{3+}$ -Ionen mit den O-H Vibrationsmoden der  $H_2O$  Moleküle begünstigt. Indessen kompensierte die Verwendung von hohen  $P$  von ca.  $1 \text{ KWcm}^{-2}$  die  $H_2O$ -induzierten Löschraten, wodurch für die UCNPs dispergiert in  $H_2O$  eine mäßig hohe  $\Phi_{UC}$  von 0.5% sowie hauptsächlich triphotonischen Aktivierung des  $Er^{3+} {}^4F_{9/2}$  Energielevels erreicht wird.

In der dritten Studie wurden die optischen Eigenschaften von 33 nm-großen UCNPs dispergiert in Toluol in Abhängigkeit der mittleren Ionenabstände untersucht. Diese Abstände wurden über die Variation der  $Yb^{3+}$  und der  $Er^{3+}$  Dotierkonzentration durchgestimmt. In dieser Hinsicht wurde demonstriert, dass die Erhöhung der  $Yb^{3+}$  Konzentrationen zu einer Verstärkung der triphotonischen Aktivierung des rot emittierenden  $Er^{3+} {}^4F_{9/2}$  Energielevel führt. Dieser Effekt ist auf einen verstärkten Energierücktransfer vom  $Er^{3+}$  zum  $Yb^{3+}$ , aufgrund der Verringerung des  $Er^{3+}$ - $Yb^{3+}$  Abstandes, zurückzuführen. Indessen führte die Erhöhung der  $Er^{3+}$  Konzentration zu verschiedenen Trends für die relative Intensität der roten  $Er^{3+}$  Emissionsbande. Die Intensitätserhöhung bei Anregung mit geringer  $P$  konnte auf die Verstärkung der nichtstrahlenden Rate des grün emittierenden  $Er^{3+} {}^2H_{11/2}/{}^4S_{3/2}$  Energielevels zurückgeführt werden. Konträr dazu verringerte sich bei Anregung mit hoher  $P$  die relative rote  $Er^{3+}$  Emissionsintensität mit steigender  $Er^{3+}$  Konzentration. Die Ratengleichungsanalyse zeigt auf, dass dieses UCL-Verhalten ein Indiz für eine bisher unbekannte Depopulationsrate ist.

---

# List of Publications for this Cumulative Thesis

This cumulative thesis is based on the following publications, which are referred by capital roman numerals:

- I. M. Kaiser, C. Würth, M. Kraft, I. Hyppänen, T. Soukka, U. Resch-Genger  
**„Power-dependent upconversion quantum yield of NaYF<sub>4</sub>: Yb<sup>3+</sup>, Er<sup>3+</sup> nano-and micrometer-sized particles – measurements and simulations“**  
*Nanoscale*, **2017**, 9, 10051-10058  
DOI: 10.1039/C7NR02449E
  
- II. C. Würth\*, M. Kaiser\*, S. Wilhelm, B. Grauel, T. Hirsch, U. Resch-Genger  
**„Excitation power dependent population pathways and absolute quantum yields of upconversion nanoparticles in different solvents“**  
*Nanoscale*, **2017**, 9, 4283-4294  
DOI: 10.1039/C7NR00092H  
\*equally contributed
  
- III. M. Kaiser, C. Würth, M. Kraft, T. Soukka, U. Resch-Genger  
**“Explaining the influence of dopant concentration and excitation power density on the luminescence and brightness of  $\beta$ -NaYF<sub>4</sub>:Yb<sup>3+</sup>,Er<sup>3+</sup> nanoparticles: Measurements and simulations”**  
*Nanoresearch*, **2019**, 12, 1871-1879  
DOI: 10.1007/s12274-019-2450-4

Content of these publications have been reproduced with the permission of the copyright holder

---

# Contents

<b>Abstract .....</b>	<b>i</b>
<b>Zusammenfassung .....</b>	<b>iii</b>
<b>List of Publications for this Cumulative Thesis .....</b>	<b>v</b>
<b>Contents .....</b>	<b>vi</b>
<b>1 Introduction .....</b>	<b>1</b>
1.1 Aims and outline of this cumulative thesis .....	4
<b>2 Fundamentals .....</b>	<b>7</b>
2.1 Upconversion (UC) processes .....	7
2.2 Energy transfer (ET) processes between $\text{Ln}^{3+}$ ions .....	9
2.3 Energy transfer upconversion (ETU)-based materials .....	12
2.3.1 Luminescent centers – sensitizer and activator ions .....	12
2.3.2 Host lattice .....	13
2.4 Upconversion luminescence (UCL) of $\beta\text{-NaYF}_4\text{:Yb}^{3+},\text{Er}^{3+}$ crystals.....	15
2.5 Upconversion luminescence quantum yield ( $\Phi_{\text{UC}}$ ) .....	18
<b>3 Reviews of Literature and Open Questions .....</b>	<b>21</b>
3.1 Absolute $\Phi_{\text{UC}}$ measurements .....	21
3.2 Solvent-dependent luminescence quenching .....	22
3.3 Dopant concentration-dependent color tuning .....	23
<b>4. Samples and Experimental Methods .....</b>	<b>25</b>
4.1 Overview of investigated $\beta\text{-NaYF}_4\text{:Yb}^{3+},\text{Er}^{3+}$ samples .....	25
4.2 Optical characterization methods .....	27
4.2.1 Integrating sphere setup (ISS) .....	28
4.2.2 Time-resolved photoluminescence spectroscopy .....	36



## Contents

---

<b>5 Measurement Strategies for the <math>P</math>-dependent <math>\Phi_{UC}</math> (<math>\Phi_{UC}(P)</math>).....</b>	<b>39</b>
5.1 Measurement conditions for $\Phi_{UC}(P)$ .....	39
5.2 Validation of measured $\Phi_{UC}(P)$ by comparison with literature data .....	46
5.2.1 Validation by comparison with measured results from Page et al. ....	47
5.2.1 Validation by comparison with measured results from the van Veggel group	48
5.2.3 Validation by comparison with simulated results from the Berry group .....	48
5.3 Conclusions of chapter 5 .....	50
 <b>6 Solvent-Dependent Optical Properties of <math>\beta</math>-NaYF<sub>4</sub>:Yb<sup>3+</sup>,Er<sup>3+</sup> UCNP</b> s .....	<b>51</b>
6.1 Solvent-dependent upconversion quantum yield ( $\Phi_{UC}$ ) .....	51
6.2 Emission color of UCNP dispersed in D <sub>2</sub> O and H <sub>2</sub> O.....	52
6.3 Conclusions of chapter 6 .....	56
 <b>7 Dopant Concentration-Dependent Optical Properties of <math>\beta</math>-NaYF<sub>4</sub>:Yb<sup>3+</sup>,Er<sup>3+</sup> UCNP</b> s .....	<b>57</b>
7.1 Dopant concentration-dependent upconversion luminescence (UCL) .....	57
7.2 Influence of the dopant concentrations on rate equation constants .....	60
7.3 Conclusions of chapter 7 .....	63
 <b>8 General Conclusions for Publications .....</b>	<b>64</b>
 <b>Appendix .....</b>	<b>I</b>
List of Abbreviations .....	I
Bibliography .....	III
List of Publications .....	XII
Conference Talks and Posters .....	XVI
Acknowledgement .....	XVIII
Contributions to the Manuscripts .....	XX

---

---

---

# 1 Introduction

Optical probes are increasingly used in biomedical research to visualize, characterize and quantify processes on cellular and subcellular levels. Such probes enable localized measurements of pH, polarity, viscosity, and the detection of disease-related biomarkers.<sup>1-4</sup> The most extensively investigated and applied chromophores for the design of optical probes are fluorescent organic dyes and colloidal semiconductor nanocrystals called quantum dots (QDs).<sup>5-7</sup> Organic dyes and QDs stand out for their excellent brightness resulting from a) a high photon absorption cross-section [ $\text{cm}^2$ ], which is a measure of the probability of an incoming photon being absorbed, and b) a high photoluminescence quantum yield ( $\Phi$ ), defined as ratio of emitted photons to absorbed photons.<sup>5</sup> Organic dyes exhibit unsymmetrical-shaped emission bands and a mirrored-shifted absorption band, see Figure 1.1. The emission process stems from optical transitions, which either are localized over the whole molecule or from an intramolecular charge transfer, i.e. that electron is transferred from one part to another part of the dye molecule.<sup>5, 8</sup> QDs have a Gaussian-shaped emission band resulting from the recombination of electron-hole pairs called excitons, which are produced by the absorption of photons with energies larger than the QDs bandgap energy. The absorptivity of QDs increases with decreasing wavelength offering a variable choice of the excitation wavelength, in contrast to organic dyes, see Figure 1.1.<sup>5</sup> The emission and absorption properties of QDs are mainly characterized by their material composition, the particle size, and size distribution. Thereby, the decrease of the QDs emission wavelength with shrinking diameter, known as quantum size effect, arises when the QDs diameter (typically a few nanometers) is comparable or smaller than the material-specific exciton Bohr radius equaling the distance of its electron-hole pairs.<sup>9, 10</sup>

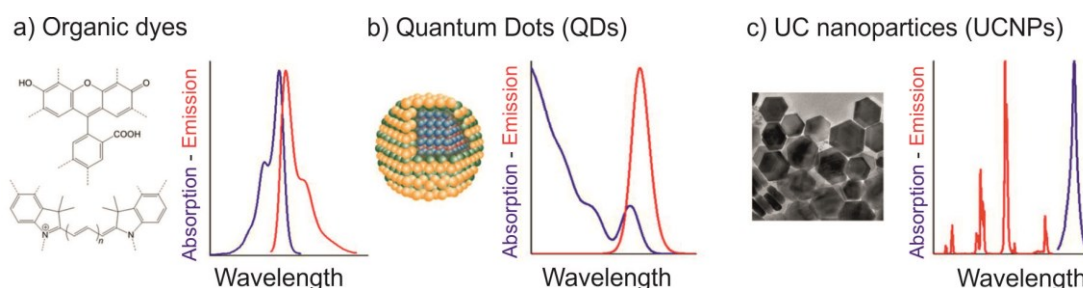


**Figure 1.1 Overview of a typical structure, emission band, and absorption band of a) Organic dyes, b) QDs, and c) UCNPs.** Reproduced from Würth et al.<sup>11</sup> with permission from Springer Nature.

## 1 Introduction

---

Despite the great success of these emitters in biomedical applications, their potential is still hampered due to the lack of stable, efficient near-infrared (NIR) emissive organic dyes and QDs.<sup>12</sup> Therefore, the common impairments of visible (vis) light emitting optical probes, including scattering, absorption, and background fluorescence of surrounding biological matrices, are restricting their scope of applications, e.g. the use in deep tissue imaging. A further critical issue of organic dyes concern their low photostability, i.e. that they bleach after long-term irradiation, which is very problematic for single particle tracking or long-term studies in a medium or in living cells. Although QDs exhibit a high photostability, their blinking behavior, i.e. that they can spontaneously switch from being emissive to a dark state, is particularly undesirable for single particle tracking applications. Furthermore, the assessment of the toxicity of these materials for *in vitro* and *in vivo* studies is an ongoing controversial topic. In this respect, dyes have been widely characterized showing cytotoxicity levels varying from low to very high.<sup>5</sup> QDs, typically consisting of toxic heavy metals (e.g. Cd<sup>2+</sup>, Hg<sup>2+</sup>, Zn<sup>2+</sup>, Pb<sup>2+</sup>), require a very stable surface chemistry as surface cover.<sup>7, 13, 14</sup> However, their nanotoxicological effects, i.e. that they may accumulate inside cells and damage them as well as a potentially high surface reactivity, are still not properly understood.

Trivalent lanthanide-(Ln<sup>3+</sup>)-based upconversion (UC) nanoparticles (UCNPs) are an emerging class of optical probes with a high potential of outperforming fluorescent dyes and QDs in many application areas.<sup>15-31</sup> UCNPs already demonstrated promising results as contrast agent for deep tissue super-resolution imaging and spectroscopy,<sup>32, 33</sup> as an optical switch to control mouse brain activity<sup>34</sup> in the optogenetics research area, and as active media for micro-cavity lasers<sup>35</sup> with ultra-low threshold down to 30 Wcm<sup>-2</sup>. The most efficient UCNPs materials are based on a combination of energy harvesting Ln<sup>3+</sup> ions called sensitizer ions (e.g. Yb<sup>3+</sup>, Nd<sup>3+</sup>) and emitting Ln<sup>3+</sup> ions called activator ions (e.g. Er<sup>3+</sup>, Tm<sup>3+</sup>, Ho<sup>3+</sup>) embedded in an inorganic transparent host material.<sup>17, 21, 30</sup> The parity forbidden optical 4f-4f transitions of the Ln<sup>3+</sup> exhibit long luminescence lifetimes > 100 μs, and hence, UCNPs require rather low excitation power densities (*P*) in the 1 Wcm<sup>-2</sup> - 10<sup>3</sup> Wcm<sup>-2</sup>. Such low *P* can be easily provided by a low-cost continuous-wave laser diode. Moreover, the UC luminescence (UCL) of UCNPs promise a very high signal-to-noise ratio due to the circumvention of the detection of background fluorescence from surrounding biological matrices, a large wavelength shift between emission and excitation (ranging from 130 nm to 500 nm) called anti-Stokes shift and several sharp tunable emission bands with line width < 20 nm (see Figure 1.1).<sup>17, 25</sup> Additionally, their long luminescence lifetimes allow canceling out sources of interference by temporal discrimination called time-gated emission spectroscopy.<sup>17, 21, 30</sup> The NIR-light excitation of UCNPs offers a deep penetration depth in

## 1 Introduction

---

tissue connected with low photodamage on cells compared to the vis-light excitation used for dyes and QDs. However, UCNPs exhibit rather low photon absorption cross-section compared to organic dye and QDs, which is a major challenge to overcome (strategies are addressed in the next paragraph). Further advantages of UCNPs compared to organic dyes and QDs presents the high photostability and the absence of blinking, which are important features for single particle tracking applications.<sup>36</sup> Moreover, results of toxic studies of UCNPs indicate a rather low nanotoxicology.<sup>17, 37, 38</sup> However, these risks have to be more intensely investigated to allow their use inside the human body.

Nowadays, the state-of-the-art synthetic protocols allow producing high-quality UCNPs with defined crystal morphology, narrow size distributions, controlled dopant concentrations and surface chemistries as well as different particle architecture. However, due to high surface-to-volume ratio of UCNPs their maximal  $\Phi_{UC}$  is still one to two orders of magnitude smaller than for bulk. A very promising strategy to avoid surface-related luminescence quenching processes consists in the passivation of the surface with an undoped optically inactive shell. Recently, a report showed that 23 nm-core particles  $\beta$ -NaYF<sub>4</sub>:Yb<sup>3+</sup>(18%),Er<sup>3+</sup>(2%) covered with a 22 nm-thick undoped  $\beta$ -NaYF<sub>4</sub> shell reaching a similar  $\Phi_{UC}$  compared to  $\mu$ m-sized UC particles.<sup>39, 40</sup> Nonetheless, the  $\Phi_{UC}$  of UCNPs with diameters of less than 10 nm, desired for biomedical applications, was yet not fully restored with this core-shell approach.<sup>41</sup> Additionally, the strong absorption of water molecules (H<sub>2</sub>O) at 980 nm, resonant to the Yb<sup>3+</sup> absorption, and thus, drastically enhancing luminescence quenching via the UCNPs surface,<sup>42</sup> is limiting the use of Yb<sup>3+</sup>-based UCNPs in aqueous media. In this respect, co-doping UCNPs with Nd<sup>3+</sup>, excitable at ca. 800 nm, offers an alternative way to avoid absorption of H<sub>2</sub>O, and consequently, reduced heating and luminescence quenching effects.<sup>43, 44</sup> However, Nd<sup>3+</sup>-based UCNPs require more complicated synthetic routes and particle design as well as exhibiting a much narrower absorption band compared to conventional Yb<sup>3+</sup>-based UCNPs. Moreover, as mentioned previously, UCNPs have a rather weak photon absorption cross-section of Ln<sup>3+</sup> ions, typically 5 - 8 orders of magnitude lower than for organic dyes and QDs. Most promising strategies to enhance the absorption of UCNPs comprise a) enhancing local electromagnetic field *via* plasmonics effects based on metal nanostructures or photonic crystals and b) sensitization of UCNPs with organic dyes or QDs. UC luminescence enhancement in the order of three orders of magnitude have already been reported with these strategies.<sup>45-49</sup>

The further rational design of brightly-luminescent UCNPs with industry-relevant structural properties and functionalities requires understanding of (de-)population processes and deactivation channels. This can be assessed with upconversion quantum yield ( $\Phi_{UC}$ )

---

measurements, particle absorption and decay behavior combined with theoretical investigations. In particular, the measurement of  $\Phi_{UC}$ , equaling the ratio of high energy photons emitted to low energy photons absorbed, is known to be very challenging. Due to its strong dependency on the  $P$ , absolute  $\Phi_{UC}$  values can be exclusively determined reliably with a customized integrating sphere setup (ISS). This initiated an increasing number of reports on absolute  $\Phi_{UC}$  measurements utilizing an ISS.<sup>50-55</sup> Nonetheless, the comparison of the  $\Phi_{UC}$  obtained of different laboratories remains a challenging task since most reports are missing a comprehensive description of the instrument design, calibration and characterization as well as measurement procedure. Furthermore, the evaluation of reported  $\Phi_{UC}$  values complicates due to differences in the excitation wavelength, missing a characterization of the excitation beam profile and the use of an insufficiently low  $P$ -range of less than two orders of magnitude. Thus, there is an urgent need for the development of standardized absolute  $\Phi_{UC}$  measurements with an ISS.

### 1.1 Aims and outline of this cumulative thesis

The main aims of this cumulative thesis:

- (i) Designing, building-up and characterizing an ISS for absolute UC quantum yield measurements for UC materials excitable at 980 nm.
- (ii) Identifying UC population and depopulation processes for  $\beta$ -NaYF<sub>4</sub>:Yb<sup>3+</sup>,Er<sup>3+</sup> UCNPs dispersed in H<sub>2</sub>O.
- (iii) Understanding the influence of Yb<sup>3+</sup> and Er<sup>3+</sup> dopant concentration on emission color of  $\beta$ -NaYF<sub>4</sub>:Yb<sup>3+</sup>,Er<sup>3+</sup> UCNPs.

In contrast to the three publications this cumulative thesis is based on, a more detailed description of the custom-built ISS is provided (see Chapter 4). Furthermore, for each publication an abbreviated version has been written (see Chapter 5,6 and 7). These parts may serve as introduction for a broader readership and describe some aspects in more detail. In the following, a brief outline of this thesis is provided:

## 1.1 Aims and outline of this cumulative thesis

---

- **Chapter 2** provides fundamentals of the UC processes. In particular, the UC processes of the investigated  $\beta$ -NaYF<sub>4</sub>:Yb<sup>3+</sup>,Er<sup>3+</sup> UC system are described in detail.
- **Chapter 3** presents an overview of the state of the art for each publication and introduces questions addressed by this thesis.
- **Chapter 4** describes the new custom-built ISS and its characterization as well as the analysis of the obtained data. An overview of the investigated UC samples is also provided.
- **Chapter 5** provides prerequisites for the measurement procedure and geometry and for the optical properties of the UC material as dispersion or powder. Furthermore, the results of  $\Phi_{UC}$  measurement for a  $\mu$ m-sized UC material were validated by comparison with literature data.
- **Chapter 6** presents studies of UCNPs in different solvents with a focus on the optical properties of UCNPs in H<sub>2</sub>O and D<sub>2</sub>O. A model for the (de-)population pathways of UCNPs in H<sub>2</sub>O was developed.
- **Chapter 7** deals with the influence of the Yb<sup>3+</sup> and Er<sup>3+</sup> dopant concentrations on the Er<sup>3+</sup> green and red emission intensities of UCNPs. The interpretations were supported with a comprehensive rate equation analysis.

---

---



---

## 2 Fundamentals

This chapter introduces the physical basics for the understanding of different UC processes. Thereafter, conditions for the composition of an efficient  $\text{Ln}^{3+}$ -based UC material including luminescent centers and host lattices are discussed. Subsequently, a focused overview of the properties of  $\beta\text{-NaYF}_4\text{:Yb}^{3+},\text{Er}^{3+}$  is given. This material is known to be the most efficient NIR to green light converter based on energy transfer upconversion (ETU), and hence, was comprehensively studied in this thesis. At the end of this chapter, a brief theoretical overview of the key parameter  $\Phi_{\text{UC}}$  is provided.

### 2.1 Upconversion (UC) processes

PL is a process in which a material absorbs incident photons, exciting electrons to a higher electronic excited state, and then emits photons after the relaxation of the electrons to a lower energy state.<sup>56</sup> In case of a linear absorption-emission PL process, the energy of the emitted photons do not exceed the energy of the absorbed ones (Stokes shifted emission). However, a UC process permits the combination of multiple absorbed photons resulting in the emission of higher energy photon (anti-Stokes shifted emission). The era of the UC field started in 1959, when Bloembergen proposed the idea of an infrared(IR)-detector based on the sequential absorption of two NIR photons within energy levels of an ion in a solid, called excited state absorption (ESA).<sup>57</sup> Unfortunately, the lack of intense coherent laser sources at this time made it impossible to observe any effects.<sup>30</sup> In 1966, Auzel extended the approach of Bloembergen by utilizing energy transfer between different ions in a solid matrix, called ETU, which could even be detected with incoherent light sources.<sup>30, 58</sup> Nowadays, ETU-based upconverters still belong to the most efficient UC materials.

Figure 2.1 shows a collection of different UC processes for the special case that exactly two absorbed photons are summed-up resulting into the emission of a higher energy photon.<sup>30</sup> ESA is the simplest UC mechanism and involves a sequential absorption of two photons *via* a real intermediate electronic energy state of a  $\text{Ln}^{3+}$ -ion, see Figure 2.1 a). However, this process is not very efficient, because of the rather low absorption coefficients of suitable  $\text{Ln}^{3+}$  ions. Compared to ESA, ETU is about one hundred times more efficient.<sup>30</sup> ETU based upconverters are typically materials doped with two different  $\text{Ln}^{3+}$  called sensitizer and activator. The sensitizer ions harvest the energy, i.e. they effectively absorb incoming photons, and transfer it in sequential steps *via* nonradiative ET to the activator ion, see Figure 2.1 b). The efficiency of ETU is commonly boosted by high sensitizer concentrations allowing

fast energy migration between sensitizer ions inside the crystal lattice.<sup>59</sup> In some special cases, chemically identical ions can act simultaneously as activator and sensitizer ion, e.g. for singly  $\text{Er}^{3+}$ -doped 1520 nm excitable upconverters used for solar cell applications.<sup>60</sup> The efficiency of ESA and ETU processes both rely on metastable energy levels required for the sequential absorption of photons to avoid early depopulation. This is satisfyingly fulfilled by most  $\text{Ln}^{3+}$  ions, due to their parity-forbidden f-f transitions and manifold of energy levels (see 2.3.1 *Luminescent centers*).

Figure 2.1 c) - e) present UC processes based on partly missing or even without any energy level called cooperative energy transfer (CET), two photon absorption (TPA) and second harmonic generation (SHG). CET is similar to ETU, but misses a real intermediate energy level for the activator ion. At the CET process, two sensitizer ions are simultaneously transferring the energy *via* a virtual energy state to the emitting activator ion. Studies on CET-based UC materials primarily focused on bulk and glasses due to their low UC efficiencies.<sup>61-63</sup> TPA and SHG typically occur in non-lanthanide materials and have to be pumped with rather expensive lasers sources with pulse lengths in the pico- to femtosecond time scale as they require very high  $P$ . TPA, which is based on the simultaneous absorption of two photons without a real intermediate energy state, of fluorescent dyes molecules or QDs is frequently used in high-resolution microscopy, bioassays, and even skin cancer detection.<sup>64-66</sup> SHG is a UC process even without occupying any real energy level utilizing the nonlinear susceptibility of a medium. SHG is amongst other applications a popular choice for the frequency doubling of lasers with maximal energy conversion efficiency of up to 70% for optimal conditions.<sup>67</sup>

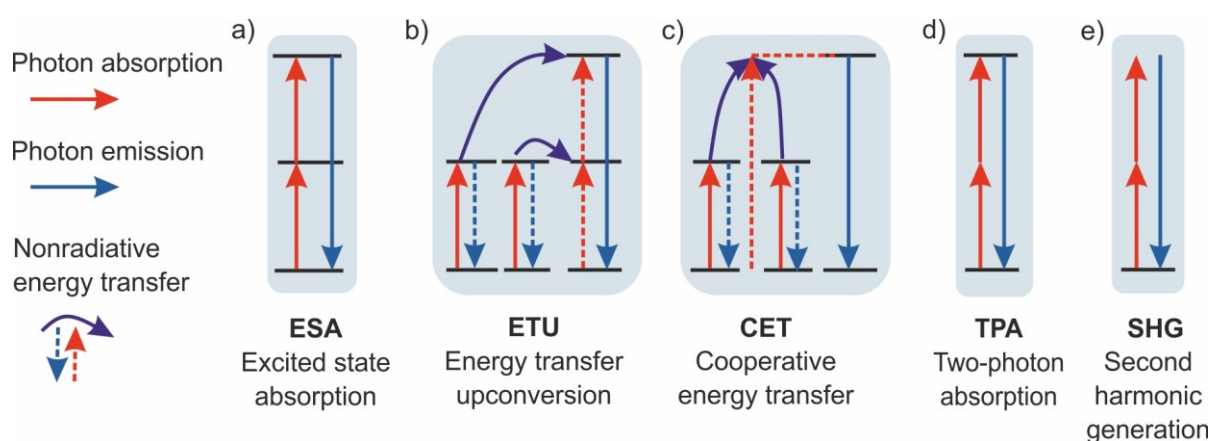


**Figure 2.1** Schematics of different UC mechanism generating a high energy photon by combining two low energy photons: a) ESA; b) ETU; c) CET; d) TPA; e) SHG.

---

## 2.1 Upconversion processes

---

At last, a brief description of the triplet-triplet annihilation (TTA) UC process is provided. TTA-based systems have sizes of only few nanometers due to its molecular structure, and thus, are very promising candidates for biomedical applications.<sup>68</sup> At the TTA process the energy of two triplet-excited dye molecules (annihilators) is combined by ET from one molecule to the other molecule, followed by the emission of a high energy photon. To enhance the absorptivity TTA molecules are typically bound to strong absorbing dye molecules (sensitizers). Thereby, the sensitizers effectively transfer the absorbed energy to the annihilators after an intersystem crossing, i.e. a sensitizer changes from an excited singlet state to a lower energetic excited triplet state. The  $\Phi_{UC}$  values of such TTA-systems found to be in the order of one percentage at rather low  $P$  of several hundred  $\text{mWcm}^{-2}$ .<sup>68, 69</sup> The limiting factor of TTA-systems is the high sensitivity to oxygen of the involved triplet states reducing the  $\Phi_{UC}$ .<sup>70-72</sup>

## 2.2 Energy transfer processes between $\text{Ln}^{3+}$ ions

In this subsection, a theoretical overview of energy transfer (ET) processes between  $\text{Ln}^{3+}$  is provided. Energy transfer is present when absorption and emission of a photon do not take place at the same luminescent center.<sup>30</sup> ET processes can be divided into radiative and nonradiative ET processes. Radiative ET usually plays a minor role for UC processes due to the small absorption coefficients of  $\text{Ln}^{3+}$  ions. In contrast, nonradiative ET is a key feature for ETU leading to effective migration and diffusion processes in the UC crystal lattice. Therefore in this thesis, the term ET implies nonradiative ET. Figure 2.2 depicts radiative and nonradiative ET processes for the simple case of only two ions interacting with each other. These two ions are named sensitizer and activator, where the sensitizer transfers the absorbed energy to the activator. Although donor and acceptor would be clearer terms, sensitizer and activator are intentionally used by the UC community to avoid misunderstanding with the nomenclature used for semiconductors.

**Radiative ET** takes place *via* an exchange of a real photon. The probability  $W_{SA}$  to transfer energy from the sensitizer to the activator for a radiative ET between two ions can be calculated in dependence of the distance  $R$  with Equation 2.1.<sup>73</sup>

$$W_{SA}(R) = \frac{1}{\tau_s} \frac{\sigma_A}{4\pi R^2} \int g_S(\nu) g_A(\nu) d\nu \quad \text{Equation 2.1}$$

Here,  $\tau_s$  is the PL lifetime of the sensitizer,  $\sigma_A$  the integrated absorption cross section of the activator, and the integral represents the spectral overlap between the sensitizer emission  $g_s(\nu)$  and activator absorption  $g_A(\nu)$ . Radiative ET does not affect the PL lifetime of the donor, so that it can be experimentally distinguished from nonradiative ET processes. For more complex systems the probability of a radiative ET  $W_{SA}(R)$  depends not solely on  $R$ , but also on the shape and scattering properties of the sample.

**Nonradiative ET** becomes relevant for short distances in the nanometer range requiring high dopant concentrations of  $\text{Ln}^{3+}$ . In this case the excitation energy is transferred from the sensitizer ion to the activator without the exchange of a real photon, see Figure 2.2 b). Such nonradiative ET *via* dipole-dipole interaction was firstly described by Förster in 1946.<sup>74</sup> Later this theory was extended by Dexter for electric multipolar interactions leading to Equation 2.2 providing the probability for this nonradiative ET process.<sup>75</sup>

$$W_{SA}(R) = \frac{1}{\tau_s} (R_0/R)^k \quad \text{Equation 2.2}$$

Here,  $R_0$  is called the Förster radius, the distance of the two ions at which the probability of an ET equals 50%, and  $k$  is a positive integer with  $k = 6$  for dipole-dipole (Förster case),  $k = 8$  for dipole-quadrupole and  $k = 10$  for quadrupole-quadrupole interactions. The Förster radius depends on the overlap of the sensitizer emission and activator absorption, the integrated absorption cross-section of the activator ion, and the photon energy. However, for very short distances less than 1 nm the orbital overlap or Dexter exchange may become the dominant nonradiative ET process. At this process the excited electrons are “hopping” through the network. The probability  $W_{ET}$  for this process has an exponential relationship to  $R$ .<sup>76</sup>

$$W_{ET}(R) = K^2 e^{-2R/L} \quad \text{Equation 2.3}$$

Here,  $K$  is a scaling parameter with a dimension of energy and the parameter  $L$  is named “effective average Bohr radius”, which accounts for the distance decay of the interaction.

## 2.2 Energy transfer processes

A **phonon-assisted nonradiative ET** can take place between different ions with an energy mismatch between the energy levels of the sensitizer and activator, see Figure 2.2 c). This energy mismatch can be overpassed *via* production or annihilation of phonons. Small energy mismatches  $< 100 \text{ cm}^{-1}$  can be bridged by thermal phonons, and larger energy mismatches, even as high as several thousand  $\text{cm}^{-1}$  can be bridged by optical phonons of the host lattice. In accordance to the Miyakawa-Dexter theory the probability for a phonon assisted ET  $W_{\text{PAT}}(\Delta E)$  can be described with Equation 2.4.<sup>77, 78</sup>

$$W_{\text{PAT}}(\Delta E) = W_{\text{PAT}}(0)e^{-\beta\Delta E}$$

**Equation 2.4**

Here  $\Delta E$  is the energy difference between the sensitizer and the activator level,  $W_{\text{PAT}}(0)$  is the energy transfer probability for  $\Delta E = 0$ ,  $\beta$  is a parameter characterized by the strength of electron-lattice coupling and the nature of the phonon involved.

**Cross-relaxation (CR)** is a special case of nonradiative ET and refers to all types of ETs between identical ions, where one ion transfers a portion of energy to another, see Figure 2.2 d). CR becomes usually a dominant process for high dopant concentration of the activator ions leading the undesired depopulation of the higher energy levels. This is also called concentration quenching.

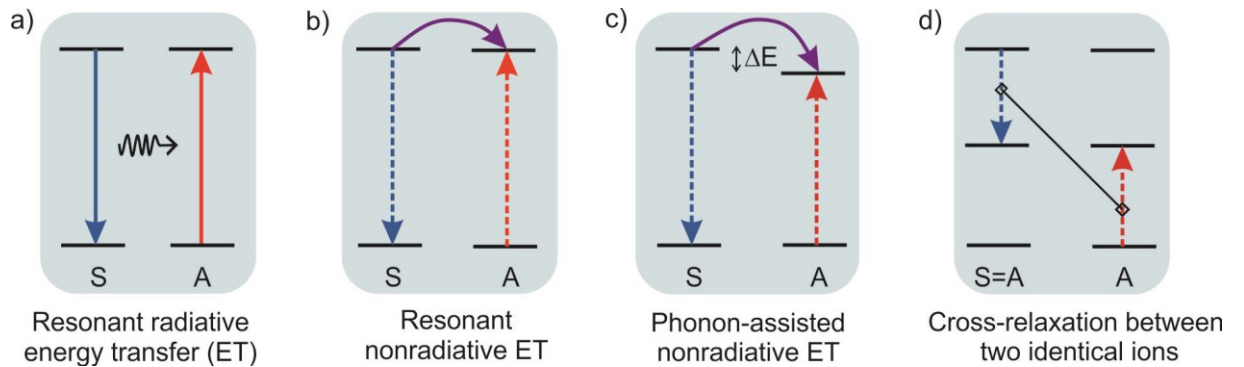


**Figure 2.2 Schematics of radiative and nonradiative ET processes between two ions:**  
a) Resonant radiative ET; b) Resonant nonradiative ET; c) Phonon-assisted nonradiative ET; d) Cross-relaxation. Based on a figure from Auzel.<sup>30</sup>

### 2.3 Energy transfer upconversion (ETU)-based materials

UC materials, based on ETU, consist of three components: i) host lattice, ii) sensitizer ions, and iii) activator ions. The design of efficient UC materials requires careful selection of these components.

#### 2.3.1 Luminescent centers – sensitizer and activator ions

$\text{Ln}^{3+}$  ions have excellent properties for the design of efficient UC materials due to their multiple long-lived optical f-f transitions (with the exception of  $\text{Yb}^{3+}$  and  $\text{Ce}^{3+}$  with only one optical transition). Figure 2.3 shows the energy level scheme for free  $\text{Ln}^{3+}$  ions with their 4f-4f transitions. For free  $\text{Ln}^{3+}$  ions the optical transitions between the 4f-4f energy levels are parity forbidden, i.e. that the probability for the emission of a photon is zero.<sup>79</sup> This rule is broken for  $\text{Ln}^{3+}$  ions embedded in a host lattice. Due to disturbances of the wavefunctions by the strength and symmetry of the crystal field of the host lattice, these parity forbidden transitions become weakly allowed. Because these 4f-4f optical transitions are shielded by the outer  $5s^2 5p^6$  subshells,<sup>80</sup> these effects are small. This implies that the optical transition of the  $\text{Ln}^{3+}$  ions are characterized by long PL lifetimes in the microsecond to millisecond range and narrow linewidths (full width at half maximum (FWHM) typically between 10-20 nm) in the solid state.

In the case of ETU-based UC materials, the standard ingredients are  $\text{Yb}^{3+}$  as sensitizer and  $\text{Er}^{3+}$ ,  $\text{Tm}^{3+}$  or  $\text{Ho}^{3+}$  as activator ions. The reason for  $\text{Yb}^{3+}$  being the best choice as sensitizer is based on three facts: i) Only one excited state ( $^2F_{5/2}$ ), ii) the high absorption cross section compared to other lanthanide ions ( $1.2 \cdot 10^{-20} \text{ cm}^2$  <sup>81</sup>), and iii) the  $^2F_{5/2}$  energy level of  $\text{Yb}^{3+}$  (980 nm) matches energetically well with energy levels of the typical activator ions. For example the  $\text{Er}^{3+}$  980 nm  $^4I_{11/2}$  energy level is resonant to this  $\text{Yb}^{3+}$  energy level allowing efficient  $\text{Yb}^{3+}$ - $\text{Er}^{3+}$  ET. In order to increase the absorption and energy migration usually high dopant concentrations of  $\text{Yb}^{3+}$  in the range of 20% up to 98%.<sup>82</sup> For activator ions a ladder like energy level structure with equally-spaced intermediate energy levels is required. This is fulfilled by  $\text{Er}^{3+}$ ,  $\text{Tm}^{3+}$  and  $\text{Ho}^{3+}$ , see Figure 2.3. The dopant concentration of the activator ion is commonly in the range of 1% to avoid concentration quenching induced by cross relaxation. However, recent studies indicate that for very high  $P$  in the region of  $1 \text{ MWcm}^{-2}$  much higher activator concentrations of up to 20% for  $\text{Er}^{3+}$  are advantageous.<sup>83</sup>

The energy levels of  $\text{Ln}^{3+}$  are denoted in the Russell-Saunders notation using  $4f^N$  states ( $N = 1$  to  $13$ ) of  $^{2S+1}L_J$  multiplets, with  $S$ ,  $L$  and  $J$  representing the total spin, orbital, and angular momenta of the  $N$  4f electrons.<sup>84</sup> The splitting of the energy levels by electrostatic

---

## 2.3 Composition of UC materials

interaction  $^{2S+1}L$  is in the order of  $10^4 \text{ cm}^{-1}$ .<sup>85</sup> In addition, the spin-orbit interaction leads to further splitting of the levels into  $^{2S+1}L_J$  with a separation of the  $J$  states by  $10^3 \text{ cm}^{-1}$ . Moreover, the crystal field of the lattice leads to an additional separation of the energy states in the order of  $10^2 \text{ cm}^{-1}$ .<sup>85</sup>

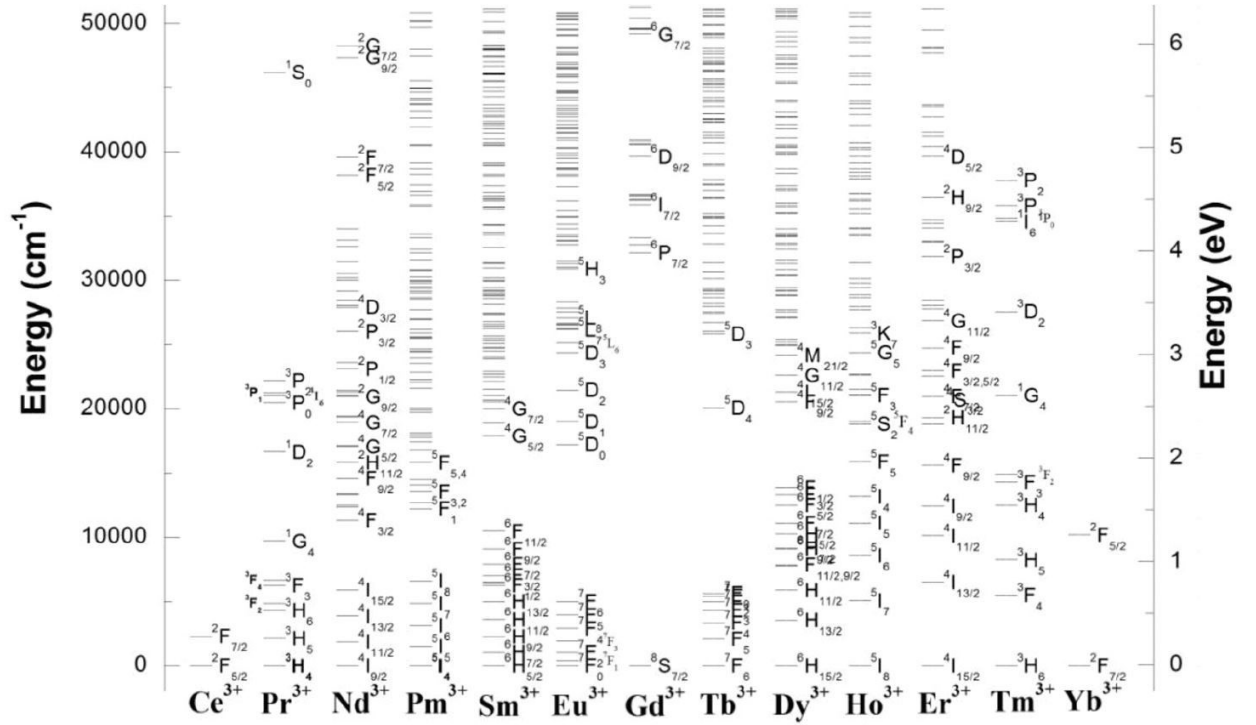


**Figure 2.3** Energy level diagram for the 4f levels of  $\text{Ln}^{3+}$  ions. Positions of energy levels are calculated by using free ion parameters described by Walrand et al.<sup>86</sup> Reprinted from Mahata et al.<sup>80</sup> with permission from Intech.

### 2.3.2 Host lattice

The choice of the host lattice is essential for an efficient UC emitter. An ideal host material should meet the following four criteria:

- i) large band gap  $> 6 \text{ eV}$  to be transparent for excitation and UC emission light
- ii) high tolerance for dopant concentrations of  $\text{Ln}^{3+}$  to avoid lattice defects
- iii) low phonon energies of the host lattice to minimize nonradiative deactivation
- iv) chemically and thermally inert

## 2 Fundamentals

These criteria are met by inorganic host materials based on certain rare earth ions ( $\text{Re}^{3+}$ ):  $\text{Sc}^{3+}$ ,  $\text{Y}^{3+}$ ,  $\text{Gd}^{3+}$ ,  $\text{La}^{3+}$  or  $\text{Lu}^{3+}$ . These materials allow high dopant concentrations of the luminescent centers that substitute these  $\text{Re}^{3+}$  ions in the host lattice. Moreover the luminescent centers have similar ionic radii like all  $\text{Re}^{3+}$  ions ( $\text{Ln}^{3+}$  ions are a subgroup of the group of  $\text{Re}^{3+}$  ions). The most common host matrices used for UC materials are oxides (e.g.  $\text{Y}_2\text{O}_3$ ),<sup>87</sup> oxysulfides (e.g.  $\text{Y}_2\text{O}_2\text{S}$ ),<sup>88</sup> oxyphosphates (e.g.  $\text{LuPO}_4$  and  $\text{YbPO}_4$ )<sup>89</sup> and fluorides (e.g.  $\text{NaYF}_4$ )<sup>90</sup>. In addition, other alkaline earth ion and transition metal ion based compounds are frequently used as host materials (e.g.,  $\text{Ca}^{2+}$ ,  $\text{Zr}^{4+}$ ).<sup>91, 92</sup>

Among these materials, the fluoride-based  $\text{NaReF}_4$  have been used for decades as nm-sized host lattices due to their low phonon energy (quantized energy portions of lattice vibrations), excellent chemical stability, and thermal stability.<sup>93-95</sup>  $\text{NaReF}_4$  has two different crystal phase structures, the cubic ( $\alpha\text{-NaReF}_4$ ) and the hexagonal phase structure ( $\beta\text{-NaReF}_4$ ), see Figure 2.4.

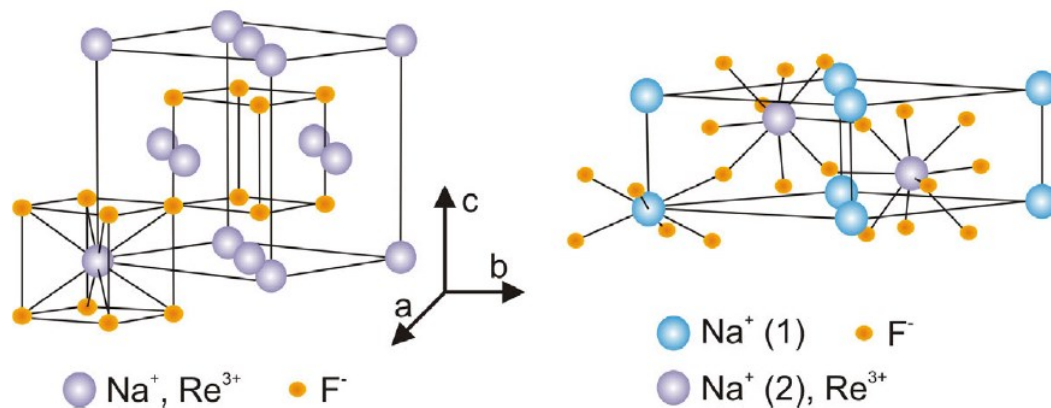


**Figure 2.4 Schematic presentation of the crystal structure of  $\text{NaReF}_4$  in the cubic and hexagonal-phase.** a) The cubic phase is characterized by an equal number of  $\text{F}^-$  cubes containing cations and vacancies; b) the hexagonal phase shows an ordered array of  $\text{F}^-$  ions with two kind of cation sites, where one is occupied by  $\text{Na}^+$  and the other one is randomly occupied by either  $\text{Na}^+$  and  $\text{Re}^{3+}$ . Reprinted from Wang et al.<sup>96</sup> with permission from Nature Publishing Group.

It is well established that the family of  $\beta\text{-NaReF}_4$  is much more efficient as host lattice for UC materials than  $\alpha\text{-NaReF}_4$ , due to their lower phonon energies of about  $350\text{ cm}^{-1}$  and a lower symmetry of the crystal field.<sup>97, 98</sup> These lower phonon energies result in a smaller probability of phonon-based nonradiative deactivation. The probability of such a



deactivation process, also called multiphonon relaxation (MPR), depends exponentially on the number of phonons with an energy  $E_{\text{phonon}}$  needed to bridge the energy gap  $\Delta E$  between the final and the initial energy level and can be calculated with Equation 2.5.<sup>99, 100</sup>

$$W_{\text{MPR}}(p) = \beta e^{-\alpha p} \quad \text{Equation 2.5}$$

Here,  $\alpha$  and  $\beta$  depend on the specific properties of the host lattice and  $p = \Delta E/E_{\text{phonon}}$  equals the number of phonons required for the nonradiative deactivation. MPR is the dominant nonradiative process for perfectly crystalline materials. However, for nm-sized particles the nonradiative deactivation is mostly governed by lattice defects or molecules near the surface or inside the particle volume.<sup>59, 101</sup> In particular, this is critical for ET-based UC systems, where the ET can be effectively transferred *via* energy migration to quenching centers. A recent study showed that surface-related quenching and the number of defect centers can be strongly minimized with a thick inactive shell and slow particle growth rates.<sup>39</sup>

## **2.4 Upconversion luminescence (UCL) of $\beta$ -NaYF<sub>4</sub>:Yb<sup>3+</sup>,Er<sup>3+</sup> crystals**

The UC system  $\beta$ -NaYF<sub>4</sub>:Yb<sup>3+</sup>,Er<sup>3+</sup> combines the previously discussed criteria for host lattice and luminescent centers for an efficient ETU-based UC material. This material is intensively studied since the mid-1960s and well known for its high UC efficiency. Typical dopant concentrations range from 17-20% for the Yb<sup>3+</sup>-ion and 1-2% for the Er<sup>3+</sup>-ion dopant concentrations aiming on an intense Er<sup>3+</sup> green UCL.<sup>21, 97</sup> ESA processes involving the Er<sup>3+</sup> energy levels can be neglected, due to the 10-fold higher absorbance of Yb<sup>3+</sup> compared to Er<sup>3+</sup>. Figure 2.5 shows a typical UCL spectrum of  $\beta$ -NaYF<sub>4</sub>:Yb<sup>3+</sup>,Er<sup>3+</sup>, which is dominated by the Er<sup>3+</sup> emission bands ranging from 370-870 nm. The strongest UC emission bands are centered at 380 nm, 410 nm, 520 nm and 540 nm, 655 nm, 810 nm, and 850 nm. All Er<sup>3+</sup> emission bands are characterized by a substructure of several sharp emission peaks, caused by a splitting from the crystal field of the host lattice. The associated emissive Er<sup>3+</sup> energy levels can be populated *via* two or more energy transfers from Yb<sup>3+</sup> to Er<sup>3+</sup> and in combination with internal nonradiative relaxation processes, see Figure 2.6.

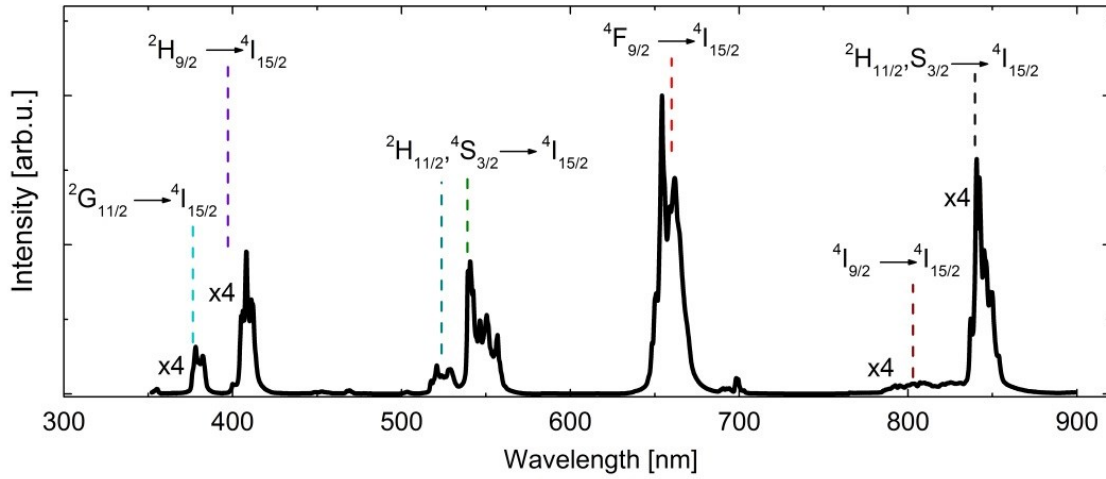


**Figure 2.5** UCL emission spectrum of  $\mu\text{m}$ -sized  $\beta\text{-NaYF}_4\text{:Yb}^{3+}(21\%),\text{Er}^{3+}(2\%)$  UC particles ( $\text{UC}\mu\text{P}_{\text{BAM}}$ ) excited at 976.4 nm at a  $P$  of  $20 \text{ Wcm}^{-2}$ . The typical  $\text{Er}^{3+}$  emission bands are centered at 380 nm ( $^4\text{G}_{11/2} \rightarrow ^4\text{I}_{15/2}$ ), 410 nm ( $^2\text{H}_{9/2} \rightarrow ^4\text{I}_{15/2}$ ), 520 nm/540 nm ( $^2\text{H}_{11/2}, ^4\text{S}_{3/2} \rightarrow ^4\text{I}_{15/2}$ ), 655 nm ( $^4\text{F}_{9/2} \rightarrow ^4\text{I}_{15/2}$ ), 810 nm ( $^4\text{I}_{9/2} \rightarrow ^4\text{I}_{15/2}$ ), and 850 nm ( $^2\text{H}_{11/2}, ^4\text{S}_{3/2} \rightarrow ^4\text{I}_{15/2}$ ). For a better visualization the UV and NIR bands were multiplied by a factor of 4. The  $\text{Er}^{3+}$  green and red emission bands account for  $> 80\%$  of the overall UCL intensity.

**The  $\text{Er}^{3+}$  green emission bands** ( $^2\text{H}_{11/2}, ^4\text{S}_{3/2} \rightarrow ^4\text{I}_{15/2}$ ) centered at 520 nm and 540 nm and  **$\text{Er}^{3+}$  NIR 850 nm emission band** ( $^2\text{H}_{11/2}, ^4\text{S}_{3/2} \rightarrow ^4\text{I}_{13/2}$ ) centered at 850 nm are activated *via* two  $\text{Yb}^{3+}\text{-Er}^{3+}$  ETs. The first ET populates the  $\text{Er}^{3+}$   $^4\text{I}_{11/2}$  energy level, followed by a second ET populating the  $\text{Er}^{3+}$   $^4\text{F}_{7/2}$  energy level. Due to the high nonradiative rate for  $\text{Er}^{3+}$   $^4\text{F}_{7/2}$  energy level, the excited electron relaxes mainly to the directly lower lying  $^2\text{H}_{11/2}, ^4\text{S}_{3/2}$  energy levels. Subsequently, an optical transition can take place either to the ground state  $^4\text{I}_{15/2}$  or the first excited state  $^4\text{I}_{13/2}$  of  $\text{Er}^{3+}$  resulting in the green 520/540 nm or NIR 850 nm emission, respectively.

**The  $\text{Er}^{3+}$  NIR 810 nm emission band** ( $^4\text{I}_{9/2} \rightarrow ^4\text{I}_{15/2}$ ) centered at 810 nm can be populated *via* two different biphotonic pathways. The first population pathway is *via* CR from the biphotonically activated  $^2\text{H}_{11/2}, ^4\text{S}_{3/2}$  to  $^4\text{I}_{9/2}$  and the second *via*  $\text{Er}^{3+}\text{-Er}^{3+}$  ET in case of a high population of the  $\text{Er}^{3+}$   $^4\text{I}_{13/2}$  energy level ( $^4\text{I}_{13/2} + ^4\text{I}_{13/2} \rightarrow ^4\text{I}_{9/2}$ ).

The Er<sup>3+</sup> ultraviolet (UV) emission band ( $^4G_{11/2} \rightarrow ^4I_{15/2}$ ) centered at 380 nm and the Er<sup>3+</sup> purple emission band ( $^2H_{9/2} \rightarrow ^4I_{15/2}$ ) centered at 410 nm are populated by a triphotonic UC process, i.e. that three sequential Yb<sup>3+</sup>-Er<sup>3+</sup> ETs are involved. The first two ET steps are identical as described above for the biphotonically activated green-emitting  $^2H_{11/2}$ ,  $^4S_{3/2}$  energy levels. The third ET excites the electron to the  $^2G_{7/2}$  energy level, followed by nonradiative relaxation to the  $^4G_{11/2}$  and  $^2H_{9/2}$  energy levels. The optical transition to the ground state  $^4I_{15/2}$  then results in the UV or purple emission, respectively.

The Er<sup>3+</sup> red emission band ( $^4F_{9/2} \rightarrow ^4I_{15/2}$ ) centered at 655 nm has the most complex nature of all emission bands as it can be activated *via* different biphotonic and triphotonic pathways. A comprehensive overview of the conditions for bi- or triphotonic activation, which was intensively debated within the last years, is given in the introduction of Publication III. In the following a brief version of this overview is presented. The photonic nature of the Er<sup>3+</sup> red emission band depends on the crystal phase, size, particle architecture, environment and excitation power density ( $P$ ).<sup>23, 26, 29, 40, 42, 55, 96, 102-113</sup> The triphotonic population pathway suggested from the Berry group in 2014<sup>102</sup> includes an Er<sup>3+</sup>-Yb<sup>3+</sup> back energy transfer (BET) from the triphotonic activated UV emissive  $^4G_{11/2}$  energy state to the red emissive  $^4F_{9/2}$  energy state. The biphotonic activation of the Er<sup>3+</sup>  $^4F_{9/2}$  energy level can occur *via* two different population routes. The first biphotonic population pathway directly feeds the  $^4F_{9/2}$  energy level *via* nonradiative relaxation from the biphotonically activated  $^4S_{3/2}$  energy levels. Therefore, an energy gap in the order of 3000 cm<sup>-1</sup> to 3200 cm<sup>-1</sup> has to be overpassed. In the case of UCNPs capped with oleic acid molecules the stretching vibrational modes of the CH<sub>2</sub>-groups (2800 cm<sup>-1</sup> to 2950 cm<sup>-1</sup>) are perfectly capable to bridge this energy gap.<sup>114</sup> The second biphotonic pathway occurs *via* the 1520 nm  $^4I_{13/2}$  energy level of Er<sup>3+</sup>, which can be populated by nonradiative relaxation from one ET activated Er<sup>3+</sup> 980 nm  $^4I_{11/2}$  energy level. Due to an energy mismatch of 1000 cm<sup>-1</sup> to the Er<sup>3+</sup> red emissive  $^4F_{9/2}$ , this ET needs assistance by phonons and requires population of the  $^4I_{13/2}$  energy level.

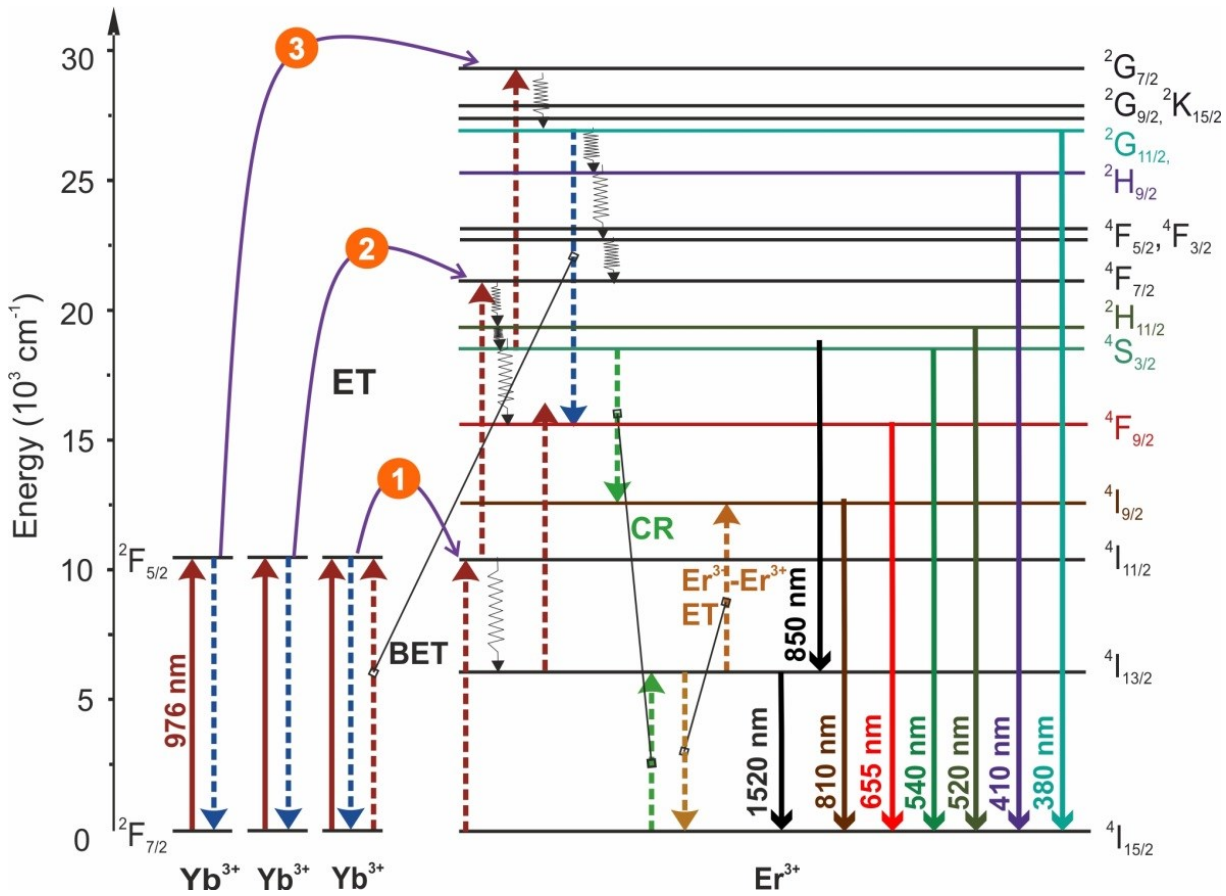


**Figure 2.6** Term scheme illustrating the relevant population pathways for the different  $\text{Er}^{3+}$  emission bands for  $\text{Yb}^{3+}, \text{Er}^{3+}$  based UC materials. Solid arrows represent excitation or de-excitation of an energy state by absorption or emission of a photon; the dashed arrows represents ET processes including  $\text{Yb}^{3+}, \text{Er}^{3+}$  ET,  $\text{Er}^{3+}-\text{Yb}^{3+}$  BET, CR between two  $\text{Er}^{3+}$  ions and  $\text{Er}^{3+}-\text{Er}^{3+}$  ET; curved arrows presents nonradiative relaxation processes by MPR. It should be noted that for simplification the splitting of energy levels by the crystal field of the host lattice is not included in the term scheme.

### 2.5 Upconversion photoluminescence quantum yield ( $\Phi_{UC}$ )

The  $\Phi$  (also often referred as “*internal quantum yield*”), presents the ratio of the number of emitted ( $N_{em}$ ) to the number of absorbed photons ( $N_{abs}$ ), see Equation 2.6.<sup>11, 21, 115, 116</sup> This key parameter characterizes the photon conversion performance of photoluminescent materials.

$$\Phi = N_{em}/N_{abs} \quad \text{Equation 2.6}$$

In the case of the  $\Phi_{UC}$ , only emitted photons with a higher energy than the energy of the absorbed ones are considered ( $E_{em} > E_{abs}$ ), see Equation 2.7.<sup>11, 53, 102, 115, 117</sup>

$$\Phi_{UC} = N_{em}/N_{abs}, \text{ for } E_{em} > E_{abs} \quad \text{Equation 2.7}$$

As the UC process is a nonlinear process, a higher excitation power density ( $P$ ) generally leads to an increase of  $\Phi_{UC}$ . In the case of a biphotonic UC process, the UCL intensity ( $I_{UC}$ ) is proportional to  $P^2$ , and consequently,  $\Phi_{UC}$  increases linearly with  $P$ . However, due to the energy conservation law, the  $P$ -dependent increase of  $\Phi_{UC}$  has to level off at higher  $P$ , and thus  $\Phi_{UC}$  is limited by  $100\%/n$ , where  $n$  is the photonic order of the UC process.<sup>28, 118</sup> The saturation behavior of the  $P$ -dependent  $\Phi_{UC}$  ( $\Phi_{UC}(P)$ ) for an ideal biphotonic emitter was studied by the Andersson-Engels group. They assumed a two-level emitter system and subsequently derived a formula for  $\Phi_{UC}(P)$  for this simple UC system, see Figure 2.7 a) and Equation 2.8.<sup>119</sup>

$$\phi_{UC}(P) = \phi_{UC,sat} / (\frac{P_{balance}}{P} + 1) \quad \text{Equation 2.8}$$

Here,  $\Phi_{UC,sat}$  is the saturated upconversion quantum yield, where  $\Phi_{UC}(P)$  converges at high  $P$ , and  $P_{balance}$  is the balancing excitation power density, where  $\Phi_{UC}(P_{balance})$  equals  $\Phi_{UC,sat}/2$ .

## 2 Fundamentals

Figure 2.7 b) shows the typical shape of the  $\Phi_{UC}$  curve for such an ideal biphotonic emitter, calculated with Equation 2.8. This formula is only valid for purely biphotonic UC processes like the NIR 800 nm emission band of  $Tm^{3+}, Yb^{3+}$  and the green 520/540 nm of  $Yb^{3+}, Er^{3+}$  based UC systems.<sup>40, 119, 120</sup> In contrast, this formula is not suitable to describe the shape of  $\Phi_{UC}(P)$  for the red emission of  $Yb^{3+}, Er^{3+}$  or  $Yb^{3+}, Ho^{3+}$  as here the population processes are more complicated.<sup>40, 55, 102, 121</sup>

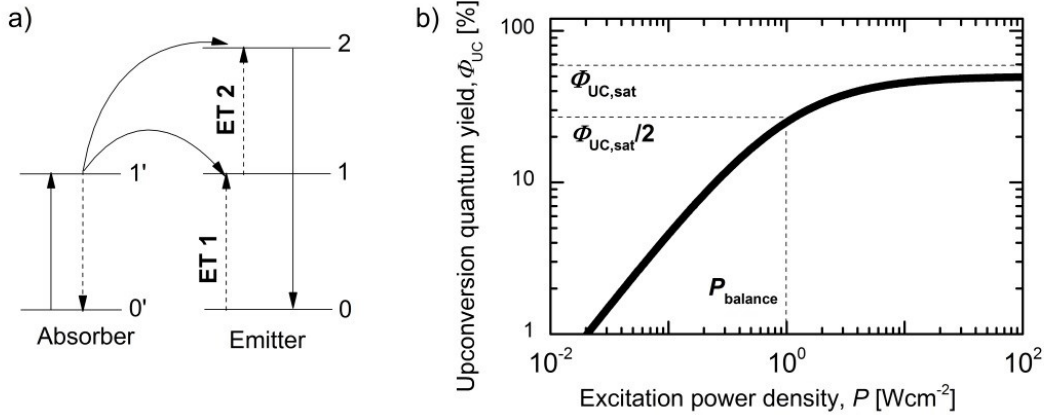


**Figure 2.7**  $P$ -dependent  $\Phi_{UC}$  behavior of a two-level emitter ETU system: a) Term scheme of the two-level emitter system; b)  $\Phi_{UC}(P)$  curve calculated for  $\Phi_{UC,sat} = 50\%$  and  $P_{balance} = 1 \text{ Wcm}^{-2}$  with Equation 2.8.<sup>119</sup>

The simulation of  $\Phi_{UC}(P)$  for more complex UC systems can be achieved by using a rate equation system consisting of a set of coupled differential equations, see Equation 2.9.<sup>122</sup>

$$\frac{dN_i}{dt} = \sum \text{populating rates} - \sum \text{depopulating rates} \quad \text{Equation 2.9}$$

Thereby, the population densities ( $N_i$ ) of the most significant 4f energy levels of the  $Ln^{3+}$  ions and their interactions have to be considered. The interactions are represented by populating and depopulating rates of the energy states including radiative rates and nonradiative rates like ET, CR, and MPR. A very decent approach was demonstrated by the Berry group for  $\beta\text{-NaYF}_4:Yb^{3+}, Er^{3+}$   $\mu\text{m}$ -sized and nm-sized UC systems with a rate equation system including a set of nine energy levels for  $Er^{3+}$ .<sup>102, 123</sup> This rate equation system was later also used in Publication II and III to draw and underpin interpretations of the influence on UC mechanisms for  $\beta\text{-NaYF}_4:Yb^{3+}, Er^{3+}$  UCNPs by modeling the  $P$ -dependent intensities of the  $Er^{3+}$  emission bands.

---

## 3 Reviews of Literature and Open Questions

In this chapter a review of the literature for each publication is presented. Furthermore, open questions are formulated, which are addressed in the chapters 4, 5, 6 and 7.

### 3.1. Absolute upconversion photoluminescence quantum yield ( $\Phi_{UC}$ )

Recently, absolute  $\Phi_{UC}$  measurements have raised great interest in the UC community as a quantitative comparison tool to identify strategies to improve the brightness of UCNPs.<sup>124</sup> Attempts to measure the  $\Phi_{UC}$  relative against a  $\Phi_{UC}$  standard or to determine enhancement factors with a spectrofluorometer<sup>125-127</sup> have shown limited reliability. This is related to the fact that there is no reliable  $\Phi_{UC}$  standard available, and additionally, due to often different scattering properties and different  $P$ -dependencies of  $\Phi_{UC}$  for UC materials.<sup>40</sup> Therefore, the  $\Phi_{UC}$  can be only measured absolutely with a spectrally calibrated ISS done.<sup>51, 52, 54, 55, 128-132</sup> Although, the increasing number of reports on ISS the comparability of the  $\Phi_{UC}$  results obtained with these setups is still limited by the often missing description of the instrument design and instrument characterization. For example, there is no report how the influence of the excitation beam profile (BP), i.e. the spatial distribution of  $P$ , is considered. Additionally, often reports provide only a single  $\Phi_{UC}$  value or the  $\Phi_{UC}$  has been measured only in a small  $P$ -range of less than two orders of magnitude, which is insufficient for monitoring saturation dynamics of the UC process. Up to the publication date of Publication I (June 2017) the highest measured  $\Phi_{UC}$  value for Yb<sup>3+</sup>,Er<sup>3+</sup>-based systems was 7.8 % for a  $\beta$ -NaYF<sub>4</sub>:Yb<sup>3+</sup>(20%),Er<sup>3+</sup>(2%)  $\mu$ m-sized UC powder at  $P$  of 22 Wcm<sup>-2</sup>.<sup>54</sup>

#### Open questions

- What are the prerequisites for the design and characterization of an ISS for reliable  $\Phi_{UC}$  measurements? (see 4.2.1 *Integrating sphere* )
- What are the prerequisites on the optical properties of the sample, measurement procedure, and measurement geometry to obtain  $\Phi_{UC}$  values with minimum uncertainty? (see 5.1. *Measurement conditions for  $\Phi_{UC}(P)$* )

### 3.2. Solvent-dependent luminescence quenching

UCNPs are generally more prone to surface quenching due to their much higher surface-to-volume ratio and shorter distance between particle center and surface compared to larger-sized particles. Thus,  $\text{Ln}^{3+}$  ions of UCNPs can transfer energy effectively to the surface region, where the excited ions can be deactivated nonradiatively by impurities or crystal defects on the surface, as well as vibrational modes of O-H and C-H bands of solvent and ligand molecules.<sup>110, 112, 113, 133-136</sup> Particularly, the interest in UCNPs for aqueous environments for life sciences applications has triggered an increasing number of reports studying solvent quenching mechanism in water ( $\text{H}_2\text{O}$ ).<sup>42, 107, 133, 137-139</sup> Arppe et al. showed in a joint publication in 2015 that  $\text{Yb}^{3+}$  ions play a major role for the migration of energy to the surface. Therefore, they studied bare rod-shaped *ca.* 35 nm-sized  $\beta\text{-NaYF}_4\text{:Yb}^{3+}(17\%),\text{Er}^{3+}(2\%)$  UCNPs dispersed in  $\text{H}_2\text{O}$  and deuterated water ( $\text{D}_2\text{O}$ ), showing a decrease of the  $\text{Er}^{3+}$  green ( $^2\text{H}_{11/2}, ^4\text{S}_{3/2} \rightarrow ^4\text{I}_{15/2}$ ) and  $\text{Er}^{3+}$  red ( $^4\text{F}_{9/2} \rightarrow ^4\text{I}_{15/2}$ ) UCL intensity of 99.9% for UCNPs in  $\text{H}_2\text{O}$  compared to  $\text{D}_2\text{O}$  for the UCNPs in  $\text{H}_2\text{O}$ .<sup>140</sup> Wilhelm et al. reported in a joint publication green-to-red ratios ( $I_{\text{green}}/I_{\text{red}}$ ) of  $\text{NaYF}_4\text{:Yb}^{3+}(17\%),\text{Er}^{3+}(2\%)$  23 nm-sized UCNPs in dependence of different solvents and different surface ligands.<sup>138</sup> This report did not include a model for the change of population and depopulation processes in  $\text{H}_2\text{O}$ .

#### Open questions

- How to measure  $\Phi_{\text{UC}}$  in strongly absorbent solvents like  $\text{H}_2\text{O}$ ? (see 5.1. *Measurement conditions for  $\Phi_{\text{UC}}(P)$ , Heating of the UCNP sample and solvent*)
- What is the influence on the  $\Phi_{\text{UC}}$  of surface protected UCNPs dispersed in different solvents? (see 6.1 *Solvent-dependent quantum yield ( $\Phi_{\text{UC}}$ )*)
  - How are the UCL bands and de- and population processes of these UCNPs affected by different solvents? (see 6.2 *Emission color of UCNPs dispersed in  $\text{D}_2\text{O}$  and  $\text{H}_2\text{O}$* )



### 3.3. Dopant concentration-dependent color tuning

The dopant ion concentration of  $\text{Yb}^{3+}, \text{Er}^{3+}$ -based UCNPs has direct influence on their optical properties like  $\Phi_{\text{UC}}$  and emission color. An increase of the  $\text{Yb}^{3+}$  concentration leads to an increase of the intensity of the  $\text{Er}^{3+}$  red emission band ( $^4\text{F}_{9/2} \rightarrow ^4\text{I}_{15/2}$ ) at the expenses of the  $\text{Er}^{3+}$  green emission band ( $^2\text{H}_{11/2}, ^4\text{S}_{3/2} \rightarrow ^4\text{I}_{15/2}$ ) as frequently reported.<sup>82, 104-106, 141-143</sup> However, different explanations are given for this observation. For the variation of  $\text{Er}^{3+}$  concentration, ambiguous or even opposite trends of the  $\text{Er}^{3+}$  green-to-red intensity ratio ( $I_{\text{green}}/I_{\text{red}}$ ) have been observed.<sup>141, 142, 144-146</sup> Additionally, the evaluation of these data is difficult as the dopant concentration-dependent  $I_{\text{green}}/I_{\text{red}}$  is also affected by  $P$ , and most publications provide the  $I_{\text{green}}/I_{\text{red}}$  only for single  $P$  values. To clarify the mechanisms influenced by the dopant concentration, a comprehensive rate equation analysis using  $P$ -dependent spectral intensities for a broad  $P$ -range and lifetime data of the different emission bands for  $\beta\text{-NaYF}_4:\text{Yb}^{3+}, \text{Er}^{3+}$  is necessary. This has not been reported for varying the  $\text{Yb}^{3+}$  and  $\text{Er}^{3+}$  concentration.

#### Open questions

- How do the  $\text{Yb}^{3+}$  and the  $\text{Er}^{3+}$  dopant concentration influence the  $P$ -dependent UCL? (see 7.1 Dopant concentration-dependent upconversion luminescence (UCL))
- How do the rate constants change by variations of the  $\text{Yb}^{3+}$  and the  $\text{Er}^{3+}$  dopant concentration? (see 7.2 Influence of the dopant concentrations on rate equation constants)

---

---

---

## 4. Samples and Experimental Methods

This chapter provides an overview of the investigated UC samples and a description of the custom-built ISS with its optical and opto-electronic components and ratiometric characterization, as well as the analysis of the data. At the end of the chapter, the commercial setup for lifetime measurements is described.

### 4.1. Overview of investigated $\beta$ -NaYF<sub>4</sub>:Yb<sup>3+</sup>,Er<sup>3+</sup> samples

In Table 4.1 all investigated  $\beta$ -NaYF<sub>4</sub>:Yb<sup>3+</sup>,Er<sup>3+</sup> UC particles are listed. For Publication I commercial 3  $\mu$ m-sized  $\beta$ -NaYF<sub>4</sub>:Yb<sup>3+</sup>(21%),Er<sup>3+</sup>(2%) UC particles (PTIR 550) obtained from *Phosphor Technology Ltd.* were studied.<sup>147</sup> The UCNPs were synthesized by project partners using different chemicals for the building blocks of  $\beta$ -NaYF<sub>4</sub>:Yb<sup>3+</sup>,Er<sup>3+</sup> crystals. These reagents were mixed and heated up to initialize formation of the UCNPs. To produce high quality UCNPs with pure phase structure well-developed protocols with exact timing for each heating step, high purity reagents, and optical growth control are required.<sup>138</sup>

#### UCNPs samples synthesized by Emilia Palo from the Prof. Soukka group, University of Turku, Finland

Emilia Palo from the group of Tero Soukka from Finland synthesized the UCNPs, for Publication I and Publication III, using a protocol from Ylihärsilä et. al.<sup>148</sup> with small modifications (see Table 4.1). For Publication I, oleic acid (OA)-capped 25 nm-sized  $\beta$ -NaYF<sub>4</sub>:Yb<sup>3+</sup>(17%),Er<sup>3+</sup>(3%) UCNPs were synthesized. For Publication III, two dopant concentration series with different Yb<sup>3+</sup> and Er<sup>3+</sup> concentrations were synthesized (see Table 4.1). The structural analysis was mainly performed by the Soukka group. This included X-ray diffraction (XRD) measurements to verify the hexagonal crystal phase and transmission electron microscopy (TEM) measurements to determine the size and size distribution of the UCNPs. Moreover, measurements with a inductively coupled plasma optical emission spectrometer (ICP-OES) were performed by M.Sc. Melissa Monks from the *Federal Institute for Material Research and Testing* (BAM) in order to determine the dopant Er<sup>3+</sup> and Yb<sup>3+</sup> content of the studied UCNP samples of Publication III.

##### **UCNPs samples synthesized by Stefan Wilhelm from the Dr. Hirsch group, University of Regensburg, Germany**

For Publication II, OA-capped 23 nm-sized  $\beta$ -NaYF<sub>4</sub>:Yb<sup>3+</sup>(19%),Er<sup>3+</sup>(2%) UCNPs were synthesized by Stefan Wilhelm, from the group of Dr. Hirsch from the University of Regensburg, using a newly developed synthesis protocol<sup>138</sup> based on a protocol from Li. et al in 2008<sup>149</sup>. This new protocol yields high quality UCNPs with a small size distribution in one large batch of about 2 grams. From this batch, surface modified UCNPs samples were produced by functionalizing these UCNPs with different surface passivating and stabilizing molecules to ensure dispersibility in different solvents.<sup>138</sup> Two different surface modification strategies were used to enable the transfer of the UCNPs to polar solvents like H<sub>2</sub>O, D<sub>2</sub>O and DMF. The first strategy involves a complete exchange of the original OA molecules with citrate and BF<sub>4</sub><sup>-</sup>. In the second strategy OA-capped UCNPs are shelled with a second layer of ligands molecules using DSPE, which are molecules soluble in polar and nonpolar solvents, see Table 4.1. The Hirsch group also performed the structural analysis with TEM and XRD measurements. Additionally, they did ICP-OES and dynamic light scattering (DLS) measurements to determine dopant concentrations and solvodynamic particle diameters, respectively.

### 4.1. Overview of investigated $\beta$ -NaYF<sub>4</sub>:Yb<sup>3+</sup>,Er<sup>3+</sup>

**Table 4.1** Investigated  $\beta$ -NaYF<sub>4</sub>:Yb<sup>3+</sup>,Er<sup>3+</sup> UC samples with respective average particle diameter, the Yb<sup>3+</sup> and the Er<sup>3+</sup> dopant content, passivating ligands and solvent.

$\beta$ -NaYF <sub>4</sub> :Yb <sup>3+</sup> ,Er <sup>3+</sup> Samples	Particle diameter	Yb <sup>3+</sup> concentration <sup>a</sup>	Er <sup>3+</sup> concentration <sup>a</sup>	Solvent	Ligand
<b>Publication I</b>					
UC $\mu$ P <sub>BAM</sub> powder	3 $\mu$ m	21.4%	2.2%	-	-
UCNPs powder	25 nm	17%	3%	-	Oleic acid
UCNPs dispersion	25 nm	17%	3%	Toluene	Oleic acid
<b>Publication II</b>					
UCNPs dispersion	23 nm	19.3%	2.3%	Cyclohexane	Oleic acid
UCNPs dispersion	23 nm	19.3%	2.3%	DMF <sup>b</sup>	BF <sub>4</sub> <sup>-</sup>
UCNPs dispersion <sup>c</sup>	23 nm	19.3%	2.3%	D <sub>2</sub> O	Citrate
UCNPs dispersion <sup>c</sup>	23 nm	19.3%	2.3%	H <sub>2</sub> O	Citrate
UCNPs dispersion	23 nm	19.3%	2.3%	D <sub>2</sub> O	DSPE <sup>d</sup>
UCNPs dispersion	23 nm	19.3%	2.3%	H <sub>2</sub> O	DSPE <sup>d</sup>
<b>Publication III</b>					
UCNPs dispersion	33 nm	14.4%	0.9%	Toluene	Oleic acid
UCNPs dispersion	33 nm	14.4%	2.1%	Toluene	Oleic acid
UCNPs dispersion	33 nm	14.4%	3.1%	Toluene	Oleic acid
UCNPs dispersion	33 nm	14.4%	3.8%	Toluene	Oleic acid
UCNPs dispersion	33 nm	10.6%	3.1%	Toluene	Oleic acid
UCNPs dispersion	33 nm	17.1%	3.1%	Toluene	Oleic acid
UCNPs dispersion	33 nm	20.5%	3.1%	Toluene	Oleic acid

<sup>a</sup> Er<sup>3+</sup> and Yb<sup>3+</sup> substitute for the Y<sup>3+</sup> ions of the  $\beta$ -NaYF<sub>4</sub> matrix; sum of dopant concentration of Er<sup>3+</sup>,Yb<sup>3+</sup> and Y<sup>3+</sup> equals 100%.

<sup>b</sup> N,N-dimethylformamide

<sup>c</sup> these samples are not discussed in this thesis

<sup>d</sup> 1,2-distearoyl-sn-glycero-3-phospho-ethanolamine-N-[methoxy-(poly-ethylene glycol)-2000] (ammonium salt) (DSPE)

## 4.2 Optical characterization methods

In this section the custom-built new integration sphere setup for absolute measurement of  $\Phi_{UC}$  and UCL is presented, as well as, the commercial setup used for time resolved PL measurements.

### 4.2.1 Integrating sphere setup (ISS)

This subsection comprehensively describes the components and characterization of the custom-built ISS. Moreover, the analysis of  $P$ -dependent UCL leading to information about the photonic order and (de)population processes of the UC process is presented.

#### 4.2.1.1 Components and characterization of the ISS

Figure 4.1 shows the ISS for absolute  $P$ -dependent  $\Phi_{UC}$  measurements, which I extended from an existing ISS built by Dr. Christian Würth from the BAM.<sup>116, 150</sup> A detailed description of the ISS is also provided in the Supporting Information (SI) of Publication I. This ISS consists of an excitation channel, where the excitation light is generated and guided to the sample, and a detection channel to record the emitted UCL and excitation light in absolute spectral photon fluxes ( $\text{s}^{-1}\text{m}^{-2}\text{nm}^{-1}$ ). The heart of the ISS is the integrating sphere. Its interior is covered with a diffusive white reflective coating guarantying that after multiple reflections the incident light is evenly distributed at any point of the inner surface. Consequently, the measurements of photon fluxes with an ISS do not require any consideration of the direction of propagation, the beam geometry and polarization of the excitation and emitted light.

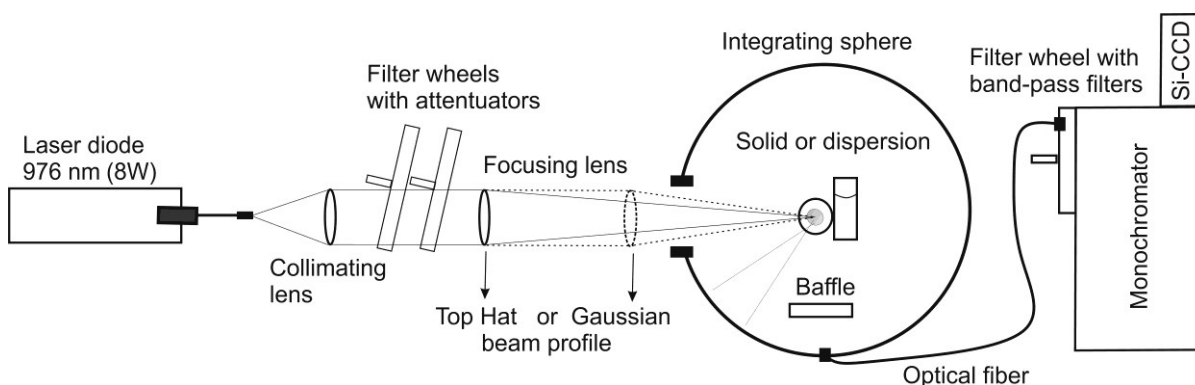


**Figure 4.1** Schematic presentation of the ISS for the absolute determination of the  $\Phi_{UC}(P)$  for UC powder and UC dispersions. The setup is divided into an excitation channel including the 8W 976 nm laser diode, filter wheels with attenuators with known transmission for controlled attenuation of the excitation light and focusing optics, and a detection channel including the integration sphere coupled into a filter wheel (equipped with band pass filters), monochromator, and a Si-CCD detector. The sample was mounted in the center of the integrating sphere. Reprinted from Kaiser et al.<sup>40</sup> with permission from The Royal Society of Chemistry.

### Excitation channel

The excitation source is a special customized optical fiber-coupled laser diode (from *Roithner Lasertechnik GmbH*) fulfilling the requirements for the absolute measurement of  $\Phi_{UC}(P)$  for  $\text{NaYF}_4:\text{Yb}^{3+},\text{Er}^{3+}$  UC crystals. These requirements include a high power of 8 W for characterizing the nonlinearity of the UC process, an adjusted emission wavelength of 976.4 nm that is resonant with the ground state absorption of  $\text{Yb}^{3+}$  ( $^2F_{7/2} \rightarrow ^2F_{5/2}$ ) and a high power stability  $< 0.1\%$  (see Figure 4.2) as prerequisite for minimum fluctuations of the absolute  $\Phi_{UC}$  measurements.

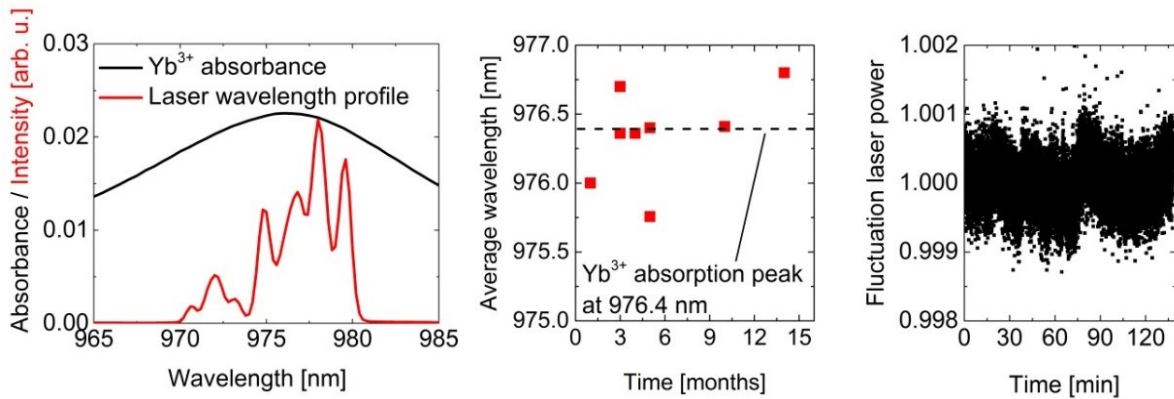


**Figure 4.2 Characterization results of the 976 nm laser diode used for  $\Phi_{UC}$  measurements:**  
a) Wavelength-dependent absorbance of  $\text{Yb}^{3+}$  (976.4 nm,  $^2F_{7/2} \rightarrow ^2F_{5/2}$ ) (black line) and wavelength profile of the 976 nm laser diode with a FWHM of about 5 nm (red line), which was adjusted to be resonant to the  $\text{Yb}^{3+}$  ground state absorption; b) Intensity averaged wavelength of the laser beam wavelength with a stability  $< 0.4$  nm over a period of over 1 year; c) Laser power with a stability  $< 0.1\%$  for over 120 minutes. Reprinted from Kaiser et al.<sup>40</sup> with permission from The Royal Society of Chemistry.

The laser light from the 200  $\mu\text{m}$ -sized output slit of the optical multimode-fiber was collimated and then focused on the sample. In order to investigate excitation beam profile (BP)-dependent effects on  $\Phi_{UC}$ , two different excitation geometries were realized by using focal lenses with focal lengths of 500 mm and 125 mm to obtain a nearly homogenous Top Hat BP ( $\text{TH}_{\text{exp}}$ ) and an inhomogeneous Gaussian BP ( $\text{Gauss}_{\text{exp}}$ ), respectively (see Figure 4.3). The  $P$  tuning range of the  $\text{TH}_{\text{exp}}$  is from  $0.25 \text{ Wcm}^{-2}$  to  $410 \text{ Wcm}^{-2}$  and for the  $\text{Gauss}_{\text{exp}}$  from  $2.5 \text{ Wcm}^{-2}$  to  $3400 \text{ Wcm}^{-2}$ , thus, allowing to tune  $P$  over four orders of magnitude. To guarantee maximal stability of  $P$ , the laser power was attenuated by two automated filter wheels equipped with reflective neutral density filters, which were placed between the collimating and focusing optics. To avoid damage of the laser diode by directly back-reflected

## 4. Samples and Experimental Methods

laser light, these filter wheels were tilted by a small angle. Furthermore, for safety reasons the reflected laser light was guided into a beam dump. In order to control the filter wheels, the monochromator, and to readout the detector, a Labview program was written with the help of the former bachelor student Nils Handelsmann from the BAM.

### Beam profile characterization

In order to verify BP-dependent effects on the  $\Phi_{UC}(P)$ , the two realized excitation geometries TH<sub>exp</sub> and Gauss<sub>exp</sub> (see Figure 4.3 a)) were systematically characterized with a beam profiler (*Newport LBP2*; pixel size: 8 x 9.3  $\mu\text{m}$ ). Therefore, cross-sections perpendicular to the beam propagation were recorded in 1 mm steps for a path length of 10 mm illustrated in Figure 4.3 b). The average beam diameter was defined at a 4 % intensity drop of the peak intensity of the in direction of the laser beam propagation averaged intensity (see Figure 4.3 c)) to ensure comparable  $\Phi_{UC}$  for a biphotonic emitter at the same averaged  $P$  values. This resulted in beam diameters of 1.4 mm and 0.55 mm for TH<sub>exp</sub> and Gauss<sub>exp</sub>, respectively.

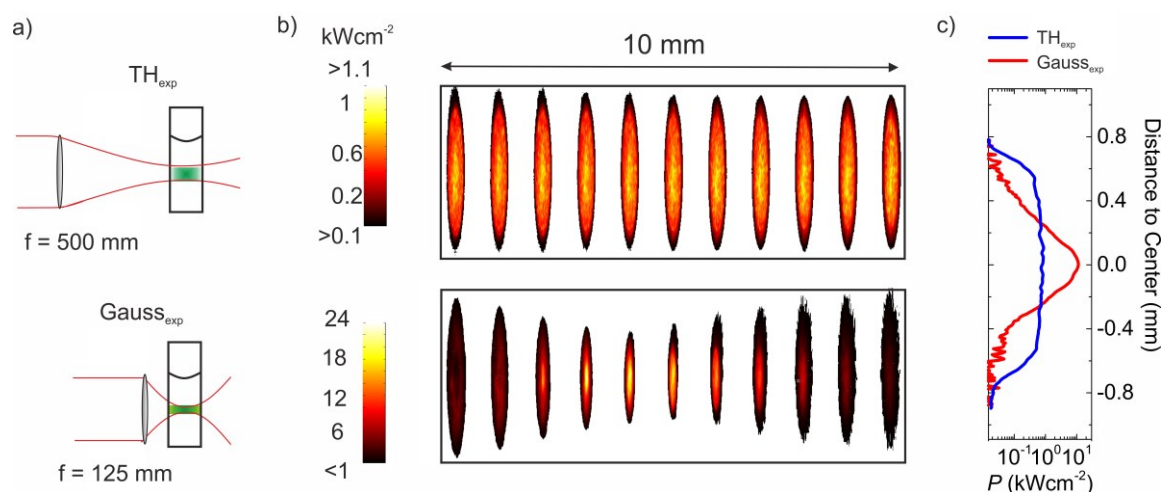


**Figure 4.3** Experimentally realized illumination geometries used for the investigation of the influence of the beam shape on the  $\Phi_{UC}(P)$  measurements. a) Schematic of the realization of TH<sub>exp</sub> BP (Top) and Gauss<sub>exp</sub> BP (Bottom) by the use of focal lenses with 500 mm and 125 mm focal length, respectively; b) Cross-sections of the  $P$ -distribution of TH<sub>exp</sub> (Top) and Gauss<sub>exp</sub> (Bottom) determined experimentally in 1 mm steps for a path length of 10 mm; c) Averaged  $P$ -distribution in the propagation direction of the laser beam for TH<sub>exp</sub> and Gauss<sub>exp</sub> for a laser power of 8 W. Reprinted from Kaiser et al.<sup>40</sup> with permission from The Royal Society of Chemistry.



##### Detection channel

The first part of the detection channel is a BaSO<sub>4</sub> inner-coated integrating sphere (from *Labsphere*) with a diameter of 15 cm, reflection over 97% in the vis to NIR spectral region), in which the sample was center-mounted with a BaSO<sub>4</sub> coated sample holder. At the bottom of the integrating sphere an optical fiber was attached guiding the light into a monochromator (Shamrock 303i, grating with blaze angle of 500 nm, spectral resolution 0.5 nm, *Andor Technology PLC*) equipped with a filter wheel and a silicon-based charged-coupled-device (Si-CCD) detector (Andor iDus CCD DU420-BRDD, 1024 x 256 Pixel with a pixel width of 26  $\mu\text{m}$ , *Andor Technology PLC*). A BaSO<sub>4</sub>-coated baffle was placed inside the integrating sphere above the optical fiber to ensure that only diffusely reflected light was detected. The filter wheel was equipped with five different bandpass filters to suppress overexposure by stray light of the intense laser light and to cover the complete wavelength region from 370 nm - 900 nm for the UCL detection. The laser light was recorded with a calibrated absorptive neutral density filter with an attenuation factor of 5,600.

##### Calibration of the detection channel

The wavelength calibration and spectral calibration of the detection channel was performed according to previously reported protocols.<sup>12, 150</sup> Therefore, a correction function for the wavelength scale was created by using a Hg-Ar discharge lamp from *Ocean Optics* (HR4000CG-UV-NIR). This included the recording of the spectral atomic lines with the ISS and comparison with the atomic spectra database from the *National Institute of Standard and Technology* (NIST). This correction function was then used for all further measurements. The optical response of the detection system was calibrated with a spectral radiance transfer standard, which wavelength dependence ( $L_\lambda(\lambda)$ ) was calibrated against a black body radiator by *The National Metrology Institute of Germany* (PTB). This spectral radiance transfer standard consists of a halogen lamp mounted inside an integrating sphere, to guarantee a diffuse spectral radiance. In order to determine the spectral instrument response functions, the spectrum of the spectral radiance standard was recorded from 350 nm - 1050 nm for all different bandpass filters used in the detection filter wheel. The obtained instrument response functions were then multiplied with  $\lambda/hc_0$  to obtain correction functions in units of spectral photon flux  $\text{s}^{-1}\text{m}^{-2}\text{nm}^{-1}$ . Additionally, an intensity correction function for different illumination times of the Si-CCD detector has been recorded. The validation of the instrument response functions was performed by recording and comparing the intensity corrected spectra of the certified spectral emission standards F003 - F005 from the BAM.<sup>151</sup> In order to control the filter wheels, the monochromator, and to readout the detector, a Labview

---

## 4. Samples and Experimental Methods

---

program was written with the help of the former bachelor student Nils Handelsmann from the BAM. Moreover, this program performed an automatic correction of the wavelength scale and the spectral sensitivity of the readout data of the detector. Furthermore, the complete analysis of the data, see 4.2.1.2 *Data analysis*, was automatized with an additionally self-written Labview program.

### Sample cells

All sample cells consist of high-quality quartz suprasil (QS) glass with an optical transmission > 80% from 200 nm – 2500 nm. Small sample volumes have been used to suppress indirect excitation and reabsorption effects (see 5.1. *Measurement conditions for  $\Phi_{UC}(P)$* ). The UCNPs dispersion samples were filled into 10 mm (inner length) x 4 mm (inner thickness) quartz cuvettes purchased from *Hellma GmbH*. As a blank sample, i.e. reference, a cuvette filled only with the pure solvent was used. The powder samples were pressed into 5 mm (inner diameter) x 0.1 mm (inner thickness) custom-designed round quartz cuvettes produced by *Hellma GmbH*. In this case, an empty round cuvette was used as a blank sample. Identical measurement positions were ensured using the reflection with a Helium-Neon (He-Ne)-laser.

### 4.2.1.2 Data analysis

In this subsection the analysis of the data obtained with the ISS is described. First, the calculation of the  $P$ -dependent  $\Phi_{UC}$  is presented. Second, the further analysis of the  $P$ -dependent UC emission spectra is detailed, which reveal additional information in respect photonic order and the (de-)population pathways regarding the different UC emission bands.

### Calculation of the $P$ -dependent upconversion quantum yield ( $\Phi_{UC}(P)$ )

The  $P$ -dependent  $\Phi_{UC}$  curve can be calculated as the quotient of the emitted and the absorbed photon flux, see Equation 4.1. This calculation requires the measurement of a) the  $P$ -dependent spectrally-corrected sample spectrum ( $I_{\text{sample}}(\lambda, P)$ ) and b) the  $P$ -dependent spectrally-corrected blank sample spectrum ( $I_{\text{blank}}(\lambda, P)$ ).

$$\Phi_{UC}(P) = \frac{\text{emitted UC photon flux}}{\text{absorbed photon flux}} = \frac{\int_{350 \text{ nm}}^{900 \text{ nm}} I(\lambda, P) d\lambda}{\int_{968 \text{ nm}}^{982 \text{ nm}} I_{\text{abs}}(\lambda, P) d\lambda} = \frac{\int_{350 \text{ nm}}^{900 \text{ nm}} I_{\text{sample}}(\lambda, P) - T I_{\text{blank}}(\lambda, P) d\lambda}{\int_{968 \text{ nm}}^{982 \text{ nm}} I_{\text{blank}}(\lambda, P) - I_{\text{sample}}(\lambda, P) d\lambda}$$

with  $T = \frac{\int_{968 \text{ nm}}^{982 \text{ nm}} I_{\text{sample}}(\lambda, P) d\lambda}{\int_{968 \text{ nm}}^{982 \text{ nm}} I_{\text{blank}}(\lambda, P) d\lambda}$

**Equation 4.1**

The  $P$ -dependent spectral photon flux ( $I(\lambda, P)$ ), needed for the calculation of the emitted UC photon flux, was determined with a stray light correction from the excitation light of  $I_{\text{sample}}(\lambda, P)$ . Therefore,  $I_{\text{sample}}(\lambda, P)$  was subtracted by  $I_{\text{blank}}(\lambda, P)$  multiplied with a factor  $T$  to resulting to  $I(\lambda, P)$ . Thereby, the factor  $T$  considers scattering of the narrow band intense excitation light inside the detection monochromator. This can result in artefacts in the emission spectra, and subsequently, affects the calculated  $\Phi_{\text{UC}}$ . Particularly, for weakly emissive UC samples this stray light correction has to be considered. The emitted absolute photon flux,  $I(\lambda, P)$  was then calculated by integration from 350 nm - 900 nm, thereby including all UC emission bands of  $\text{Er}^{3+}$  and omitting the sensitizer  $\text{Yb}^{3+}$  luminescence above 900 nm. The absorbed absolute photon flux was obtained by integrating the absorbed photon flux  $I_{\text{abs}}(\lambda, P)$ , equaling the difference of  $I_{\text{blank}}(\lambda, P)$  and  $I_{\text{sample}}(\lambda, P)$ , over the wavelength range of the excitation peak, here 968 nm - 982 nm (see Figure 4.2 a)).

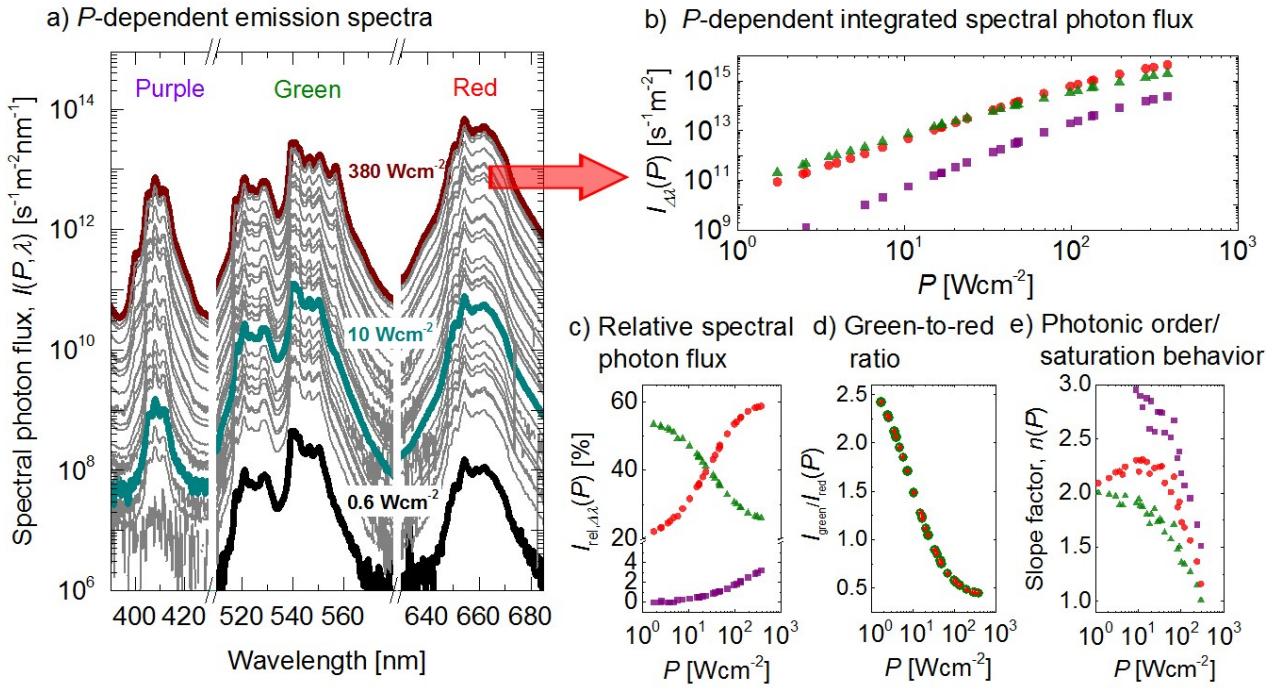
#### **Analysis of the $P$ -dependent spectral photon flux $I(\lambda, P)$**

Figure 4.4 a) presents a set of  $I(\lambda, P)$  for a respective UC sample for a broad  $P$ -range. This set of  $I(\lambda, P)$  can be used to obtain the following parameters providing information on of the UC processes for the different  $\text{Er}^{3+}$  emission bands: i)  $P$ -dependent integrated spectral photon fluxes ( $I_{\Delta\lambda}(P)$ ), ii)  $P$ -dependent relative spectral photon fluxes ( $I_{\text{rel}, \Delta\lambda}(P)$ ), iii)  $P$ -dependent green-to-red ratios ( $I_{\text{green}}/I_{\text{red}}(P)$ ), and iv)  $P$ -dependent slope factors ( $n(P)$ ) (see Figure 4.4 b), c), d) and e)). In the following these parameters are defined.

#### **$P$ -dependent integral spectral photon flux ( $I_{\Delta\lambda}(P)$ )**

The  $P$ -dependent integral spectral photon flux ( $I_{\Delta\lambda}(P)$ ) was determined for each  $\text{Er}^{3+}$  emission band by integrating  $I(\lambda, P)$  over the integration intervals presented in Table 4.2. The  $I_{\Delta\lambda}(P)$  of the  $\text{Er}^{3+}$  green, red and purple emission bands are presented for a respective UC sample in Figure 4.4 b).

#### 4. Samples and Experimental Methods



**Figure 4.4** Parameters derived from the  $P$ -dependent spectral photon flux ( $I(\lambda, P)$ ): a)  $I(\lambda, P)$  of  $\text{Er}^{3+}$  purple ( $^2\text{H}_{9/2} \rightarrow ^4\text{I}_{15/2}$ ),  $\text{Er}^{3+}$  green ( $^2\text{H}_{11/2}, ^4\text{S}_{3/2} \rightarrow ^4\text{I}_{15/2}$ ) and  $\text{Er}^{3+}$  red ( $^4\text{F}_{9/2} \rightarrow ^4\text{I}_{15/2}$ ) emission bands with  $P$  varying from 0.6  $\text{Wcm}^{-2}$  to 380  $\text{Wcm}^{-2}$  for a representative UCNP sample; b)  $P$ -dependent integral spectral photon flux ( $I_{\Delta\lambda}(P)$ ); c)  $P$ -dependent relative spectral photon flux ( $I_{\text{rel},\Delta\lambda}(P)$ ) presenting changes in the population density of the respective emissive states; d)  $P$ -dependent green-to red ratio ( $I_{\text{green}}/I_{\text{red}}(P)$ ); e)  $P$ -dependent slope factors ( $n(P)$ ) revealing the photonic order and saturation behavior of the UC process.

**Table 4.2** Intervals for integration of the intensity of the  $\text{Er}^{3+}$  UC emission bands.

$\Delta\lambda$ , color/center wavelength	Electronic transition	Integration interval
UV/380 nm	$^4\text{G}_{11/2} \rightarrow ^4\text{I}_{15/2}$	372 nm - 394 nm
Purple/410 nm	$^2\text{H}_{9/2} \rightarrow ^4\text{I}_{15/2}$	394 nm - 430 nm
Green/520nm,540 nm	$^2\text{H}_{11/2}, ^4\text{S}_{3/2} \rightarrow ^4\text{I}_{15/2}$	510 nm - 570 nm
Red/655 nm	$^4\text{F}_{9/2} \rightarrow ^4\text{I}_{15/2}$	630 nm - 685 nm
NIR 1/810 nm	$^4\text{I}_{9/2} \rightarrow ^4\text{I}_{15/2}$	783 nm - 833 nm
NIR 2/850 nm	$^2\text{H}_{11/2}, ^4\text{S}_{3/2} \rightarrow ^4\text{I}_{13/2}$	833 nm - 880 nm
<b>Overall UCL intensity</b>		370 nm - 900 nm

### **$P$ -dependent relative spectral emission intensity ( $I_{\text{rel},\Delta\lambda}(P)$ )**

The  $P$ -dependent relative spectral emission intensity ( $I_{\text{rel},\Delta\lambda}(P)$ ) is defined by the quotient of  $I_{\Delta\lambda}(P)$  to the overall UC photon flux ( $I_{\lambda\text{all}}(P)$ ), see Equation 4.2.

$$I_{\text{rel},\Delta\lambda}(P) = \frac{I_{\Delta\lambda}(P)}{I_{\lambda\text{all}}(P)} = \frac{\int_{\lambda_{\text{em,low}}}^{\lambda_{\text{em,up}}} I(\lambda, P) d\lambda}{\int_{350 \text{ nm}}^{900 \text{ nm}} I(\lambda, P) d\lambda} \quad \text{Equation 4.2}$$

Here,  $\lambda_{\text{em,up}}$  and  $\lambda_{\text{em,low}}$  present the wavelengths of the upper and lower bounds used for the integration of the UC emission bands, see Table 4.2. The  $I_{\text{rel},\Delta\lambda}(P)$  of the  $\text{Er}^{3+}$  green, red and purple emission bands are presented in Figure 4.4 c).

$I_{\text{rel},\Delta\lambda}(P)$  provides information about the population density of the respective energy levels in dependence of  $P$ . The shape of  $I_{\text{rel},\Delta\lambda}(P)$  was used to optimize rate equation constants in Publication II and III. Moreover, the crossing point of the  $\text{Er}^{3+}$  green and red intensity, see Figure 4.4 c), was recently used as indication point for the UC efficiency for  $\beta\text{-NaYF}_4\text{:Yb}^{3+}, \text{Er}^{3+}$  UC systems with similar  $\text{Yb}^{3+}$  and  $\text{Er}^{3+}$  dopant concentrations.<sup>39</sup>

It should be noted, to avoid misunderstandings, that in Publications I and II  $I_{\text{rel},\Delta\lambda}(P)$  referred to  $I_{\Delta\lambda}(P)$ . The nomenclature defined in this thesis is in accordance to the nomenclature used in Publication III.

### **Green-to-red ratio ( $I_{\text{green}}/I_{\text{red}}$ )**

$I_{\text{green}}/I_{\text{red}}(P)$  is the  $P$ -dependent ratio of the integral photon flux of the  $\text{Er}^{3+}$  green (520,540 nm,  $^2\text{H}_{11/2}, ^4\text{S}_{3/2} \rightarrow ^4\text{I}_{15/2}$ ) to  $\text{Er}^{3+}$  red (655 nm,  $^4\text{F}_{7/2} \rightarrow ^4\text{I}_{15/2}$ ) emission intensity, see Equation 4.3 and Figure 4.4 d).

$$I_{\text{green}}/I_{\text{red}}(P) = \frac{\int_{510 \text{ nm}}^{570 \text{ nm}} I(\lambda, P) d\lambda}{\int_{630 \text{ nm}}^{685 \text{ nm}} I(\lambda, P) d\lambda} \quad \text{Equation 4.3}$$

This quantity is commonly used by the UC community to compare the properties of UC samples with similar material composition and size. A high  $I_{\text{green}}/I_{\text{red}}(P)$  for  $\text{Yb}^{3+}, \text{Er}^{3+}$ -based upconverters can account for low nonradiative rates as the red emissive energy level can be directly fed from the  $\text{Er}^{3+} ^2\text{H}_{11/2}, ^4\text{S}_{3/2}$  energy level *via* nonradiative relaxation (see Figure 2.7).

---

### Slope factor ( $n(P)$ )

The  $P$ -dependent slope factor ( $n(P)$ ) represents the nonlinear increase of the emission intensity with  $P$  (see Equation 4.4 and Equation 4.5). At low  $P$ ,  $n(P)$  typically presents the photonic order of the UC process. For example, in case of a biphotonic process  $n(P)$  equals two at low  $P$ . Saturation of the UC process at higher  $P$  results in a decrease of  $n(P)$ . For the calculation of  $n(P)$  energetically neighboring data points  $I(P_1), I(P_2)$  were used, see Figure 4.4 b) and Figure 4.4 e) and Equation 4.6.

$$I(P) \propto P^{n(P)} \quad \text{Equation 4.4}$$

$$n(P) = \frac{d \log (I(P))}{d \log (P)} \quad \text{Equation 4.5}$$

$$n(P) = \frac{\log (I(P_2)) - \log (I(P_1))}{\log (P_2) - \log (P_1)} \quad \text{Equation 4.6}$$

An energy level can also be populated by a mixture of processes with different photonic orders like the  $\text{Er}^{3+}$  red emissive  $^4\text{F}_{9/2}$  energy level, which can be populated *via* bi- and triphotonic processes, see Figure 2.6. Such mixtures of different photonic population processes can be characterized *via* the shape of  $n(P)$  of the  $\text{Er}^{3+}$  red emission band, see Figure 4.4 e).

### 4.2.2 Time-resolved photoluminescence spectroscopy

The lifetime curves of the emissive energy levels, characterized by their rise and decay behaviors (see Figure 4.5), provide information about the temporal evolution of the population and depopulation processes. Measurements of the lifetime curves were performed with a commercial *Edinburgh Instruments* spectrofluorometer FSP-920. This setup was equipped with an electrically-pulsed 1 W 978 nm laser diode (950  $\mu\text{s}$  long square pulse) to excite the sensitizer  $\text{Yb}^{3+}$  ions for the determination of the UCL lifetime curves for the  $\text{Er}^{3+}$  380 nm, 410 nm, 520/540 nm, 655 nm, 810 nm and the downshifted (DS) lifetime curve of the 1520 nm emission bands. Additionally, DS luminescence lifetimes were determined by directly exciting the  $\text{Er}^{3+}$  ions with an electrically pulsed xenon lamp (pulse width *ca.* 1  $\mu\text{s}$ ) combined with an excitation double monochromator to select the respective excitation wavelength. This provided the DS luminescence curves of the  $\text{Er}^{3+}$  410, nm, 520/540 nm, 655 nm emission bands. Moreover, the DS lifetime of  $\text{Yb}^{3+}$  976 nm emission

#### 4.2.2 Time-resolved photoluminescence spectroscopy

band was determined with excitation wavelength of 940 nm. The detection channel was also equipped with a double monochromator to select the respective emission wavelength for detection. The luminescence lifetime curves were then recorded with a red extended photomultiplier tube (PMT) (R2658P) for the UV-NIR region, and a nitrogen cooled NIR PMT (R5509P) for the  $\text{Er}^{3+}$  1520 nm emission band. Distortion by stray light or undesired intensity of other emission bands were canceled out by using different band pass filters.

In order to estimate the influence of the long-pulse excitation of the above described setup, I also performed short-pulse measurements with a setup of the work group of Prof. Dr. Hoffmann from the *Technical University of Berlin* for the UC samples investigated in Publication I. Here, luminescence lifetime curves were obtained with short pulse excitation with pulse lengths of *ca.* 10 ns and an excitation wavelength of 940 nm using a dye (IR140) laser pumped with an excimer laser, see Figure 4.6. The deviations of the derived decay times for short- and long-pulse excitation using a differential method, see Supporting Information of Publication I, were < 10%.

It should be noted that the determined UC lifetimes are always results of combinations of decay and ET processes.<sup>152</sup> Furthermore, DS decay lifetimes can be affected by CR processes.<sup>152</sup> This underlines the fact that only with aid of a comprehensive rate equation analysis, taking into account the significant interaction between the  $\text{Yb}^{3+}$  and  $\text{Er}^{3+}$  energy levels, the population and depopulation dynamics can be described accurately as done in Publications II and III.

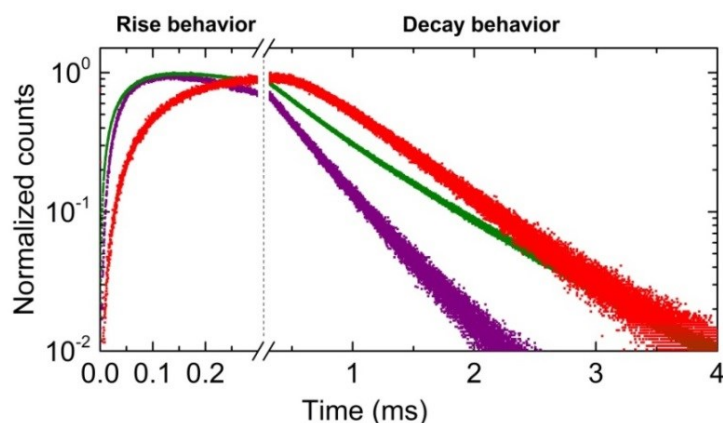


**Figure 4.5** Temporal rise and decay behavior of  $\mu\text{m}$ -sized  $\beta\text{-NaYF}_4\text{:Yb}^{3+}(21\%),\text{Er}^{3+}(2\%)$  UC particles for the  $\text{Er}^{3+}$  purple at 410 nm ( $^2\text{H}_{9/2} \rightarrow ^4\text{I}_{15/2}$ ),  $\text{Er}^{3+}$  green 520 nm/540 nm ( $^2\text{H}_{11/2}, ^4\text{S}_{3/2} \rightarrow ^4\text{I}_{15/2}$ ) and 655 nm ( $^4\text{F}_{9/2} \rightarrow ^4\text{I}_{15/2}$ ) emission bands. The lifetime curves were obtained using a dye (IR140) laser pumped with an excimer laser with short pulse excitation of 10 ns with an excitation wavelength of 940 nm with a setup from the work group of Prof. Dr. Hoffmann from the *Technical University of Berlin* (TU-Berlin).

---

---



---

## 5 Measurement Strategies for the $P$ -dependent

### $\Phi_{UC} (\Phi_{UC}(P))$

In this chapter prerequisites and challenges for absolute  $P$ -dependent  $\Phi_{UC}$  measurements with the custom-built ISS (see 4.2.1 *Integrating sphere setup (ISS)*) are presented for  $\beta$ -NaYF<sub>4</sub>:Yb<sup>3+</sup>,Er<sup>3+</sup> UC crystals. The first part of this chapter addresses stringent requirements for the optical properties of the sample, the measurement geometry, and measurement procedure. In the second part, the  $\Phi_{UC}(P)$  values of  $\mu$ m-sized  $\beta$ -NaYF<sub>4</sub>:Yb<sup>3+</sup>(21%),Er<sup>3+</sup>(2%) UC particles (UC $\mu$ P) are validated by comparison to experimental and theoretical literature data.

#### 5.1. Measurement conditions for $\Phi_{UC}(P)$

In this section, the prerequisites and measurement strategies of the  $\Phi_{UC}$  measurement are detailed. Disregarding these recommendations can lead to a high fluctuation, systematic underestimation or overestimation of the measured  $\Phi_{UC}$  values. The following instructions present a guideline for accurate  $P$ -dependent  $\Phi_{UC}$  measurements with minimum uncertainty.

##### Absorption of the UC sample

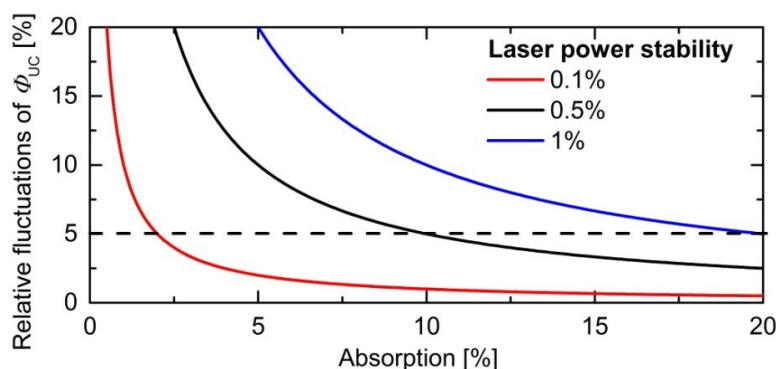
An accurate  $\Phi_{UC}$  measurement can be only guaranteed for a UC sample with a suitable absorption. This parameter can be tuned by either varying the particle concentration or the optical path length. The lower measuring limit of the UC sample absorption sensitively depends on the stability of the excitation source and on the reproducibility of measurement conditions of the sample and the blank. Whereas, the upper measuring limit depends on the optical path length and nonlinearity of the UC material.

Figure 5.1 shows that with the use of a high-stability excitation source of 0.1%, as utilized in this work, see Figure 4.2 c), a reasonable  $\Phi_{UC}$  determination requires UC samples with an absorption larger than 1% to minimize fluctuation of a single  $\Phi_{UC}$  measurement down to 10%. However, systematic errors regarding the positioning, the preparation and the optical properties of the sample and the blank must also be considered. Although identical positioning can be ensured with the reflection of a He-Ne laser, small slight deviations of the reflectance of the quartz cuvettes from about 0.1% - 0.4% showed to be a crucial uncertainty source at low UC sample absorptions. Therefore, a **lower limit of 5%** for the absorption of the UC sample is recommended to minimize these systematic errors. In case of UCNPs

## 5 Absolute Upconversion Quantum Yield ( $\Phi_{UC}$ ) Measurements: Conditions and Validation

dispersions with very low particle concentrations, this recommendation may not be fulfilled. However, the use of the same quartz cuvette for UC sample and blank has still proven to be moderately precise for absorption measurements down to 2%.

A strong absorptive UC sample can lead to attenuation of the laser beam inside the sample volume resulting to inhomogeneous spatial emission for these nonlinear emitters. To minimize this effect, an **upper limit of about 20%**, for the absorption of the UC sample with an optical path length of 10 mm is recommended.



**Figure 5.1** Relative fluctuations for a single  $\Phi_{UC}$  measurement in dependence of the fraction of absorbed light for different laser power stabilities. The 976 nm laser diode used for the absolute  $\Phi_{UC}$  measurements in this thesis has a power stability  $< 0.1\%$ . The relative fluctuations of the  $\Phi_{UC}$  measurements were calculated from the quotient of the relative laser power stability to the relative absorption of the UC sample.

### Scattering of the UC sample

Another common issue, for  $\Phi_{UC}$  measurements, results from the scattering of the excitation light by the UC sample. Particularly, scattering can critically influence the  $\Phi_{UC}$  measurements for i) dispersions with UCNPs sizes larger than 50 nm or agglomerated UCNPs and ii) for powder samples. Additionally, scattering of the excitation light by UCNPs dispersion can lead to a lowered  $P$  inside the sample volume, and hence, results in underestimated  $\Phi_{UC}$  values. Therefore, it was ensured for all investigated UCNPs dispersions that no detectable scattering occurs at the excitation wavelength, see Figure 5.2.

Light scattering by powder samples can lead either to a decrease of  $P$ , due to a diffusion of the incident light, or even to an increase of  $P$  by multiple reflections, dependent on the preparation of the powder sample. In order to minimize internal scattering effects, the powder samples were prepared in thin cell cuvettes having an inner thickness of 100  $\mu\text{m}$ . In addition, the sample holder, placed in the center of the integrating sphere, was tilted by  $30^\circ$  to avoid that diffuse back-scattered excitation light leave the integrating sphere *via* the

## 5.1. Measurement conditions for $\Phi_{UC}(P)$

entrance port. This excitation geometry has the advantage that there is no need for a non-absorbing reference sample with similar scattering properties compared to the powder sample, since most of the reflected incident light is collected with the integrating sphere.

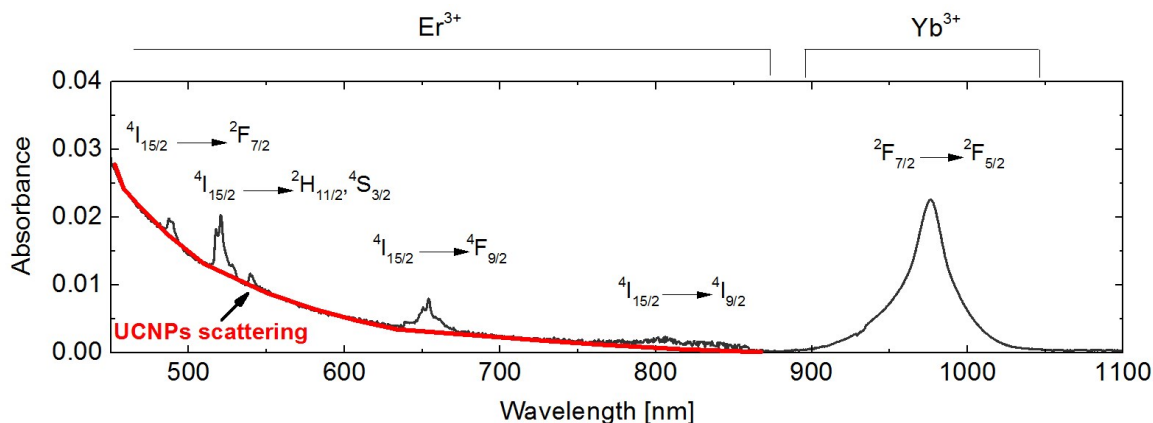


**Figure 5.2** Absorbance spectra of 25 nm-sized UCNPs dispersed in toluene taken from Publication I. This shows the absence of scattering at the excitation wavelength of 976 nm for this UCNPs dispersion, ensuring no effect on the measured  $\Phi_{UC}$ . Reprinted from Kaiser et al.<sup>40</sup> with permission from The Royal Society of Chemistry.

### Yb<sup>3+</sup> 980 nm emission ( $^4F_{5/2} \rightarrow ^4F_{7/2}$ )

Figure 5.3 a) schematically shows the distortion of the measured absorption, due to the overlap of emitted light from the sensitizing Yb<sup>3+</sup> ion with excitation light. This issue was addressed by subtracting the emitted intensity of Yb<sup>3+</sup> from the recorded intensity.<sup>132</sup> Therefore, the real shape of the Yb<sup>3+</sup> 980 nm emission band was measured separately with an excitation wavelength < 950 nm and then normalized to the distorted recorded sample spectrum. Fischer et al. reported deviations of up to 40% for  $\Phi_{UC}$  of core-shell UCNPs between Yb<sup>3+</sup> emission-corrected and -uncorrected values.<sup>132</sup> For the UCNPs studied in this work, no Yb<sup>3+</sup> 980 nm emission-correction was necessary, as the Yb<sup>3+</sup> emission intensity is weak for these unshelled systems.<sup>40</sup> In case of the  $\mu\text{m}$ -sized  $\beta\text{-NaYF}_4\text{:Yb}^{3+},\text{Er}^{3+}$  particles (UC $\mu$ P), investigated in Publication I, a Yb<sup>3+</sup> 980 nm emission-correction was required. The relative deviations of Yb<sup>3+</sup> emission-corrected to -uncorrected absorption as well as associated  $\Phi_{UC}$  values additionally show a  $P$  dependence with 14% at a  $P$  of 0.2 Wcm<sup>-2</sup> down to 3% for a  $P$  of 100 Wcm<sup>-2</sup>, see Figure 5.3 b) and c).

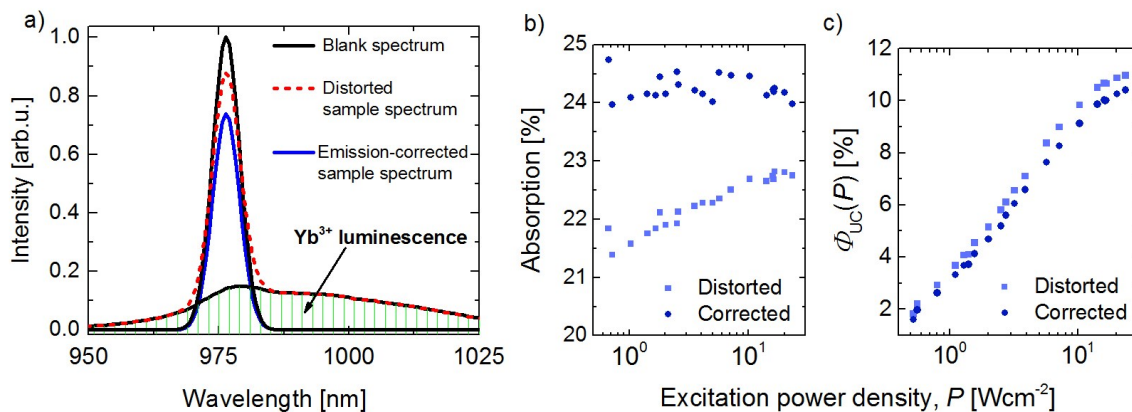


**Figure 5.3** Emission-correction method of the  $\Phi_{UC}(P)$  for the intensity of the  $\text{Yb}^{3+}$  980 nm emission band ( $^4\text{F}_{5/2} \rightarrow ^4\text{F}_{7/2}$ ). a) Schematic of the  $\text{Yb}^{3+}$  emission-correction method including the  $\text{Yb}^{3+}$  980 nm emission band (black line, area under curve in shaded green), blank spectrum (black line), distorted sample spectrum (dashed red line) and  $\text{Yb}^{3+}$  980 nm emission-corrected sample spectrum (blue line); b)  $\text{Yb}^{3+}$  emission-corrected absorption values and c)  $\text{Yb}^{3+}$  emission-corrected  $\Phi_{UC}(P)$  values; of the UCuP sample studied in Publication I. Reprinted from Kaiser et al.<sup>40</sup> with permission from The Royal Society of Chemistry.

### Reabsorption and indirect excitation

Multiple diffuse reflections inside the integrating sphere can lead to *reabsorption* of the emitted light and *indirect absorption* of the excitation light by the UC sample. Thereby, reabsorption can reduce the emitted photon flux, whereas indirect excitation is associated with a very low  $P$ , both leading to underestimated  $\Phi_{UC}$  values. These values can be corrected with a method developed by MacDougall et al.,<sup>153</sup> who extended the widely known reabsorption-correction for linear emitters developed from de Mello.<sup>154</sup> However, these effects can be easily circumvented by minimizing the sample volume compared to the integrating sphere volume, making the events of reabsorption and indirect excitation negligible, and thus, a correction obsolete. Suitable sample cell sizes can be determined by measuring  $\Phi_{UC}$  for a series of sample cells with varied volumes.

### Excitation beam profile (BP)

Linear emitters like fluorescent dyes and QDs do not need any consideration of the  $P$ -inhomogeneity of the BP. However, UCL depends strongly on  $P$ . Consequently, an inhomogeneous BP results in a distribution of  $\Phi_{UC}(P)$  for these nonlinear emitters.

These BP-dependent effects on the  $\Phi_{UC}(P)$  were quantified by a calculation using the experimentally realized BPs (see Figure 4.3). For this purpose, the formula of the Anderson

### 5.1. Measurement conditions for $\Phi_{UC}(P)$

Engels group for the  $\Phi_{UC}(P)$  of an ideal biphotonic emitter (see Equation 2.8) was extended by including the spatial  $P$ -distribution of the BP of the illuminated sample volume (detailed in Publication I). Figure 5.4 shows the  $P$ -dependent deviation of the  $\Phi_{UC}(P)$  for the experimentally realized TH<sub>exp</sub> and Gauss<sub>exp</sub> shaped BPs (see Figure 4.3) compared to an ideal Top Hat (TH<sub>ideal</sub>) shaped BP, i.e. a perfectly homogenous BP. At low  $P$ , The deviations of  $\Phi_{UC}(P)$  for Gauss<sub>exp</sub> and TH<sub>exp</sub> account to about 45% and 10%, respectively. This underlines the need for a homogeneous Top Hat BP for accurate  $\Phi_{UC}(P)$  measurement.

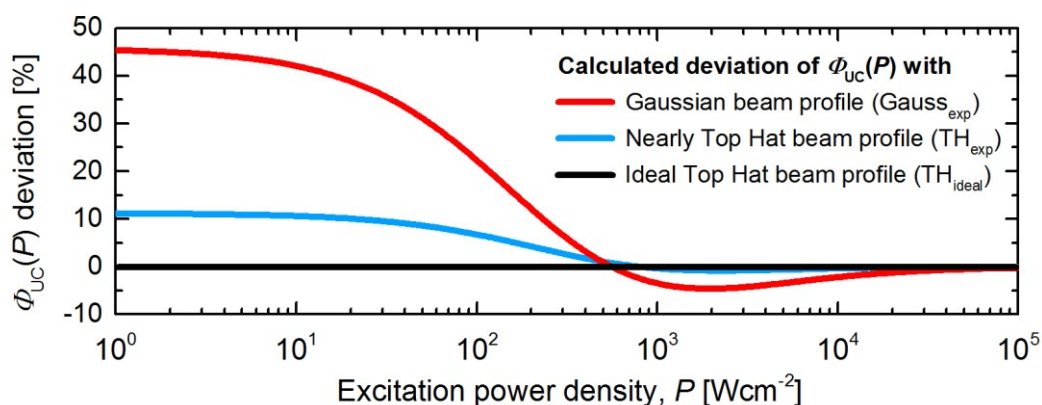


**Figure 5.4** Calculated deviation of  $\Phi_{UC}(P)$  for experimentally realized beam profiles. Here, the experimentally realized TH<sub>exp</sub> and Gauss<sub>exp</sub> BPs (see Figure 4.3) were compared to a TH<sub>ideal</sub> BP. At low  $P$ , the deviation of the simulated  $\Phi_{UC}(P)$  values obtained with the TH<sub>exp</sub> and Gauss<sub>exp</sub> BPs accounts for up to ca. 10% and 45%, respectively. Reproduced from Kaiser et al.<sup>40</sup> with permission from The Royal Society of Chemistry.

#### Heating effects at high laser power

The excitation of the UC sample with high laser powers is accompanied by an increase of its temperature. This results in a decrease of the measured  $\Phi_{UC}(P)$  due to thermal deactivation of the emissive Er<sup>3+</sup> energy levels. The heating of the UC sample depends on the measurement time, laser power, and beam diameter, as well as on the UC sample specific properties like size, absorptivity, crystalline quality, and the optical and thermal properties of its environment (e.g. absorption and heat capacity of the solvent). By using a short measurement time of less than 30 s, the thermally induced intensity loss was limited to maximally 30 % at the highest  $P$  used for the investigated UC samples studied. In particular, powder samples found to be quite prone to degradation for  $P > 130$  Wcm<sup>-2</sup> for the used beam diameters of sizes in the mm-range. Instead, smaller beam diameters in the  $\mu$ m-range used typically in microscopic studies allows excitation of UC powders with very high  $P$  of more than 10<sup>6</sup> Wcm<sup>-2</sup>.<sup>155</sup> UCNPs dispersions generally have a better heat transfer than powders

## 5 Absolute Upconversion Quantum Yield ( $\Phi_{UC}$ ) Measurements: Conditions and Validation

allowing excitation with laser powers of more than 8 W (used for the here investigated UCNPs dispersions) without harming the samples.

The property of UCNPs to act as nanothermometers allows monitoring the temperature increase for different  $P$ . Therefore, the temperature-dependent intensity-ratio  $I_{520nm}/I_{540nm}(T)$  of the thermally coupled  $Er^{3+}$  520 nm ( $^2H_{11/2} \rightarrow ^4I_{15/2}$ ) and 540 nm ( $^4S_{3/2} \rightarrow ^4I_{15/2}$ ) emission bands is utilized, see Figure 5.5 a).<sup>156, 157</sup> Note that the  $I_{520nm}/I_{540nm}(T)$  depends on many parameters, like e.g. size, solvent and dopant concentration of the UCNPs and has to be calibrated separately. Exemplarily, Figure 5.5 b) represent the temperature of UCNPs dispersed in water ( $H_2O$ ) and heavy water ( $D_2O$ ) for different  $P$ , excited with a Gauss<sub>exp</sub> BP for under 30 s, with an optical path length of 10 mm and a sample volume of about 1 ml. The drastic increase of the temperature from 25 °C to 60 °C of UCNPs dispersed in  $H_2O$ , at  $P = 1000 \text{ Wcm}^{-2}$ , mainly results from the high absorption of  $H_2O$  of 40% at 976 nm for the chosen 10 mm optical path length. This underlines the critical influence of absorbing solvents on the actual temperature of the sample for  $\Phi_{UC}$  measurements. In contrast, for UCNPs dispersed in  $D_2O$  the temperature increase is much less pronounced with 10° C at  $P = 1000 \text{ Wcm}^{-2}$ . This increase results solely from nonradiative deactivation processes of the UCNPs as  $D_2O$  does not absorb at the excitation light.

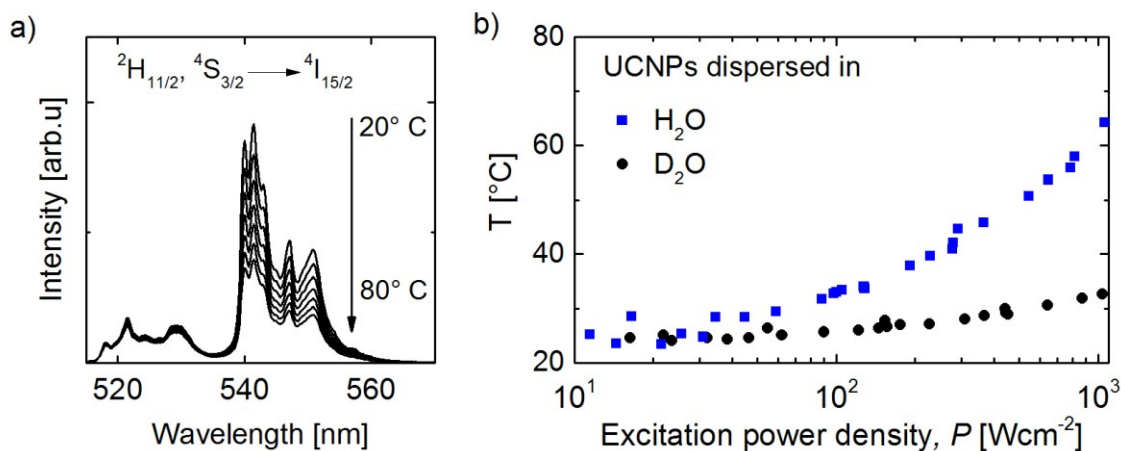


**Figure 5.5 Monitoring of the temperature increase of UCNPs by laser excitation during the  $\Phi_{UC}(P)$  measurement:** a) Temperature-dependent  $Er^{3+}$  520 nm to  $Er^{3+}$  540 nm emission intensity ratio  $I_{520nm}/I_{540nm}(T)$  from 20° C - 80° C separately recorded and used for calibration; b)  $P$ -dependent temperature increase for DSPE-capped UCNPs dispersed in  $H_2O$  (blue) and  $D_2O$  (black), for standard  $\Phi_{UC}$  measurement conditions described in the text, calculated with the  $I_{520nm}/I_{540nm}(T)$ . Reproduced from Würth, Kaiser et al.<sup>55</sup> with permission from The Royal Society of Chemistry.

#### **$\Phi_{UC}$ measurement in H<sub>2</sub>O at high $P$**

Accurate  $\Phi_{UC}$  of measurements for UCNPs dispersed in H<sub>2</sub>O are very challenging, since H<sub>2</sub>O has a high absorption coefficient at the excitation wavelength of 976 nm. This results in heating up of the UCNPs sample for high  $P$  (see Figure 5.5 b)) resulting in a decrease in intensity. Moreover, the absorption coefficient of H<sub>2</sub>O increases with increasing temperature,<sup>158</sup> which requires more specific measurement conditions for high  $P$  to avoid overestimation of the measured  $\Phi_{UC}$ . This implies that blank and sample spectrum must be recorded with the same illumination times to match their temperatures. Additionally, the absorption of the UCNPs dispersion should be kept low at *ca.* 5-10%, so that nonradiative deactivation processes minimally contribute to the increase of the temperature. In addition, the high absorption of H<sub>2</sub>O leads to a lowered average  $P$  and to an increase of the inhomogeneity of the BP. As discussed earlier in this section, an inhomogeneous BP leads to overestimated  $\Phi_{UC}$  values.

### 5.2 Validation of measured $\Phi_{UC}(P)$

The aim of this section is to validate the measured  $\Phi_{UC}(P)$  data by comparing with literature data obtained from different laboratories. For this purpose, high-quality bulk systems with similar dopant concentrations are the best choice due to their low nonradiative rates, and hence, well-comparable optical properties. As a representative bulk material, commercially available 3  $\mu\text{m}$ -sized  $\beta\text{-NaYF}_4\text{:Yb}^{3+}(21\%),\text{Er}^{3+}(2\%)$  UC particles (**UC $\mu\text{P}_{BAM}$** ) (from *Phosphor Technologies*)<sup>147</sup> were chosen. Reliable reports of  $\Phi_{UC}$  measurements of bulk  $\beta\text{-NaYF}_4\text{:Yb}^{3+},\text{Er}^{3+}$  are rare since these measurements are challenging, as intensively discussed in the previous sections of this thesis. Reported  $\Phi_{UC}$  data usually includes the intensity data of a limited number or even only for a single UC emission band. Furthermore, most works provide  $\Phi_{UC}$  data for small  $P$ -range  $< 2$  orders of magnitude or even only a single  $P$ , which is not enough to fully characterize the saturation behavior of the UC processes. Therefore, this work provided a comprehensive characterization of the  $\Phi_{UC}$  of **UC $\mu\text{P}_{BAM}$**  regarding the full spectral region from 360 - 900 nm, considering all UC emission bands with a significant contribution to the overall UCL, recorded for a wide  $P$  range of over three orders of magnitude with a well-characterized TH-shaped excitation beam profile.

Three reports were used for the comparison of the measured  $\Phi_{UC}(P)$  of **UC $\mu\text{P}_{BAM}$** . The first report from Page et al. (1997) provides the  $\Phi_{UC}(P)$  of the  $\text{Er}^{3+}$  green emission band ( $\Phi_{UC,\text{green}}(P)$ ) for  $\mu\text{m}$ -sized  $\beta\text{-NaYF}_4\text{:Yb}^{3+},\text{Er}^{3+}$  powder (**UC $\mu\text{P}_{Page}$** ).<sup>52</sup> However, the dopant concentration for **UC $\mu\text{P}_{Page}$**  was not specified. In the second report from the Van Veggel group, the maximal  $\Phi_{UC,\text{green}}$  for  $\beta\text{-NaYF}_4\text{:Yb}^{3+}(20\%),\text{Er}^{3+}(2\%)$  particles with sizes  $\gg 100$  nm (**UC $\mu\text{P}_{VanVeggel}$** ) was determined. Both of these reports used an ISS for the absolute  $\Phi_{UC}$  determination. The third report from the Berry group in 2014 provides simulated values of the spectral  $\Phi_{UC}(P)$ 's of different  $\text{Er}^{3+}$  emission bands of  $\mu\text{m}$ -sized rod-shaped  $\beta\text{-NaYF}_4\text{:Yb}^{3+}(18\%),\text{Er}^{3+}(2\%)$  crystallites (**UC $\mu\text{P}_{Berry}$** ) (from *Lorad Chemical Corp.*).<sup>102</sup>



### 5.2.1 Validation by comparison with measured results from Page et al.

In 1997, Page et al. reported on the absolute determination of UC conversion efficiencies for single emission bands for different green-, red- and blue-emitting UC phosphors.<sup>52</sup> Thereby, they provided a detailed description of the spectral calibration of their ISS and measurement procedure. For UCμP<sub>Page</sub> they determined the  $\Phi_{\text{UC,green}}(P)$  for a broad  $P$ -range of over three orders of magnitude.

Figure 5.7 a) displays the  $\Phi_{\text{UC,green}}(P)$  curves for UCμP<sub>BAM</sub> and UCμP<sub>Page</sub> for a  $P$ -range from 0.2 Wcm<sup>-2</sup> to 130 Wcm<sup>-2</sup>. The excellent agreement of these  $\Phi_{\text{UC,green}}(P)$  curves with similar increase and identical maximal  $\Phi_{\text{UC,green}}$  of 2.4% at  $P = 20$  Wcm<sup>-2</sup> implies comparability of these materials, i.e. crystal phase, crystal quality and Yb<sup>3+</sup> and the Er<sup>3+</sup> dopant concentrations. Both  $\Phi_{\text{UC,green}}(P)$  curves starts to decrease for  $P > 20$  Wcm<sup>-2</sup>, which may be attributed to a competition of triphotonic to biphotonic processes at high  $P$ . In this respect, thermal effects as reason for this decrease were excluded, see Publication I.

Figure 5.7 b) presents the normalized spectrally-corrected emission spectra of the Er<sup>3+</sup> green and Er<sup>3+</sup> red emission bands for UCμP<sub>BAM</sub> to UCμP<sub>Page</sub> at a  $P$  of ca. 20 Wcm<sup>-2</sup>. The good match of these normalized spectra further supports the assumption that these materials are comparable. Moreover, the domination of the Er<sup>3+</sup> red emission intensity, known for its triphotonic activation for μm-sized crystals,<sup>102</sup> strengthen the hypothesis of triphotonic processes being responsible for the fall of the  $\Phi_{\text{UC,green}}(P)$  at high  $P$ .

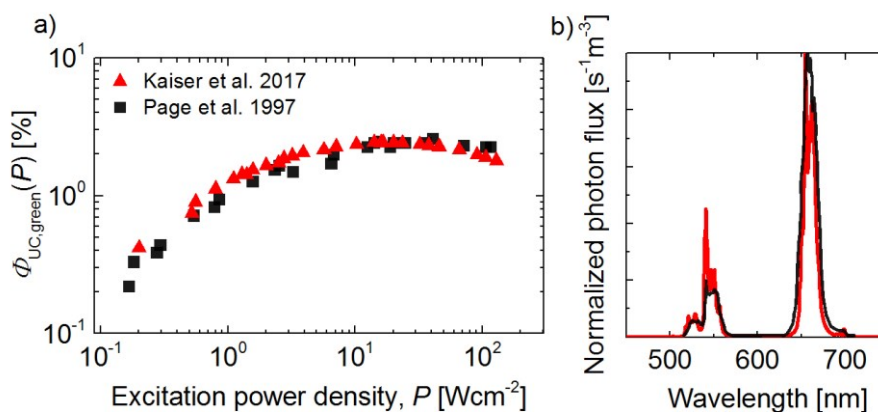


**Figure 5.7** Validation of absolutely measured  $\Phi_{\text{UC}}(P)$  of the Er<sup>3+</sup> green emission band ( $\Phi_{\text{UC,green}}(P)$ ) for UCμP<sub>BAM</sub> (red color) to UCμP<sub>Page</sub> (black color) from Page et al.<sup>52</sup>: a)  $\Phi_{\text{UC,green}}(P)$  curves for UCμP<sub>BAM</sub> and UCμP<sub>Page</sub> displayed from 0.2 Wcm<sup>-2</sup> to 130 Wcm<sup>-2</sup> b) Normalized spectrally-corrected emission spectra for UCμP<sub>BAM</sub> excited with  $P = 20$  Wcm<sup>-2</sup> and UCμP<sub>Page</sub> excited with a  $P$  in the Wcm<sup>-2</sup>-range. The data from Page was digitized and values were transformed from energy to photon numbers. Reprinted from Kaiser et al.<sup>40</sup> with permission from The Royal Society of Chemistry.

### 5.2.2 Validation by comparison with measured results from the Van Veggel group

The Van Veggel Group published in 2010, a strategy for the absolute measurement of the  $\Phi_{UC}$  for UCNPs using a commercially available spectrophotometer (FLS 920 from *Edinburgh Instruments*) combined with a 980 nm laser diode and an integrating sphere.<sup>51</sup> This work is an important milestone in the UCNPs research area as the performance of UCNPs was previously only compared relatively. In order to validate their  $\Phi_{UC}$  results, they compared the maximal  $\Phi_{UC,green}$  value of 3 % for UC $\mu$ P<sub>VanVeggel</sub> with the  $\Phi_{UC,green}$  value of 2.4% from UC $\mu$ P<sub>Page</sub>. This value also matches well with the  $\Phi_{UC,green}$  value of 2.4% measured for UC $\mu$ P<sub>BAM</sub>.

### 5.2.3 Validation by comparison with simulated results from the Berry group

In 2014, the Berry group simulated the spectral  $\Phi_{UC}(P)$ 's of the Er<sup>3+</sup> green ( $\Phi_{UC,green}(P)$ ), Er<sup>3+</sup> red ( $\Phi_{UC,red}(P)$ ) and Er<sup>3+</sup> purple ( $\Phi_{UC,purple}(P)$ ) emission bands.<sup>102</sup> These simulation results were based on a comprehensive rate equation analysis utilizing measured  $P$ -dependent intensity and UCL lifetime data of the Er<sup>3+</sup> purple, green and red emission bands. This analysis was based on a new rate equation model revisiting the back then outdated model of population processes for the different Er<sup>3+</sup> energy levels of  $\beta$ -NaYF<sub>4</sub>:Yb<sup>3+</sup>,Er<sup>3+</sup>.

Figure 5.6 a) - d) shows the  $\Phi_{UC,green}(P)$ ,  $\Phi_{UC,red}(P)$ ,  $\Phi_{UC,purple}(P)$ , and their sum ( $\Phi_{UC,vis}(P)$ ) for UC $\mu$ P<sub>BAM</sub> and UC $\mu$ P<sub>Berry</sub>. The  $\Phi_{UC,vis}(P)$  and  $\Phi_{UC,green}(P)$  curves have similar shape for both samples with relative deviation < 40%. Taking into account the complexity of the population processes for the multitude Er<sup>3+</sup> levels, these deviations between experimental and simulated data can be considered as relatively small. However, the  $\Phi_{UC,red}(P)$  and  $\Phi_{UC,purple}(P)$  show high deviations by factors of two and five, respectively. In particular for  $\Phi_{UC,purple}(P)$ , the shape also strongly differs between UC $\mu$ P<sub>Berry</sub> and UC $\mu$ P<sub>BAM</sub>. Moreover, the  $I_{green}/I_{red}$  ratio strongly deviates by a factor of ca. 3 between UC $\mu$ P<sub>Berry</sub> and UC $\mu$ P<sub>BAM</sub>. However, the  $I_{green}/I_{red}$  ratio determined for UC $\mu$ P<sub>BAM</sub> are supported by the values of UC $\mu$ P<sub>Page</sub>, see 5.2.1 *Validation by comparison with measured results from Page et al.*. Further, the comparability of UC $\mu$ P<sub>Berry</sub> and UC $\mu$ P<sub>BAM</sub> is underlined by similar luminescent decay kinetic of the different UC emission bands, see Figure 5.6 e).

### 5.2.3 Validation by comparison with experimental results from the Berry group

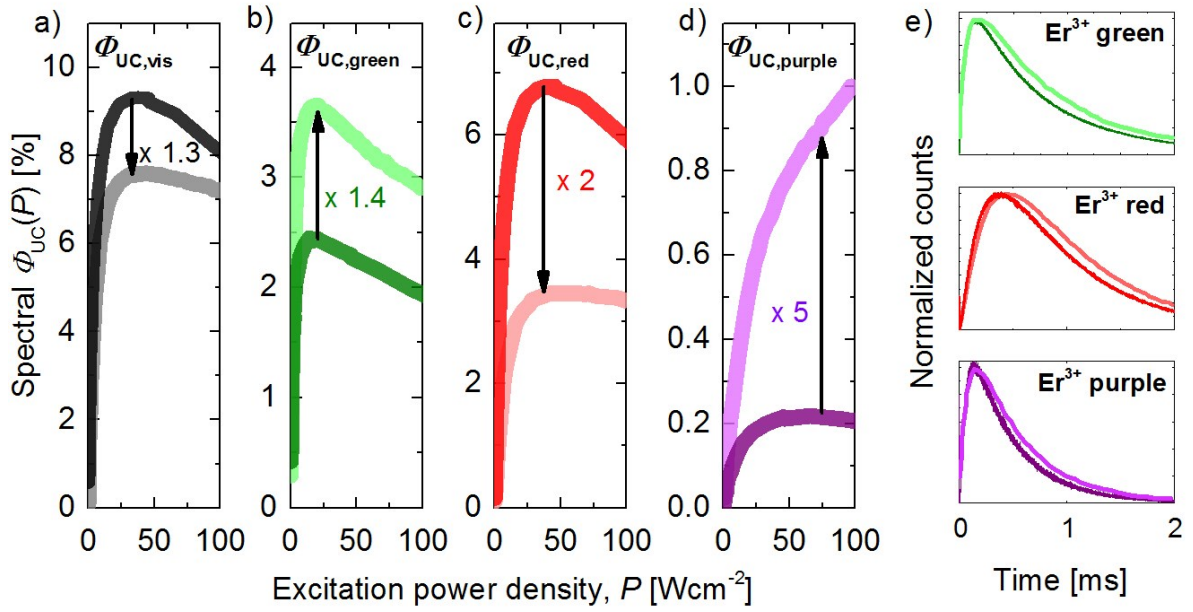


**Figure 5.6** Validation of  $\Phi_{UC}(P)$ 's of experimental results for UCμP<sub>BAM</sub> (dark colored lines) by the simulation results for UCμP<sub>Berry</sub> (light colored lines) from the Berry group:

a)-d)  $P$ -dependent spectral  $\Phi_{UC}$  of the Er<sup>3+</sup> green ( $\Phi_{UC,green}(P)$ ), red ( $\Phi_{UC,red}(P)$ ) and purple Er<sup>3+</sup> emission bands ( $\Phi_{UC,purple}(P)$ ), as well as the vis  $\Phi_{UC}(\Phi_{UC,vis}(P))$ , equaling the sum of  $\Phi_{UC,green}(P)$ ,  $\Phi_{UC,red}(P)$  and  $\Phi_{UC,purple}(P)$  for UCμP<sub>BAM</sub> and UCμP<sub>Berry</sub>; e) Comparison of lifetime curves for UCμP<sub>BAM</sub> ( $\lambda_{exc} = 940$  nm, pulse energy of *ca.* 1 mJcm<sup>-2</sup>) compared to UCμP<sub>Berry</sub> ( $\lambda_{exc} = 943$  nm, pulse energy of 66 mJcm<sup>-2</sup>) revealing similar (de-)population dynamics for UCμP<sub>BAM</sub> and UCμP<sub>Berry</sub>. Reproduced from Kaiser et al.<sup>40</sup> with permission from The Royal Society of Chemistry.

### 5.3. Conclusions of chapter 5

A guideline for  $P$ -dependent  $\Phi_{UC}$  measurement with the newly custom-built ISS has been developed. Special emphasis was given to the challenges and requirements on the optical properties of the sample and measurement geometry for accurate  $\Phi_{UC}(P)$  measurements. Overall, this underlines the need for careful consideration of these conditions to obtain  $P$ -dependent  $\Phi_{UC}$  values with high precision. In particular, the choice of the BP showed to be crucial factor for an accurate determination of the  $\Phi_{UC}(P)$  underlining the need for a homogenous Top Hat BP.

The obtained  $\Phi_{UC}(P)$  data for a commercial  $\mu\text{m}$ -sized  $\beta\text{-NaYF}_4\text{:Yb}^{3+},\text{Er}^{3+}$  ( $\text{UC}\mu\text{P}_{\text{BAM}}$ ) was validated with literature data from Page et al.<sup>52</sup>, the Van Veggel group<sup>51</sup>, and the Berry group<sup>103</sup>. The independently measured maximal  $\Phi_{UC,\text{green}}(P)$  of  $\text{UC}\mu\text{P}_{\text{BAM}}$  and  $\text{UC}\mu\text{P}_{\text{Page}}$  with 2.4% as well as  $\text{UC}\mu\text{P}_{\text{VanVeggel}}$  with 3% underlines the quality of spectral calibration and suitability of the measurement strategies of the newly-developed ISS. The theoretical results for  $\text{UC}\mu\text{P}_{\text{Berry}}$  of the  $\Phi_{UC,\text{vis}}(P)$  and  $\Phi_{UC,\text{green}}(P)$  showed deviations up to 40% compared to the measured values for  $\text{UC}\mu\text{P}_{\text{BAM}}$ . Taken into account the complexity of the UC processes these deviations can be considered as relatively small. However, the high deviations of  $\text{UC}\mu\text{P}_{\text{Berry}}$  and  $\text{UC}\mu\text{P}_{\text{BAM}}$  for the  $\Phi_{UC,\text{red}}(P)$  and  $\Phi_{UC,\text{purple}}(P)$  by factors two and five, respectively, suggest that a further optimization of their rate equation model for  $\beta\text{-NaYF}_4\text{:Yb}^{3+},\text{Er}^{3+}$   $\mu\text{m}$ -sized UC systems is needed.

These studies laid the ground for the following quantitative optical characterization of  $\beta\text{-NaYF}_4\text{:Yb}^{3+},\text{Er}^{3+}$  UCNPs in dependence of the solvent and dopant concentration.

---

## 6 Solvent-Dependent Optical Properties of $\beta$ -NaYF<sub>4</sub>:Yb<sup>3+</sup>,Er<sup>3+</sup> UCNPs

This chapter deals with the influence of particle microenvironment and thereby, also surface functionalization on the UCL and  $\Phi_{UC}$  of 23 nm-sized  $\beta$ -NaYF<sub>4</sub>:Yb<sup>3+</sup>(19%),Er<sup>3+</sup>(2%) UCNPs. In the first part, the impact of vibrational modes of different solvents on the  $\Phi_{UC}$  is discussed. In the second part, a special emphasis was dedicated to the study of the population mechanisms of the Yb<sup>3+</sup> and Er<sup>3+</sup> energy levels of UCNPs dispersed in water (H<sub>2</sub>O) and heavy water (D<sub>2</sub>O). In contrast to H<sub>2</sub>O, the vibrational modes of D<sub>2</sub>O are shifted to lower frequencies, and therefore, lead less likely to the depopulation of the Yb<sup>3+</sup> and Er<sup>3+</sup> energy levels. This resulted to a model of the (de-)population processes for the participating Er<sup>3+</sup> energy levels for UCNPs dispersed in H<sub>2</sub>O and UCNPs dispersed in solvents without UCL quenching OH-bonds.

### 6.1 Solvent-dependent upconversion quantum yield ( $\Phi_{UC}$ )

In this section, the influence of different solvents on the  $\Phi_{UC}(P)$  of identical UCNPs passivated with different surface passivating molecules was studied. Different surface chemistry, i.e. different ligands, were required to render the UCNPs dispersible in different solvents. The UCL and  $\Phi_{UC}(P)$ 's of the following four samples were recorded: i) oleate-capped UCNPs dispersed in cyclohexane, ii) BF<sub>4</sub><sup>-</sup>-capped UCNPs dispersed in DMF and iii) DSPE-capped UCNPs dispersed in H<sub>2</sub>O and iv) DSPE-capped UCNPs dispersed D<sub>2</sub>O (see 4.1 *Overview of the investigated  $\beta$ -NaYF<sub>4</sub>:Yb<sup>3+</sup>,Er<sup>3+</sup> samples*). The passivating surface molecules have two tasks: i) to control particle colloidal stability by electrostatic or steric effects to prevent agglomeration of the UCNPs and ii) to minimize the particle surface area accessible to the solvent molecules aiming to reduce solvent-induced UCL quenching. The complete suppression of solvent-induced UCL quenching requires a tight ligand shell preventing any penetration of solvent molecules, which was not completely achieved here.

Figure 6.1 a) presents the  $P$ -dependent  $\Phi_{UC}$  of the investigated UCNPs. The DSPE-capped UCNPs dispersed in D<sub>2</sub>O showed the best performance with a  $\Phi_{UC}$  of about 1.1% at  $P = 800 \text{ Wcm}^{-2}$ . In comparison, the UCNPs dispersed in DMF, cyclohexane and H<sub>2</sub>O perform with 90%, 75% and 40% of this  $\Phi_{UC}$  value at  $800 \text{ Wcm}^{-2}$ , respectively. Figure 6.1 b) displays the absorbance spectra of the solvents near the spectral region of the Yb<sup>3+</sup> 980 nm emission band ( $^2F_{5/2} \rightarrow ^2F_{7/2}$ ) This demonstrates a correlation for the reduction of the  $\Phi_{UC}$  by

the different solvents with the overlap of the absorbance spectra of the solvent and the Yb<sup>3+</sup> 980 nm emission band. This overlap provides a measure for the probability of the nonradiative deactivation of near-surface excited Yb<sup>3+</sup> ions *via* ET to the solvent molecules. The strong absorption of the vibrational overtone O-H-mode at 980 nm of H<sub>2</sub>O can be identified as the main factor for the diminishing of the  $\Phi_{UC}$  by a factor of 2.5 – 3 for the DSPE-capped UCNPs in H<sub>2</sub>O compared to the UCNPs in D<sub>2</sub>O. This is also in accordance with the reduction of the Yb<sup>3+</sup> 980 nm emission lifetime from 160  $\mu$ s to 40  $\mu$ s, see Publication II. The fact that Arppe et al. reported for 38 nm-sized bare UCNPs dispersed in H<sub>2</sub>O a UCL quenching of 99.9% of the Er<sup>3+</sup> green and red UCL compared to the same UCNPs dispersed in D<sub>2</sub>O underlines the partial repulsion of H<sub>2</sub>O molecules from the surface of the 23 nm-sized DSPE-capped UCNPs.

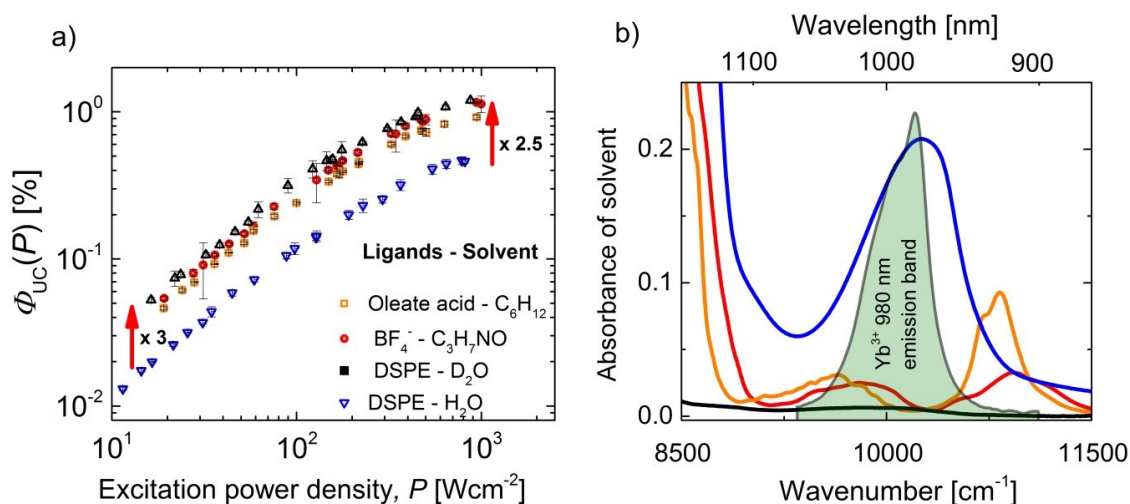


**Figure 6.1 Surface quenching of 23 nm-sized  $\beta$ -NaYF<sub>4</sub>:Yb<sup>3+</sup>(19%),Er<sup>3+</sup>(2%) UCNPs by solvent molecules.** a) Measured  $\Phi_{UC}(P)$  curves for UCNPs in different solvents: Oleate-capped UCNPs in cyclohexane (C<sub>6</sub>H<sub>12</sub>) (orange squares), BF<sub>4</sub>-capped UCNPs in DMF (red circles) as well as DSPE-capped UCNPs in heavy water (D<sub>2</sub>O) (black triangles) and water (H<sub>2</sub>O) (blue triangles); b) Absorbance spectra of the solvents - same color code as in a) - and the Yb<sup>3+</sup> 980 nm emission band (<sup>2</sup>F<sub>5/2</sub> → <sup>2</sup>F<sub>7/2</sub>); Reproduced from Würth, Kaiser et al.<sup>55</sup> with permission from The Royal Society of Chemistry.

## 6.2 Emission color of UCNPs dispersed in D<sub>2</sub>O and H<sub>2</sub>O

Subsequently, the differences in population processes at different  $P$  of the emissive Er<sup>3+</sup> energy levels of the DSPE-capped UCNPs dispersed in H<sub>2</sub>O and D<sub>2</sub>O were investigated. Figure 6.2 a) shows the normalized UCL spectra of these UCNPs for a low  $P$  value of 16 Wcm<sup>-2</sup> and a high  $P$  value of 1000 Wcm<sup>-2</sup>. The spectra display the wavelength region from 500 nm –

## 6.2 Emission color of UCNPs dispersed in D<sub>2</sub>O and H<sub>2</sub>O

900 nm including the Er<sup>3+</sup> green at 520/540 nm (<sup>2</sup>H<sub>11/2</sub>, <sup>4</sup>S<sub>3/2</sub> → <sup>4</sup>I<sub>15/2</sub>), Er<sup>3+</sup> red at 655 nm (<sup>4</sup>F<sub>9/2</sub> → <sup>4</sup>I<sub>15/2</sub>), Er<sup>3+</sup> 810 nm (<sup>4</sup>I<sub>9/2</sub> → <sup>4</sup>I<sub>15/2</sub>), and Er<sup>3+</sup> 850 nm (<sup>2</sup>H<sub>11/2</sub>, <sup>4</sup>S<sub>3/2</sub> → <sup>4</sup>I<sub>13/2</sub>) emission bands. At  $P = 16 \text{ Wcm}^{-2}$ , an enhanced relative intensity of the Er<sup>3+</sup> red and 810 nm emission bands can be observed for the UCNPs dispersed in H<sub>2</sub>O compared to D<sub>2</sub>O. Thereby, the relative intensities of the Er<sup>3+</sup> green and Er<sup>3+</sup> 850 nm emission bands, both originating from the <sup>4</sup>S<sub>3/2</sub>, <sup>2</sup>H<sub>11/2</sub> level are strongly reduced. This reveals that the population dynamics, at low  $P$ , differ strongly for UCNPs dispersed in H<sub>2</sub>O and D<sub>2</sub>O. Contrarily, at a high  $P$  of  $1000 \text{ Wcm}^{-2}$ , the normalized UCL spectra are nearly identical in both solvents. Thus, the population dynamics for the emissive Er<sup>3+</sup> energy levels are assumed to be comparable. These observations are supported by the  $P$ -dependent behavior of  $I_{\text{green}}/I_{\text{red}}$  ( $I_{\text{green}}/I_{\text{red}}(P)$ ), see Figure 6.2 b). For UCNPs in D<sub>2</sub>O,  $I_{\text{green}}/I_{\text{red}}(P)$  decreases for increasing  $P$  and converge to a constant value of about 0.4. In case of the UCNPs in H<sub>2</sub>O, the  $I_{\text{green}}/I_{\text{red}}(P)$  starts at a 5 times lower value, increases to a maximal value of about 0.7 and converges to the same  $I_{\text{green}}/I_{\text{red}}(P)$  value of about 0.4 as observed for the UCPNs in D<sub>2</sub>O. This difference of relative spectral intensities of the UCL emission bands originate from the strong vibrational modes of H<sub>2</sub>O located between  $3300 \text{ cm}^{-1}$  to  $3700 \text{ cm}^{-1}$  and their respective energy levels of Er<sup>3+</sup> involved in the population of the emissive states.<sup>159</sup> In the case of D<sub>2</sub>O, these vibrational modes are shifted to lower energies due to the higher mass of deuterium compared to the hydrogen atoms, and thus, are not resonant anymore with the energy gaps between the Er<sup>3+</sup> energy levels, see Figure 6.3.

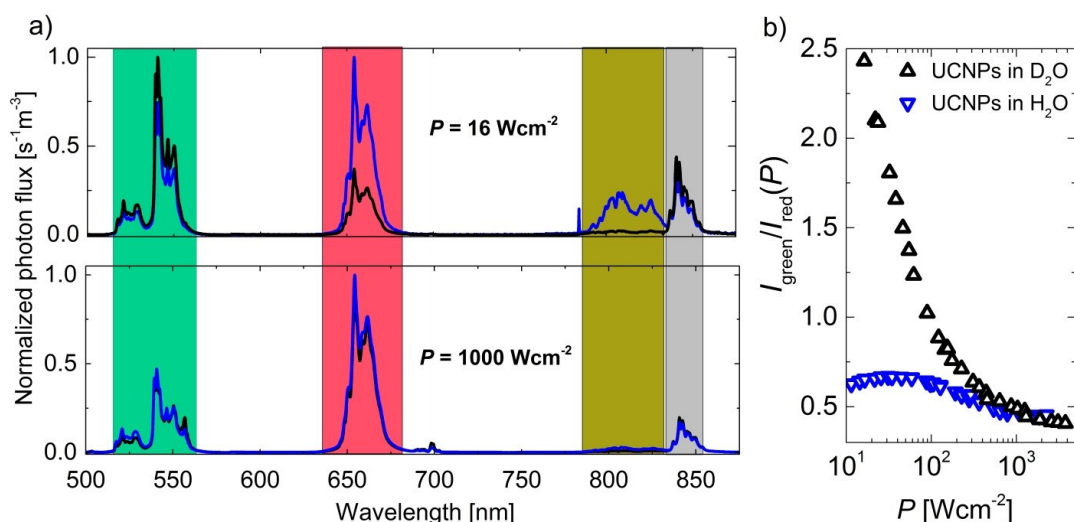


**Figure 6.2** a) Normalized emission spectra of 23 nm-sized  $\beta\text{-NaYF}_4\text{:Yb}^{3+}(19\%),\text{Er}^{3+}(2\%)$  UCNPs dispersed in D<sub>2</sub>O (black line) and H<sub>2</sub>O (blue line) for low  $P$  value of  $16 \text{ Wcm}^{-2}$  (top) and a high  $P$  of  $1000 \text{ Wcm}^{-2}$  (bottom); b)  $P$ -dependent  $I_{\text{green}}/I_{\text{red}}$  for UCNPs in D<sub>2</sub>O (black symbols) and H<sub>2</sub>O (blue symbols). Reproduced from Würth, Kaiser et al.<sup>55</sup> with permission from The Royal Society of Chemistry.

The energy scheme displayed in Figure 6.3 highlights the proposed dominant population pathways of the different UCL bands of the UCNPs in H<sub>2</sub>O. This model accounts for the efficient coupling of O-H vibrations to the Er<sup>3+</sup> <sup>4</sup>S<sub>3/2</sub>/<sup>2</sup>H<sub>11/2</sub> and <sup>4</sup>I<sub>11/2</sub> energy levels, enhancing nonradiative decay rates to the next lower energy level. At low  $P$ , the nonradiative decay of the Er<sup>3+</sup> 980 nm <sup>4</sup>I<sub>11/2</sub> energy level results in a high population of the Er<sup>3+</sup> 1520 nm <sup>4</sup>I<sub>13/2</sub> energy level for UCNPs dispersed in H<sub>2</sub>O. This favors the population from the Er<sup>3+</sup> <sup>4</sup>I<sub>13/2</sub> energy level to the Er<sup>3+</sup> red emissive <sup>4</sup>F<sub>9/2</sub> energy level *via* Yb<sup>3+</sup> to Er<sup>3+</sup> ET (<sup>4</sup>I<sub>13/2</sub> → <sup>4</sup>F<sub>9/2</sub>) at low  $P$ , which agrees with the observed increase of  $I_{\text{green}}/I_{\text{red}}(P)$  in the low  $P$ -region. Additionally, the high population of the Er<sup>3+</sup> <sup>4</sup>I<sub>13/2</sub> energy levels is also responsible for the high intensity of the 810 nm emission band induced by the Er<sup>3+</sup>-Er<sup>3+</sup> energy transfer process <sup>4</sup>I<sub>13/2</sub> + <sup>4</sup>I<sub>13/2</sub> → <sup>4</sup>I<sub>9/2</sub>.<sup>160</sup> In contrast, for the UCNPs dispersed in D<sub>2</sub>O and organic solvents, at low  $P$ , the Er<sup>3+</sup> red emissive <sup>4</sup>F<sub>9/2</sub> level is mainly populated *via* direct nonradiative relaxation from the Er<sup>3+</sup> green emissive <sup>4</sup>S<sub>3/2</sub>/<sup>2</sup>H<sub>11/2</sub> level, see Figure 2.6. At high  $P$ , UCNPs showed solvent-independent population of the Er<sup>3+</sup> red emissive <sup>4</sup>F<sub>9/2</sub> energy level, by a triphotonic process *via* the <sup>4</sup>G<sub>11/2</sub> energy level (see Figure 6.3, Right Panel), due to the compensation of solvent-induced quenching rates by the high  $P$ .

These conclusions of the (de-)population of UCNPs in H<sub>2</sub>O and D<sub>2</sub>O were underpinned with results from a rate equation analysis using the  $P$ -dependent emission spectra and luminescence lifetimes of Er<sup>3+</sup> 520/540 nm and 655 nm, as well as the Yb<sup>3+</sup> 980 nm emission bands, detailed in Publication II.



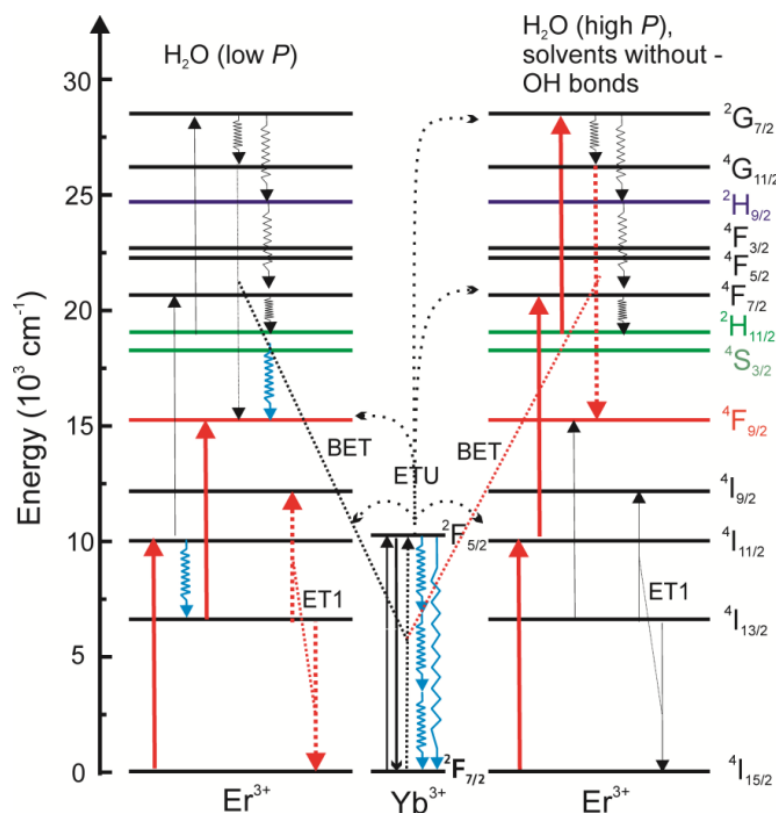


**Figure 6.3** Energy level diagram for Yb<sup>3+</sup>-Er<sup>3+</sup> interactions for UCNPs in H<sub>2</sub>O at low *P* (left) and high *P* (right); red arrows show dominant population pathways; for high *P* the dominant population pathways of UCNPs in H<sub>2</sub>O closely match with the photophysics of UCNPs in organic solvents and D<sub>2</sub>O; Blue arrows: indicate nonradiative deactivation by O–H vibrations of H<sub>2</sub>O. The arrow length represents the energy of the vibrational mode. ET: energy transfer, ETU: energy transfer upconversion, and BET: back energy transfer. Reprinted from Würth, Kaiser et al.<sup>55</sup> with permission from The Royal Society of Chemistry.

### 6.3 Conclusions of chapter 6

In summary, the influence of vibrational modes of solvent molecules on the  $\Phi_{UC}(P)$  and UCL was assessed for  $\beta$ -NaYF<sub>4</sub>:Yb<sup>3+</sup>,Er<sup>3+</sup> UCPNs with different surface modifications produced from the same UCPNs batch. The optical absorption of the solvent vibrational modes at 980 nm shows to be directly connected to nonradiative deactivation of near-surface excited Yb<sup>3+</sup> ions. In this respect, H<sub>2</sub>O with its highly absorptive vibrational modes, is acting as a strong luminescent quencher for the UCL, as also previously reported.<sup>42, 138</sup> The protection of the surface of DSPE-capped UCPNs from H<sub>2</sub>O molecules is underlined by a reduction of UCL by only about 60% in H<sub>2</sub>O compared to D<sub>2</sub>O. This is a strong improvement compared to the UCL intensity loss of 99.9% of bare UCPNs dispersed in H<sub>2</sub>O reported by Arppe et al. et al.<sup>42</sup>, which have a about five times higher particle volume compared to the here investigated UCPNs.

With the aid of UCL emission spectra and  $I_{green}/I_{red}(P)$  ratios, the (de-)population dynamics for the Er<sup>3+</sup> energy levels of UCPNs in H<sub>2</sub>O were identified. At low  $P$ , the fundamental vibrational modes of H<sub>2</sub>O from 3300-3700 cm<sup>-1</sup> lead to high population of the Er<sup>3+</sup> <sup>4</sup>I<sub>13/2</sub> energy level, favoring the population pathway from the <sup>4</sup>I<sub>13/2</sub> energy level to the red emissive <sup>4</sup>F<sub>9/2</sub> (655 nm) by an Yb<sup>3+</sup> energy transfer. However, at high  $P$ , the quenching rates are compensated resulting in identical (de-)population dynamics, and thus, identical emission color for UCPNs dispersed in H<sub>2</sub>O to D<sub>2</sub>O. Interpretations for the (de-)population dynamics in different solvents were supported by results of a rate equation analysis performed with a model from the Berry group<sup>102</sup>, which was detailed in Publication II. These methods for the refined understanding of the UC processes of UCPNs in H<sub>2</sub>O were a valuable starting point for the investigations of the change of UC mechanisms by the variation of the dopant concentrations, which is discussed in the next chapter.

---

## 7 Dopant Concentration-Dependent Optical Properties of $\beta$ -NaYF<sub>4</sub>:Yb<sup>3+</sup>,Er<sup>3+</sup> UCNPs

This chapter presents a study on the effect of varying the Yb<sup>3+</sup> and Er<sup>3+</sup> dopant concentrations on the emission colors of  $\beta$ -NaYF<sub>4</sub>:Yb<sup>3+</sup>,Er<sup>3+</sup> UCNPs with similar size. The *P*-dependent UCL data were measured with the ISS, and used as input data for a rate equation model containing all relevant Er<sup>3+</sup> levels to identify dopant concentration-dependent parameters. This combination of experimental data and theoretical analysis provided deep insights into the underlying UC mechanisms.

### 7.1 Dopant concentration-dependent upconversion luminescence (UCL)

In this section, the experimental results of the *P*-dependent Er<sup>3+</sup> green and red emission intensity as a function of the Yb<sup>3+</sup> and Er<sup>3+</sup> dopant concentration of  $\beta$ -NaYF<sub>4</sub>:Yb<sup>3+</sup>,Er<sup>3+</sup> UCNPs are discussed. The UCL was recorded over a wide *P*-range (> two orders of magnitude) for two dopant concentration series, namely the Yb<sup>3+</sup> and the Er<sup>3+</sup> series. The **Yb<sup>3+</sup> series** includes four samples with Yb<sup>3+</sup> sensitizer varied concentration from 11% - 21% and a constant Er<sup>3+</sup> concentration of 3%. The **Er<sup>3+</sup> series** consisted of four samples, with a Er<sup>3+</sup> activator concentration varied from 1% - 4% and a constant Yb<sup>3+</sup> concentration of 14%. The sample containing 14% Yb<sup>3+</sup> and 3% Er<sup>3+</sup> is part of both series. All UCNPs samples were similarly sized to about 33 nm, and were capped with oleic-acid molecules to provide dispersibility in toluene. This ensures that the observed effects are solely caused by the variation of dopant concentrations. A list including both concentration series is provided in Table 4.1.

Two different *P* values were chosen as corner points for the comparison of the UCL of the Yb<sup>3+</sup> and Er<sup>3+</sup> series. The first *P* value of  $P_{\text{unsat}} = 1.8 \text{ Wcm}^{-2}$  represents the unsaturated *P*-region for these UCNPs: The population of the Er<sup>3+</sup> activator ion energy levels induced by the Yb<sup>3+</sup> sensitizer ion *via* ET is low, and thus, the events of BET from Er<sup>3+</sup> to Yb<sup>3+</sup> is less pronounced. In this case, the biphotonic Er<sup>3+</sup> green emission intensity increases with  $P^2$ . For higher *P*, the increase of the Er<sup>3+</sup> green emission intensity levels off due to saturation. The second value  $P_{\text{sat}} = 380 \text{ Wcm}^{-2}$  marks the saturated *P*-region, where the intensity of the Er<sup>3+</sup> green emission band increases linearly with *P*. In this case, the Er<sup>3+</sup> energy levels are highly populated so that the contribution of BET from Er<sup>3+</sup> to Yb<sup>3+</sup> is relevant.

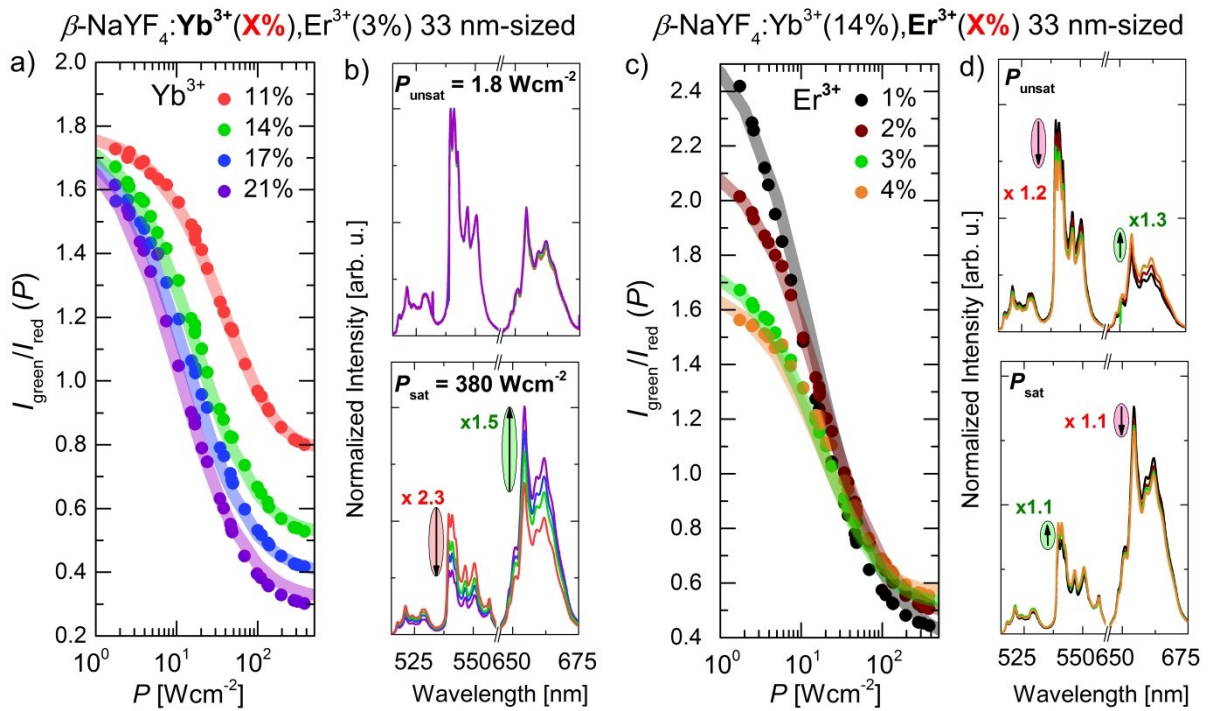
Figure 7.1 a) and c) presents the  $I_{\text{green}}/I_{\text{red}}(P)$  for the Yb<sup>3+</sup> and Er<sup>3+</sup> series. The  $I_{\text{green}}/I_{\text{red}}(P)$  converges to constant maximum and minimum values for decreasing and increasing  $P$ . Coincidentally, the  $I_{\text{green}}/I_{\text{red}}(P)$  ratios reach minimum and maximum values at  $P_{\text{sat}}$  and  $P_{\text{unsat}}$  for the investigated UCNPs. Analyzing the dopant concentration-dependent trend of the  $I_{\text{green}}/I_{\text{red}}(P)$  shows that with increasing Yb<sup>3+</sup> concentration, the maximum value at low  $P$  is unaffected, while the minimum value at high  $P$  decreases with increasing Yb<sup>3+</sup> concentration. Therefore the  $P$ -dependent color tuning range increases for increasing Yb<sup>3+</sup>, see Figure 7.1 a). In contrast, for increasing Er<sup>3+</sup> concentration the maximum value at low  $P$  decreases, while the minimum value at high  $P$  only shows a slight increase. Subsequently, the  $P$ -dependent color tuning range can be increased with decreasing Er<sup>3+</sup> concentration, see Figure 7.1 c).

Figure 7.1 b) and d) show the dopant concentration-dependent normalized UCL spectra at  $P_{\text{unsat}}$  and  $P_{\text{sat}}$  for the Yb<sup>3+</sup> and Er<sup>3+</sup> series. In order to highlight changes of the population of the respective energy levels, the intensity values of the UCL spectra were normalized to the overall UCL intensity ( $I_{\text{all}}(P)$ ) (integration interval from 370 nm to 900 nm). Subsequently, the  $P$ -dependent intensities of the UCL spectra are relative contributions  $I_{\text{rel}}(\lambda, P)$ . Further, the  $P$ -dependent relative intensities of the Er<sup>3+</sup> green and red emission bands are referred to as  $I_{\text{rel,green}}(P)$  and  $I_{\text{rel,red}}(P)$ , respectively. The UCL spectra of the Yb<sup>3+</sup> series at  $P_{\text{unsat}}$  are identical, underlining that the population dynamics of the respective Er<sup>3+</sup> energy levels are independent of Yb<sup>3+</sup> concentration for this low  $P$ , see Figure 7.1 b). This reveals very good comparability of crystallinity (low defect density), crystal size, surface chemistry, and spatial Er<sup>3+</sup> dopant ion distribution for this dopant concentration series, as  $I_{\text{rel,green}}(P)$  and  $I_{\text{rel,red}}(P)$  are known to be sensitive to these parameters by affecting the rate constants of the Er<sup>3+</sup> ions.<sup>40, 41, 55, 138, 161-163</sup> Contrary, at  $P_{\text{sat}}$ ,  $I_{\text{rel,red}}(P)$  increases by a factor of 1.5 and  $I_{\text{rel,green}}(P)$  drops by a factor of 2.3 for the Yb<sup>3+</sup> concentration varied from 11% to 21%. An increase of  $I_{\text{rel,red}}$  for increasing Yb<sup>3+</sup> concentration has been already reported in the literature, but the concrete mechanism was still under discussion.<sup>82, 104-106, 141-143</sup>

The rate equation analysis, more detailed in the following section, showed that this enhancement originates from an enhancement of the triphotonic population pathway to the red emissive Er<sup>3+</sup> <sup>4</sup>F<sub>9/2</sub> energy level fed by the triphotonic activated Er<sup>3+</sup> <sup>4</sup>G<sub>11/2</sub> energy level via a BET to Yb<sup>3+</sup>, see Figure 2.6.

## 7.1 Dopant concentration-dependent upconversion luminescence (UCL)

For the  $\text{Er}^{3+}$  series, at  $P_{\text{unsat}}$ ,  $I_{\text{rel,red}}(P)$  enhances and  $I_{\text{rel,green}}(P)$  decreases by factors of 1.3 and 1.2 for  $\text{Er}^{3+}$  concentration varied from 1% to 4%, see Figure 7.2 d). This can be ascribed to a higher number of surface or near-surface  $\text{Er}^{3+}$  ions, which enhance the probability of a nonradiative relaxation from the  $\text{Er}^{3+}$  green emissive level  $^2\text{H}_{11/2}, ^4\text{S}_{3/2}$  to the  $\text{Er}^{3+}$  red emissive level  $^4\text{F}_{9/2}$  (see Figure 2.6), which was found to be the main process for the activation of the  $\text{Er}^{3+}$  red emission band for these 33 nm-sized UCNPs dispersed in toluene at low  $P$ . Contrarily, at  $P_{\text{sat}}$ ,  $I_{\text{rel,red}}(P)$  decreases and  $I_{\text{rel,green}}(P)$  increases each by a factor of only 1.1 for increasing  $\text{Er}^{3+}$  concentration. These opposite trends for the  $\text{Er}^{3+}$  series at  $P_{\text{sat}}$  and  $P_{\text{unsat}}$  explain the ambiguous spectral trends reported in the literature and underline the need of considering a broad  $P$ -range.



**Figure 7.1** Dopant concentration and  $P$ -dependent spectral properties of 33 nm-sized oleate-capped  $\beta\text{-NaYF}_4\text{:Yb}^{3+},\text{Er}^{3+}$  UCNPs in toluene. a), b):  $\text{Yb}^{3+}$  series with a  $\text{Yb}^{3+}$  concentration varied between 11% to 21% at a constant  $\text{Er}^{3+}$  concentration of 3%; c), d):  $\text{Er}^{3+}$  series with a varied  $\text{Er}^{3+}$  concentration of 1% to 4% and a constant  $\text{Yb}^{3+}$  concentration of 14%; a), c)  $P$ -dependent measured (symbols) and simulated (lines)  $I_{\text{green}}/I_{\text{red}}$  values; b),d) UCL spectra from 515 nm to 675 nm for  $P_{\text{unsat}}$  of  $1.8 \text{ Wcm}^{-2}$  and  $P_{\text{sat}}$  of  $380 \text{ Wcm}^{-2}$ ; all spectra were normalized to the total UCL intensity integrated from 370 nm to 900 nm. Reprinted from Kaiser et al.<sup>164</sup> with permission from Tsinghua University Press.

## 7.2 Influence of the dopant concentrations on rate equation constants

To support the interpretation of the dopant concentration effects, a comprehensive rate equation analysis of the UCNPs samples of the investigated Yb<sup>3+</sup> and Er<sup>3+</sup> series was performed. The experimentally determined  $P$ -dependent intensity values and slope factors ( $n(P)$ ) of the Er<sup>3+</sup> red and green emission bands as well as the luminescence decay curves of the Er<sup>3+</sup> green, Er<sup>3+</sup> red, and Yb<sup>3+</sup> 980 nm emission bands were used as fitting parameters. The rate equation model, including all relevant Er<sup>3+</sup> energy levels and interactions, was adapted from the Berry group.<sup>102, 123</sup> Despite the success of this rate equation model from the Berry group in describing  $P$ -dependent UCL of UCNPs,<sup>123</sup> a couple of rate constants had to be changed drastically (by up to two orders of magnitude) for this work. To model the data of the Yb<sup>3+</sup> and Er<sup>3+</sup> series simplifications were made, e.g. the obtained rate constants were averaged over the complete particle volume. In contrast, Hossan et al. assumed an extra dark layer for such core-only particles without an inactive shell layer.<sup>123</sup> Comprehensive descriptions of the optimization of the rate constants, simplifications, and fitting procedures are provided in Publication III.

After optimizing the rate constants for the UCNPs sample containing 14% Yb<sup>3+</sup> and 3% Er<sup>3+</sup>, only three parameters for the Yb<sup>3+</sup> series and four parameters for the Er<sup>3+</sup> series had to be varied, including the respective density of dopant ions. The good match of the fitted data with the experimental data, including intensity and lifetime data of the Er<sup>3+</sup> green and Er<sup>3+</sup> red emission bands, see Figure 7.1 a) and c) and Publication III, supports the correct identification of the affected relevant parameters responsible for the dopant concentration-dependent color change of the UCNPs.

Figure 7.2 provides an overview of the rate constants affected by the variation of the Yb<sup>3+</sup> and Er<sup>3+</sup> concentration. For both series, an increase of the nonradiative Yb<sup>3+</sup> 980 nm rate constant ( $k_{Yb\_NR}$ ) with increasing dopant concentration was observed. Thereby,  $k_{Yb\_NR}$  was directly assessed from the measured decay behavior of the Yb<sup>3+</sup> 980 nm luminescence. The increase of  $k_{Yb\_NR}$  can be explained by a higher amount of near-surface Yb<sup>3+</sup> and Er<sup>3+</sup> ions that can be deactivated by oleic-acid ligand molecules (C-H vibrational modes between 2700 cm<sup>-1</sup> and 2950 cm<sup>-1</sup>)<sup>114</sup> or by the surrounding toluene solvent molecules (vibrational modes at 8000 cm<sup>-1</sup>)<sup>40</sup>.  $k_{Yb\_NR}$  was found to be more sensitive to changes of the Er<sup>3+</sup> concentration, since the energy gap to the next lower lying level for the Er<sup>3+</sup> 980 nm <sup>4</sup>I<sub>11/2</sub> is three times smaller compared to the Yb<sup>3+</sup> 980 nm <sup>4</sup>F<sub>5/2</sub> energy level. In addition, energy migration to the particle surface is enhanced for higher dopant concentrations due to the shorter ion-ion distances. The rate equation analysis showed that the change of  $k_{Yb\_NR}$  does only affect the

## 7.2 Influence of dopant concentration on rate equation constants

---

saturation behavior of the population of the  $\text{Er}^{3+}$  activator energy levels, but has no effect on the emission color of the UCNP. Although the increase of  $k_{\text{Yb\_NR}}$  also had a negative influence on the  $\Phi_{\text{UC}}$ , it was shown that the increase of absorbing  $\text{Yb}^{3+}$  concentration overcompensates this effect with respect to UC particle brightness, which is defined as product of the  $\Phi_{\text{UC}}$ , cross section [ $\text{cm}^2$ ] of an  $\text{Yb}^{3+}$  ion in a  $\text{NaYF}_4$  matrix, and the number of absorbing  $\text{Yb}^{3+}$  ion inside the UCNP, see Publication III.

For the  $\text{Yb}^{3+}$  series, all ET and BET rates were found to be enhanced simultaneously by 220% for a  $\text{Yb}^{3+}$  concentration from 11% to 21%, equaling a decrease of the average  $\text{Yb}^{3+}$ - $\text{Yb}^{3+}$  and  $\text{Yb}^{3+}$ - $\text{Er}^{3+}$  distances by *ca.* 20% from 0.9 nm to 0.7 nm. The trend of the ion distance-dependent ET and BET rates shows rather an exponential behavior, which may indicate that the energy transfer between  $\text{Yb}^{3+}$  and  $\text{Er}^{3+}$  originates from electron hopping (Dexter ET), see 2.2 *Energy transfer processes between  $\text{Ln}^{3+}$* . This underlines the possibility to investigate the physical nature of nonradiative ET for  $\text{Yb}^{3+}$ , $\text{Er}^{3+}$ -based UC systems with a rate equation analysis. Moreover, the rate equation analysis revealed that for increasing  $\text{Yb}^{3+}$  concentration, a pronounced BET from triphotonicly activated  $^4\text{G}_{7/2}$  to the red emissive  $^4\text{F}_{9/2}$  is responsible for the increase of the  $\text{Er}^{3+}$  red emission intensity at  $P_{\text{sat}}$ , see Figure 7.1 b). In the case of the  $\text{Er}^{3+}$  series, ET and BET are not affected. This is in accordance with a self-developed Monte Carlo simulation showing that for these relatively small  $\text{Er}^{3+}$  concentrations the average distance of  $\text{Er}^{3+}$  ions to the nearest  $\text{Yb}^{3+}$  ion changes only minimally (see Supporting Information of Publication III).

The observed color change for increasing  $\text{Er}^{3+}$  concentration results mainly from two processes. As discussed previously, at low  $P$ , the enhanced nonradiative rate from the  $^2\text{H}_{11/2}$ ,  $^4\text{S}_{3/2}$  to the red emissive  $^4\text{F}_{9/2}$  energy level ( $k_{\text{NR6}}$ ) by higher surface coupling results in an enhancement of the  $\text{Er}^{3+}$  red emission intensity, see middle Panel of Figure 7.3 b). At high  $P$ , the decrease of  $I_{\text{rel,red}}(P)$  is assigned to a yet unknown  $\text{Er}^{3+}$ - $\text{Er}^{3+}$  ET leading to a depopulation of the  $\text{Er}^{3+}$  red emissive  $^4\text{F}_{9/2}$  energy level. This was simulated with a simplified approach by using an additional factor for the  $\text{Yb}^{3+}$ - $\text{Er}^{3+}$  ET rate  $k_{\text{ET5-8}}$ , which also depopulates the  $\text{Er}^{3+}$   $^4\text{F}_{9/2}$  energy level. Therefore, the trend for the simulated change of  $\text{Er}^{3+}$ - $\text{Er}^{3+}$  ET, see Figure 2.7 b) lower Panel, may not correspond to the real change of the  $\text{Er}^{3+}$ - $\text{Er}^{3+}$  ET rate. In order to further optimize the rate equation system, four new possible candidates for the missing  $\text{Er}^{3+}$ - $\text{Er}^{3+}$  ET rate constant have been suggested, which were detailed and discussed in Publication III.

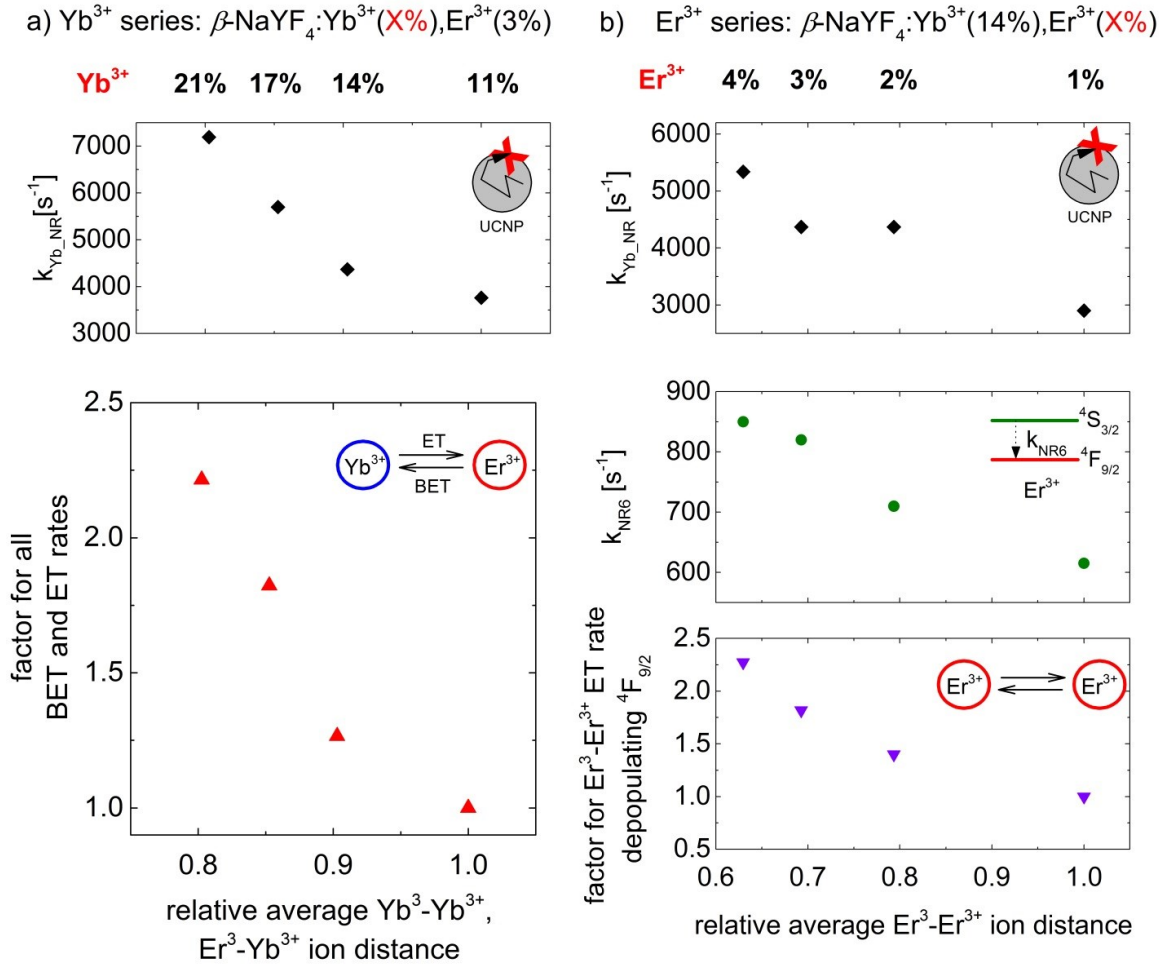


**Figure 7.2 Dependence of the rate constants on the dopant concentration for varied parameters of the rate equation analysis:** a) Yb<sup>3+</sup> series and b) Er<sup>3+</sup> series; In the case of the variation of the Yb<sup>3+</sup> concentration, the nonradiative rate of the Yb<sup>3+</sup> 980 nm <sup>2</sup>F<sub>5/2</sub> energy level and the ET and BET rates are influenced. For the Er<sup>3+</sup> concentration, the nonradiative rate of the Yb<sup>3+</sup> 980 nm <sup>2</sup>F<sub>5/2</sub> energy level, the nonradiative relaxation from the <sup>2</sup>H<sub>11/2</sub>, <sup>4</sup>S<sub>3/2</sub> to the red emissive level <sup>4</sup>F<sub>9/2</sub>, and a not yet identified Er<sup>3+</sup>-Er<sup>3+</sup> ET rate is influenced. For the Er<sup>3+</sup>-Er<sup>3+</sup> ET a simplified approach was used by varying an Yb<sup>3+</sup>-Er<sup>3+</sup> ET depopulating the <sup>4</sup>F<sub>9/2</sub> energy level to simulate the enhancement of the red emission band. In Publication III, four possible candidates for the missing Er<sup>3+</sup>-Er<sup>3+</sup> were discussed. Reproduced from Kaiser et al.<sup>164</sup> with permission from Tsinghua University Press.



### 7.3 Conclusions of chapter 7

In summary, the tuning of the UCL color of 33 nm-sized  $\beta$ -NaYF<sub>4</sub>:Yb<sup>3+</sup>,Er<sup>3+</sup> UCNPs by the variation of the Yb<sup>3+</sup> and Er<sup>3+</sup> dopant concentrations was studied for a  $P$ -range of over two orders of magnitude. Combining experimental results and theoretical investigations with a nine-level rate equation model from the Berry group, including the most significant energy levels of Er<sup>3+</sup>,<sup>102, 123</sup> allowed to make reliable statements about the influence of the dopant concentrations on interactions between the ions and the particle surface.

The variation of the Yb<sup>3+</sup> concentration from 11% to 21%, equaling a reduction in Er<sup>3+</sup>-Yb<sup>3+</sup> distance of 20%, resulted in an increase of 220 % for all Yb<sup>3+</sup> to Er<sup>3+</sup> ET rates and Er<sup>3+</sup> to Yb<sup>3+</sup> BET rates. This indirect measure of the change of ET processes opens the possibility to study the physical nature of nonradiative ET processes. The corresponding increase of the relative intensity of the Er<sup>3+</sup> red emission band ( $I_{\text{rel,red}}(P)$ ) at high  $P$  was attributed to an enhanced triphotonic activation of the red emissive Er<sup>3+</sup> <sup>4</sup>F<sub>9/2</sub> energy level the Er<sup>3+</sup> <sup>4</sup>G<sub>11/2</sub> to the red emissive <sup>4</sup>F<sub>9/2</sub> energy level.

For the Er<sup>3+</sup> series, different trends for  $I_{\text{rel,red}}(P)$  at low  $P$  and high  $P$  were determined. At low  $P$ , the increase of the number of Er<sup>3+</sup> ions leads to an enhanced biphotonic activation of the Er<sup>3+</sup> red emission band *via* direct relaxation from the green emissive <sup>2</sup>H<sub>11/2</sub>, <sup>4</sup>S<sub>3/2</sub> to <sup>4</sup>F<sub>9/2</sub> energy levels, induced by an increased surface coupling of the Er<sup>3+</sup> ions. At high  $P$ , a not yet identified Er<sup>3+</sup>-Er<sup>3+</sup> rate was found to be responsible for the decrease of  $I_{\text{rel,red}}(P)$ . Moreover, these results reveal that the modulation range of the emission color by  $P$  can be extended by increasing the Yb<sup>3+</sup> and/or decreasing the Er<sup>3+</sup> concentration. Overall, this highlights the possibility of predicting the emission color for  $\beta$ -NaYF<sub>4</sub>:Yb<sup>3+</sup>,Er<sup>3+</sup> UCNPs by rate equation modelling.

---

## 8 General Conclusions for Publications

In summary, an ISS has been designed, validated and utilized for the accurate absolute determination of  $P$ -dependent  $\Phi_{UC}$  and UCL spectra for different  $\beta$ -NaYF<sub>4</sub>:Yb<sup>3+</sup>,Er<sup>3+</sup> UC systems. The obtained  $\Phi_{UC}(P)$  and UCL results for  $\beta$ -NaYF<sub>4</sub>:Yb<sup>3+</sup>, Er<sup>3+</sup> UCNPs in different solvents and with varied Yb<sup>3+</sup> and Er<sup>3+</sup> dopant concentrations, in combination with theoretical modelling, allowed substantial extensions of the understanding of surface quenching and color tuning.

Publication I summarized the challenges and requirements of the custom-built ISS for  $\Phi_{UC}(P)$  measurements for 976 nm-excitable UC materials. This includes prerequisites on setup components and new calibration strategies. Moreover, measurement conditions for powders and dispersed UC samples were derived with respect to measurement geometry, experimental procedures, and optical properties of the UC material. This report can be used as a protocol to perform  $\Phi_{UC}(P)$  measurements with minimum uncertainty in the order of about 10 %. The maximum  $\Phi_{UC}$  of 10.5% at  $P = 30 \text{ Wcm}^{-2}$  for a commercial  $\beta$ -NaYF<sub>4</sub>:Yb<sup>3+</sup>(21%),Er<sup>3+</sup>(2%) 3  $\mu\text{m}$ -sized UC particles (UC $\mu$ P) is nowadays being frequently referenced as highest value for Yb<sup>3+</sup>,Er<sup>3+</sup>-based systems, underlining the overall accepted accuracy of this new ISS.

In Publication II, identical UCNPs dispersed in organic solvents, water (H<sub>2</sub>O) and heavy water (D<sub>2</sub>O) functionalized with different surface ligands were systematically studied. Thereby the  $\Phi_{UC}$  was found to be mainly determined by the interaction of near-surface Yb<sup>3+</sup> ions with the vibrational modes of the solvent and ligand molecules. In this respect, H<sub>2</sub>O leads to the highest quenching rate from the UCNPs surface due to its high frequency O-H vibrational modes resonant to the Yb<sup>3+</sup> 980 nm energy level. For organic solvents and D<sub>2</sub>O, the probability of energy transfer is less likely, since their C-H and O-D vibrational modes are non-resonant to the Yb<sup>3+</sup> 980 nm energy level as their frequencies are much lower. Instead, the lower-frequency vibrational modes of these solvents in combination with the low frequency vibrational modes of ligand molecules at *ca.* 3000 cm<sup>-1</sup> clearly affected the emission color of the UCNPs. Thereby, these vibrational modes can effectively bridge the energy gaps between the multitudes of Er<sup>3+</sup> energy levels ranging from 1000 cm<sup>-1</sup> to 3500 cm<sup>-1</sup>. Furthermore, the absolute UCL measurements, in combination with a rate equation analysis, enabled the development of a new (de-)population model explaining the change in emission color of UCNPs in H<sub>2</sub>O.

## 8 General Conclusions for Publications

---

In Publication III, the influence of the dopant concentration on emission color and particle brightness for a set of 33 nm-sized oleate-capped UCNPs dispersed in toluene was assessed for Yb<sup>3+</sup> and Er<sup>3+</sup> dopant concentrations varied from 11 - 21% and 1 - 4%, respectively. The experimental results, including emission intensities and slope factors of the Er<sup>3+</sup> green and red emission bands as well as luminescence lifetimes, were used for the optimization of the rate constants of a rate equation model considering all significant Er<sup>3+</sup> energy levels. As a result an increase of the Yb<sup>3+</sup> concentration was found to lead to enhanced triphotonic activation and an increase in Er<sup>3+</sup> concentration to an enhanced biphotonic activation of the red emissive <sup>4</sup>F<sub>9/2</sub> energy level. Moreover, the results indicate that the particle brightness of these UCNPs can be further improved with higher Yb<sup>3+</sup> and lower Er<sup>3+</sup> concentrations. This enabled an estimate of trends for the ultimate goal to find optimized dopant concentrations for maximal particle brightness in dependence of UCNPs size and particle architecture. Overall, a refined understanding of UC processes of  $\beta$ -NaYF<sub>4</sub>:Yb<sup>3+</sup>,Er<sup>3+</sup> UCNPs was gained by using quantitative measurements with the new custom-built ISS in combination with a comprehensive rate equation analysis.

---

---

---

# Appendix

## List of Abbreviations

<b>BET</b>	back energy transfer
<b>BP</b>	beam profile
<b>CCD</b>	charge-coupled device
<b>CET</b>	cooperative energy transfer
<b>CR</b>	cross-relaxation
<b>DMF</b>	N,N-dimethylformamide, solvent for UCNPs
<b>DS</b>	downshifted
<b>DSPE</b>	1,2-distearoyl-sn-glycero-3-phospho-ethanolamine-N-[methoxy-(poly-ethylene glycol)-2000] (ammonium salt)
$E_{em}$	energy of emitted photons
$E_{abs}$	energy of absorbed photons
$Er^{3+}$	trivalent erbium ions
<b>ESA</b>	excited state absorption
<b>ET</b>	energy transfer
<b>ETU</b>	energy transfer upconversion
<b>FWHM</b>	full width at half maximum
<b>Gauss<sub>exp</sub></b>	experimentally realized Gaussian beam profile
$Ho^{3+}$	trivalent holmium ions
$I_{sample}(\lambda, P)$	$P$ -dependent spectrally-corrected sample spectrum
$I_{blank}(\lambda, P)$	$P$ -dependent spectrally-corrected blank spectrum
$I(\lambda, P)$	$P$ -dependent spectral photon flux
$I_{\Delta\lambda}(P)$	$I(\lambda, P)$ for certain UC emission band or color
$I_{\lambda all}(P)$	$I(\lambda, P)$ including all UC emission bands
$I_{rel}(\lambda, P)$	$I(\lambda, P)$ relative to $I_{\lambda all}(P)$
$I_{rel, \Delta\lambda}(P)$	$I(\lambda, P)$ for certain UC emission band or color relative to $I_{\lambda all}(P)$
$I_{green}/I_{red}(P)$	green-to-red intensity ratio
<b>ISS</b>	integrating sphere setup
$Ln^{3+}$	trivalent lanthanide ions
$Nd^{3+}$	trivalent neodymium ions
<b>NIR</b>	near-infrared spectral region

---

## Appendix

---

$n(P)$	P-dependent slope factor
$N_{\text{em}}$	number of emitted photons
$N_{\text{abs}}$	number of absorbed photons
OA	Oleic acid, ligand molecules for UCNPs
$P$	excitation power density
$P_{\text{balance}}$	balancing excitation power density
$P_{\text{BP}}$	excitation power for certain beam profile
PL	photoluminescence
$\text{Re}^{3+}$	trivalent rare earth ions
Si-CCD	silicon-based charged-coupled-device
SHG	second harmonic generation
TEM	transmission electron microscopy
$\text{TH}_{\text{exp}}$	experimentally realized Top Hat beam profile
$\text{TH}_{\text{ideal}}$	ideal Top Hat beam profile
$\text{Tm}^{3+}$	trivalent thulium ions
TPA	two-photon absorption
TTA	triplet-triplet annihilation
UC	upconversion
UCL	upconversion luminescence
UCNPs	upconversion nm-sized particles
$\text{UC}\mu\text{P}$	upconversion $\mu\text{m}$ -sized particles
UV	ultraviolet spectral region
vis	visible spectral region
$\text{Yb}^{3+}$	trivalent ytterbium ion
$\alpha\text{-NaYF}_4$	sodium yttrium tetrafluoride in the cubic crystal phase
$\beta\text{-NaYF}_4$	sodium yttrium tetrafluoride in the hexagonal crystal phase
$\Phi$	photoluminescence quantum yield
$\Phi_{\text{UC}}$	upconversion photoluminescence quantum yield
$\Phi_{\text{UC}}(P)$	$P$ -dependent $\Phi_{\text{UC}}$
$\Phi_{\text{UC,sat}}$	saturated $\Phi_{\text{UC}}$
$\Phi_{\text{UC,max}}$	maximum $\Phi_{\text{UC}}$
$\Phi_{\text{UC,green}}(P)$	$P$ -dependent $\Phi_{\text{UC}}$ of $\text{Er}^{3+}$ green emission band
$\Phi_{\text{UC,red}}(P)$	$P$ -dependent $\Phi_{\text{UC}}$ of $\text{Er}^{3+}$ red emission band
$\Phi_{\text{UC,purple}}(P)$	$P$ -dependent $\Phi_{\text{UC}}$ of $\text{Er}^{3+}$ purple emission band
$\Phi_{\text{UC,vis}}(P)$	$P$ -dependent $\Phi_{\text{UC}}$ for visible spectral region

---

**Bibliography**

1. Joshi, B. P.; Wang, T. D., Targeted Optical Imaging Agents in Cancer: Focus on Clinical Applications. *Contrast Media Mol Imaging* **2018**, *2018*, 2015237-2015237.
2. Wilhelm, S.; Tavares, A. J.; Dai, Q.; Ohta, S.; Audet, J.; Dvorak, H. F.; Chan, W. C. W., Analysis of nanoparticle delivery to tumours. *Nature Reviews Materials* **2016**, *1*, 16014.
3. Dang, X.; Bardhan, N. M.; Qi, J.; Gu, L.; Eze, N. A.; Lin, C.-W.; Kataria, S.; Hammond, P. T.; Belcher, A. M., Deep-tissue optical imaging of near cellular-sized features. *Scientific Reports* **2019**, *9* (1), 3873.
4. Gerwing, M.; Herrmann, K.; Helfen, A.; Schliemann, C.; Berdel, W. E.; Eisenblätter, M.; Wildgruber, M., The beginning of the end for conventional RECIST — novel therapies require novel imaging approaches. *Nature Reviews Clinical Oncology* **2019**, *16* (7), 442-458.
5. Resch-Genger, U.; Grabolle, M.; Cavaliere-Jaricot, S.; Nitschke, R.; Nann, T., Quantum dots versus organic dyes as fluorescent labels. *Nature Methods* **2008**, *5* (9), 763-775.
6. Medintz, I. L.; Uyeda, H. T.; Goldman, E. R.; Mattoussi, H., Quantum dot bioconjugates for imaging, labelling and sensing. *Nature Materials* **2005**, *4* (6), 435-446.
7. Petryayeva, E.; Algar, W. R.; Medintz, I. L., Quantum Dots in Bioanalysis: A Review of Applications across Various Platforms for Fluorescence Spectroscopy and Imaging. *Applied Spectroscopy* **2013**, *67* (3), 215-252.
8. Mason, W. T., *Fluorescent and luminescent probes for biological activity : a practical guide to technology for quantitative real-time analysis*. 2nd ed. ed.; San Diego (Calif.) : Academic press: 1999.
9. Ekimov, A.; Onushcheko, A., Quantum Size Effect in Three-Dimensional Microscopic Semiconductor Crystals. *ZhETF Pis ma Redaktsiiu* **1981**, *34*, 363.
10. Yoffe, A. D., Low-dimensional systems: Quantum size effects and electronic properties of semiconductor microcrystallites (zero-dimensional systems) and some quasi-two-dimensional systems. *Advances in Physics* **2002**, *51* (2), 799-890.
11. Würth, C.; Geißler, D.; Behnke, T.; Kaiser, M.; Resch-Genger, U., Critical review of the determination of photoluminescence quantum yields of luminescent reporters. *Analytical and Bioanalytical Chemistry* **2014**, 1-20.
12. Hatami, S.; Würth, C.; Kaiser, M.; Leubner, S.; Gabriel, S.; Bahrig, L.; Lesnyak, V.; Pauli, J.; Gaponik, N.; Eychemüller, A.; Resch-Genger, U., Absolute photoluminescence quantum yields of IR26 and IR-emissive Cd<sub>1-x</sub>Hg<sub>x</sub>Te and PbS quantum dots - method- and material-inherent challenges. *Nanoscale* **2015**, *7* (1), 133-143.
13. Hardman, R., A toxicologic review of quantum dots: toxicity depends on physicochemical and environmental factors. *Environ Health Perspect* **2006**, *114* (2), 165-172.
14. Nikazar, S.; Sivasankarapillai, V. S.; Rahdar, A.; Gasmi, S.; Anumol, P. S.; Shanavas, M. S., Revisiting the cytotoxicity of quantum dots: an in-depth overview. *Biophys Rev* **2020**, *12* (3), 703-718.
15. Mader, H. S.; Kele, P.; Saleh, S. M.; Wolfbeis, O. S., Upconverting luminescent nanoparticles for use in bioconjugation and bioimaging. *Current Opinion in Chemical Biology* **2010**, *14* (5), 582-596.
16. Chen, G. Y.; Agren, H.; Ohulchanskyy, T. Y.; Prasad, P. N., Light upconverting core-shell nanostructures: nanophotonic control for emerging applications. *Chemical Society Reviews* **2015**, *44* (6), 1680-1713.
17. Resch-Genger, U.; Gorris, H. H., Perspectives and challenges of photon-upconversion nanoparticles - Part I: routes to brighter particles and quantitative spectroscopic studies. *Analytical and Bioanalytical Chemistry* **2017**, *409* (25), 5855-5874.
18. Jaque, D.; Vetrone, F., Luminescence nanothermometry. *Nanoscale* **2012**, *4* (15), 4301-4326.
19. Zhou, B.; Shi, B. Y.; Jin, D. Y.; Liu, X. G., Controlling upconversion nanocrystals for emerging applications. *Nature Nanotechnology* **2015**, *10* (11), 924-936.

20. Chan, E. M., Combinatorial approaches for developing upconverting nanomaterials: high-throughput screening, modeling, and applications. *Chemical Society Reviews* **2015**, *44* (6), 1653-1679.
21. Haase, M.; Schafer, H., Upconverting Nanoparticles. *Angewandte Chemie-International Edition* **2011**, *50* (26), 5808-5829.
22. Wu, X.; Chen, G. Y.; Shen, J.; Li, Z. J.; Zhang, Y. W.; Han, G., Upconversion Nanoparticles: A Versatile Solution to Multiscale Biological Imaging. *Bioconjugate Chemistry* **2015**, *26* (2), 166-175.
23. Xu, C. T.; Zhan, Q. Q.; Liu, H. C.; Somesfalean, G.; Qian, J.; He, S. L.; Andersson-Engels, S., Upconverting nanoparticles for pre-clinical diffuse optical imaging, microscopy and sensing: Current trends and future challenges. *Laser & Photonics Reviews* **2013**, *7* (5), 663-697.
24. Wang, H. Q.; Batentschuk, M.; Osvet, A.; Pinna, L.; Brabec, C. J., Rare-Earth Ion Doped Up-Conversion Materials for Photovoltaic Applications. *Advanced Materials* **2011**, *23* (22-23), 2675-2680.
25. Gnach, A.; Bednarkiewicz, A., Lanthanide-doped up-converting nanoparticles: Merits and challenges. *Nano Today* **2012**, *7* (6), 532-563.
26. Wang, F.; Liu, X. G., Recent advances in the chemistry of lanthanide-doped upconversion nanocrystals. *Chemical Society Reviews* **2009**, *38* (4), 976-989.
27. Gorris, H. H.; Wolfbeis, O. S., Photon-Upconverting Nanoparticles for Optical Encoding and Multiplexing of Cells, Biomolecules, and Microspheres. *Angewandte Chemie-International Edition* **2013**, *52* (13), 3584-3600.
28. Zheng, W.; Huang, P.; Tu, D.; Ma, E.; Zhu, H.; Chen, X., Lanthanide-doped upconversion nano-bioprobes: electronic structures, optical properties, and biodetection. *Chem Soc Rev* **2015**, *44* (6), 1379-415.
29. Zhou, J.; Liu, Q.; Feng, W.; Sun, Y.; Li, F., Upconversion Luminescent Materials: Advances and Applications. *Chemical Reviews* **2015**, *115* (1), 395-465.
30. Auzel, F., Upconversion and anti-stokes processes with f and d ions in solids. *Chemical Reviews* **2004**, *104* (1), 139-173.
31. Han, S.; Deng, R.; Xie, X.; Liu, X., Enhancing Luminescence in Lanthanide-Doped Upconversion Nanoparticles. *Angewandte Chemie International Edition* **2014**, *53* (44), 11702-11715.
32. Peng, X.; Huang, B.; Pu, R.; Liu, H.; Zhang, T.; Widengren, J.; Zhan, Q.; Ågren, H., Fast upconversion super-resolution microscopy with 10  $\mu$ s per pixel dwell times. *Nanoscale* **2019**, *11* (4), 1563-1569.
33. Chen, C.; Wang, F.; Wen, S.; Su, Q. P.; Wu, M. C. L.; Liu, Y.; Wang, B.; Li, D.; Shan, X.; Kianinia, M.; Aharonovich, I.; Toth, M.; Jackson, S. P.; Xi, P.; Jin, D., Multi-photon near-infrared emission saturation nanoscopy using upconversion nanoparticles. *Nature Communications* **2018**, *9* (1), 3290.
34. Chen, S.; Weitemier, A. Z.; Zeng, X.; He, L.; Wang, X.; Tao, Y.; Huang, A. J. Y.; Hashimoto, Y.; Kano, M.; Iwasaki, H.; Parajuli, L. K.; Okabe, S.; Teh, D. B. L.; All, A. H.; Tsutsui-Kimura, I.; Tanaka, K. F.; Liu, X.; McHugh, T. J., Near-infrared deep brain stimulation via upconversion nanoparticle-mediated optogenetics. *Science (New York, N.Y.)* **2018**, *359* (6376), 679-684.
35. Fernandez-Bravo, A.; Wang, D.; Barnard, E. S.; Teitelboim, A.; Tajon, C.; Guan, J.; Schatz, G. C.; Cohen, B. E.; Chan, E. M.; Schuck, P. J.; Odom, T. W., Ultralow-threshold, continuous-wave upconverting lasing from subwavelength plasmons. *Nature Materials* **2019**, *18* (11), 1172-1176.
36. Wang, F.; Wen, S.; He, H.; Wang, B.; Zhou, Z.; Shimon, O.; Jin, D., Microscopic inspection and tracking of single upconversion nanoparticles in living cells. *Light: Science & Applications* **2018**, *7*.
37. Zhou, M.; Ge, X.; Ke, D.-M.; Tang, H.; Zhang, J.-Z.; Calvaresi, M.; Gao, B.; Sun, L.; Su, Q.; Wang, H., The Bioavailability, Biodistribution, and Toxic Effects of Silica-Coated Upconversion Nanoparticles in vivo. *Front Chem* **2019**, *7*, 218-218.
38. Gnach, A.; Lipinski, T.; Bednarkiewicz, A.; Rybka, J.; Capobianco, J. A., Upconverting nanoparticles: assessing the toxicity. *Chemical Society Reviews* **2015**, *44* (6), 1561-1584.



## Bibliography

---

39. Homann, C.; Krukewitt, L.; Frenzel, F.; Grauel, B.; Würth, C.; Resch-Genger, U.; Haase, M., NaYF<sub>4</sub>:Yb,Er/NaYF<sub>4</sub> Core/Shell Nanocrystals with High Upconversion Luminescence Quantum Yield. *Angewandte Chemie International Edition* **2018**, *57* (28), 8765-8769.
  40. Kaiser, M.; Würth, C.; Kraft, M.; Hyppänen, I.; Soukka, T.; Resch-Genger, U., Power-dependent upconversion quantum yield of NaYF<sub>4</sub>:Yb<sup>3+</sup>,Er<sup>3+</sup> nano- and micrometer-sized particles - measurements and simulations. *Nanoscale* **2017**, *9* (28), 10051-10058.
  41. Würth, C.; Fischer, S.; Grauel, B.; Alivisatos, A. P.; Resch-Genger, U., Quantum Yields, Surface Quenching, and Passivation Efficiency for Ultrasmall Core/Shell Upconverting Nanoparticles. *Journal of the American Chemical Society* **2018**, *140* (14), 4922-4928.
  42. Arppe, R.; Hyppänen, I.; Perala, N.; Peltomaa, R.; Kaiser, M.; Würth, C.; Christ, S.; Resch-Genger, U.; Schäferling, M.; Soukka, T., Quenching of the upconversion luminescence of NaYF<sub>4</sub>:Yb<sup>3+</sup>,Er<sup>3+</sup> and NaYF<sub>4</sub>:Yb<sup>3+</sup>,Tm<sup>3+</sup> nanophosphors by water: the role of the sensitizer Yb<sup>3+</sup> in non-radiative relaxation. *Nanoscale* **2015**, *7* (27), 11746-11757.
  43. Lyu, L.; Cheong, H.; Ai, X.; Zhang, W.; Li, J.; Yang, H.; Lin, J.; Xing, B., Near-infrared light-mediated rare-earth nanocrystals: recent advances in improving photon conversion and alleviating the thermal effect. *NPG Asia Materials* **2018**, *10* (8), 685-702.
  44. Wiesholler, L. M.; Frenzel, F.; Grauel, B.; Würth, C.; Resch-Genger, U.; Hirsch, T., Yb,Nd,Er-doped upconversion nanoparticles: 980 nm versus 808 nm excitation. *Nanoscale* **2019**, *11* (28), 13440-13449.
  45. Wang, X.; Valiev, R. R.; Ohulchanskyy, T. Y.; Ågren, H.; Yang, C.; Chen, G., Dye-sensitized lanthanide-doped upconversion nanoparticles. *Chemical Society Reviews* **2017**, *46* (14), 4150-4167.
  46. Wen, S.; Zhou, J.; Schuck, P. J.; Suh, Y. D.; Schmidt, T. W.; Jin, D., Future and challenges for hybrid upconversion nanosystems. *Nature Photonics* **2019**, *13* (12), 828-838.
  47. Das, A.; Mao, C.; Cho, S.; Kim, K.; Park, W., Over 1000-fold enhancement of upconversion luminescence using water-dispersible metal-insulator-metal nanostructures. *Nature Communications* **2018**, *9* (1), 4828.
  48. Dong, J.; Gao, W.; Han, Q.; Wang, Y.; Qi, J.; Yan, X.; Sun, M., Plasmon-enhanced upconversion photoluminescence: Mechanism and application. *Reviews in Physics* **2019**, *4*, 100026.
  49. Park, W.; Lu, D.; Ahn, S., Plasmon enhancement of luminescence upconversion. *Chemical Society Reviews* **2015**, *44* (10), 2940-2962.
  50. Fischer, S.; Johnson, N. J. J.; Pichaandi, J.; Goldschmidt, J. C.; van Veggel, F. C. J. M., Upconverting core-shell nanocrystals with high quantum yield under low irradiance: On the role of isotropic and thick shells. *Journal of Applied Physics* **2015**, *118* (19), 193105.
  51. Boyer, J. C.; van Veggel, F., Absolute quantum yield measurements of colloidal NaYF<sub>4</sub>: Er<sup>3+</sup>, Yb<sup>3+</sup> upconverting nanoparticles. *Nanoscale* **2010**, *2* (8), 1417-1419.
  52. Page, R. H.; Schaffers, K. I.; Waide, P. A.; Tassano, J. B.; Payne, S. A.; Krupke, W. F.; Bishel, W. K., Upconversion-pumped luminescence efficiency of rare-earth-doped hosts sensitized with trivalent ytterbium. *Journal of the Optical Society of America B-Optical Physics* **1998**, *15* (3), 996-1008.
  53. Fischer, S.; Martin-Rodriguez, R.; Frohlich, B.; Kramer, K. W.; Meijerink, A.; Goldschmidt, J. C., Upconversion quantum yield of Er<sup>3+</sup>-doped β-NaYF<sub>4</sub> and Gd<sub>2</sub>O<sub>2</sub>S: The effects of host lattice, Er<sup>3+</sup> doping, and excitation spectrum bandwidth. *Journal of Luminescence* **2014**, *153*, 281-287.
  54. Pokhrel, M.; Kumar, G. A.; Sardar, D. K., Highly efficient NIR to NIR and VIS upconversion in Er<sup>3+</sup> and Yb<sup>3+</sup> doped in M<sub>2</sub>O<sub>2</sub>S (M = Gd, La, Y). *Journal of Materials Chemistry A* **2013**, *1* (38), 11595-11606.
  55. Würth, C.; Kaiser, M.; Wilhelm, S.; Grauel, B.; Hirsch, T.; Resch-Genger, U., Excitation power dependent population pathways and absolute quantum yields of upconversion nanoparticles in different solvents. *Nanoscale* **2017**, *9* (12), 4283-4294.
  56. Lakowicz, J., *Principles of Fluorescence Spectroscopy*. 2006; 3<sup>rd</sup> Edition.
-

57. Bloembergen, N., Solid State Infrared Quantum Counters. *Physical Review Letters* **1959**, 2 (3), 84-85.
  58. Auzel, F. E., Materials and devices using double-pumped-phosphors with energy transfer. *Proceedings of the IEEE* **1973**, 61 (6), 758-786.
  59. Nadort, A.; Zhao, J. B.; Goldys, E. M., Lanthanide upconversion luminescence at the nanoscale: fundamentals and optical properties. *Nanoscale* **2016**, 8 (27), 13099-13130.
  60. Goldschmidt, J. C.; Fischer, S., Upconversion for Photovoltaics - a Review of Materials, Devices and Concepts for Performance Enhancement. *Advanced Optical Materials* **2015**, 3 (4), 510-535.
  61. Streck, W.; Deren, P.; Bednarkiewicz, A., Cooperative processes in KYb(WO<sub>4</sub>)<sub>2</sub> crystal doped with Eu<sup>3+</sup> and Tb<sup>3+</sup> ions. *Journal of Luminescence* **2000**, 87-89, 999-1001.
  62. Arai, Y.; Yamashita, T.; Suzuki, T.; Ohishi, Y., Upconversion properties of Tb<sup>3+</sup>-Yb<sup>3+</sup> codoped fluorophosphate glasses. *Journal of Applied Physics* **2009**, 105 (8), 083105.
  63. Hernández, I.; Pathumakanthar, N.; Wyatt, P. B.; Gillin, W. P., Cooperative Infrared to Visible Up Conversion in Tb<sup>3+</sup>, Eu<sup>3+</sup>, and Yb<sup>3+</sup> Containing Polymers. *Advanced Materials* **2010**, 22 (47), 5356-5360.
  64. Teuchner, K.; Ehlert, J.; Freyer, W.; Leupold, D.; Altmeyer, P.; Stücker, M.; Hoffmann, K., Fluorescence Studies of Melanin by Stepwise Two-Photon Femtosecond Laser Excitation. *Journal of Fluorescence* **2000**, 10 (3), 275-275.
  65. Helmchen, F.; Denk, W., Deep tissue two-photon microscopy. *Nature Methods* **2005**, 2 (12), 932-940.
  66. Meiling, T. T.; Cywiński, P. J.; Löhmansröben, H.-G., Two-Photon Excitation Fluorescence Spectroscopy of Quantum Dots: Photophysical Properties and Application in Bioassays. *The Journal of Physical Chemistry C* **2018**, 122 (17), 9641-9647.
  67. Masada, G.; Suzudo, T.; Satoh, Y.; Ishizuki, H.; Taira, T.; Furusawa, A., Efficient generation of highly squeezed light with periodically poled MgO:LiNbO<sub>3</sub>. *Opt. Express* **2010**, 18 (12), 13114-13121.
  68. Gharaati, S.; Wang, C.; Förster, C.; Weigert, F.; Resch-Genger, U.; Heinze, K., Triplet-Triplet Annihilation Upconversion in a MOF with Acceptor-Filled Channels. *Chemistry – A European Journal* **2020**, 26 (5), 960-960.
  69. Park, J.; Xu, M.; Li, F.; Zhou, H.-C., 3D Long-Range Triplet Migration in a Water-Stable Metal–Organic Framework for Upconversion-Based Ultralow-Power in Vivo Imaging. *Journal of the American Chemical Society* **2018**, 140 (16), 5493-5499.
  70. Kouno, H.; Sasaki, Y.; Yanai, N.; Kimizuka, N., Supramolecular Crowding Can Avoid Oxygen Quenching of Photon Upconversion in Water. *Chemistry – A European Journal* **2019**, 25 (24), 6038-6038.
  71. Balushev, S.; Katta, K.; Avlasevich, Y.; Landfester, K., Annihilation upconversion in nanoconfinement: solving the oxygen quenching problem. *Materials Horizons* **2016**, 3 (6), 478-486.
  72. Filatov, M. A.; Balushev, S.; Landfester, K., Protection of densely populated excited triplet state ensembles against deactivation by molecular oxygen. *Chemical Society Reviews* **2016**, 45 (17), 4668-4689.
  73. Auzel, F., Multiphonon Processes, Cross-Relaxation and Up-Conversion in Ion-Activated Solids, Exemplified By Minilaser Materials. In *Radiationless Processes*, DiBartolo, B.; Goldberg, V., Eds. Springer US: Boston, MA, 1980; pp 213-286.
  74. Förster, T., Energiewanderung und Fluoreszenz. *Naturwissenschaften* **1946**, 33 (6), 166-175.
  75. Dexter, D. L., Theory of Sensitized Luminescence in Solids. *Journal of Chemical Physics* **1953**, 21, 836-850.
  76. Inokuti, M.; Hirayama, F., Influence of Energy Transfer by the Exchange Mechanism on Donor Luminescence. *The Journal of Chemical Physics* **1965**, 43 (6), 1978-1989.
  77. Yamada, N.; Shionoya, S.; Kushida, T., Phonon-Assisted Energy Transfer between Trivalent Rare Earth Ions. *Journal of the Physical Society of Japan* **1972**, 32 (6), 1577-1586.
-

## Bibliography

---

78. Miyakawa, T.; Dexter, D. L., Phonon Sidebands, Multiphonon Relaxation of Excited States, and Phonon-Assisted Energy Transfer between Ions in Solids. *Physical Review B* **1970**, *1* (7), 2961-2969.
79. A. M. Dirac, P., *The Quantum Theory of Emission and Absorption of Radiation*. 1927; 114, p 243-265.
80. Mahata, M. K.; Hofsäss, H.; Vetter, U., Photon-Upconverting Materials: Advances and Prospects for Various Emerging Applications. 2016; pp 109-131.
81. Strohhöfer, C.; Polman, A., Absorption and emission spectroscopy in  $\text{Er}^{3+}$ - $\text{Yb}^{3+}$  doped aluminum oxide waveguides. *Optical Materials* **2003**, *21* (4), 705-712.
82. Shen, B.; Cheng, S.; Gu, Y.; Ni, D.; Gao, Y.; Su, Q.; Feng, W.; Li, F., Revisiting the optimized doping ratio in core/shell nanostructured upconversion particles. *Nanoscale* **2017**, *9* (5), 1964-1971.
83. Gargas, D. J.; Chan, E. M.; Ostrowski, A. D.; Aloni, S.; Altoe, M. V. P.; Barnard, E. S.; Sanii, B.; Urban, J. J.; Milliron, D. J.; Cohen, B. E.; Schuck, P. J., Engineering bright sub-10-nm upconverting nanocrystals for single-molecule imaging. *Nature Nanotechnology* **2014**, *9* (4), 300-305.
84. N. Russell, H.; A. Saunders, F., New Regularities in the Spectra of the Alkaline Earths. *The Astrophysical Journal* **1924**, *61*, 38.
85. Walsh, B., Judd-Ofelt theory: Principles and practices. 2005; pp 403-433.
86. Görrler-Walrand, C.; Binnemans, K., Chapter 155 Rationalization of crystal-field parametrization. In *Handbook on the Physics and Chemistry of Rare Earths*, Elsevier: 1996; Vol. 23, pp 121-283.
87. Capobianco, J. A.; Vetrone, F.; Boyer, J. C.; Speghini, A.; Bettinelli, M., Enhancement of Red Emission ( $^4\text{F}_{9/2} \rightarrow ^4\text{I}_{15/2}$ ) via Upconversion in Bulk and Nanocrystalline Cubic  $\text{Y}_2\text{O}_3\text{:Er}^{3+}$ . *The Journal of Physical Chemistry B* **2002**, *106* (6), 1181-1187.
88. van de Rijke, F.; Zijlmans, H.; Li, S.; Vail, T.; Raap, A. K.; Niedbala, R. S.; Tanke, H. J., Up-converting phosphor reporters for nucleic acid microarrays. *Nature Biotechnology* **2001**, *19* (3), 273-276.
89. Heer, S.; Lehmann, O.; Haase, M.; Güdel, H.-U., Blue, Green, and Red Upconversion Emission from Lanthanide-Doped  $\text{LuPO}_4$  and  $\text{YbPO}_4$  Nanocrystals in a Transparent Colloidal Solution. *Angewandte Chemie International Edition* **2003**, *42* (27), 3179-3182.
90. Heer, S.; Kömpe, K.; Güdel, H.-U.; Haase, M., Highly Efficient Multicolour Upconversion Emission in Transparent Colloids of Lanthanide-Doped  $\text{NaYF}_4$  Nanocrystals. *Advanced Materials* **2004**, *16* (23-24), 2102-2105.
91. Wang, G.; Peng, Q.; Li, Y., Upconversion Luminescence of Monodisperse  $\text{CaF}_2\text{:Yb}^{3+}/\text{Er}^{3+}$  Nanocrystals. *Journal of the American Chemical Society* **2009**, *131* (40), 14200-14201.
92. Chen, D.; Lei, L.; Zhang, R.; Yang, A.; Xu, J.; Wang, Y., Intrinsic single-band upconversion emission in colloidal  $\text{Yb/Er(Tm):Na}_3\text{Zr(Hf)F}_7$  nanocrystals. *Chemical Communications* **2012**, *48* (86), 10630-10632.
93. Menyuk, N.; Dwight, K.; Pierce, J. W.,  $\text{NaYF}_4$  : Yb,Er—an efficient upconversion phosphor. *Applied Physics Letters* **1972**, *21* (4), 159-161.
94. Suyver, J. F.; Grimm, J.; Krämer, K. W.; Güdel, H. U., Highly efficient near-infrared to visible up-conversion process in  $\text{NaYF}_4\text{:Er}^{3+},\text{Yb}^{3+}$ . *Journal of Luminescence* **2005**, *114* (1), 53-59.
95. Lay, A.; H. Sheppard, O.; Siefe, C.; A. McLellan, C.; D. Mehlenbacher, R.; Fischer, S.; Goodman, M.; A. Dionne, J., Optically Robust and Biocompatible Mechanosensitive Upconverting Nanoparticles. *ACS Central Science* **2019**.
96. Wang, F.; Han, Y.; Lim, C. S.; Lu, Y.; Wang, J.; Xu, J.; Chen, H.; Zhang, C.; Hong, M.; Liu, X., Simultaneous phase and size control of upconversion nanocrystals through lanthanide doping. *Nature* **2010**, *463*, 1061.
97. Renero-Lecuna, C.; Martín-Rodríguez, R.; Valiente, R.; González, J.; Rodríguez, F.; Krämer, K. W.; Güdel, H. U., Origin of the High Upconversion Green Luminescence Efficiency in  $\beta\text{-NaYF}_4\text{:2\%Er}^{3+},\text{20\%Yb}^{3+}$ . *Chemistry of Materials* **2011**, *23* (15), 3442-3448.
-

98. Klier, D. T.; Kumke, M. U., Analysing the effect of the crystal structure on upconversion luminescence in Yb<sup>3+</sup>,Er<sup>3+</sup>-co-doped NaYF<sub>4</sub> nanomaterials. *Journal of Materials Chemistry C* **2015**, *3* (42), 11228-11238.
99. Riseberg, L. A.; Moos, H. W., Multiphonon Orbit-Lattice Relaxation of Excited States of Rare-Earth Ions in Crystals. *Physical Review* **1968**, *174* (2), 429-438.
100. Wermuth, M.; Riedener, T.; Güdel, H. U., Spectroscopy and upconversion mechanisms of CsCdBr<sub>3</sub>Dy<sup>3+</sup>. *Physical Review B* **1998**, *57* (8), 4369-4376.
101. Rabouw, F. T.; Prins, P. T.; Villanueva-Delgado, P.; Castelijns, M.; Geitenbeek, R. G.; Meijerink, A., Quenching Pathways in NaYF<sub>4</sub>:Er<sup>3+</sup>,Yb<sup>3+</sup> Upconversion Nanocrystals. *ACS Nano* **2018**, *12* (5), 4812-4823.
102. Anderson, R. B.; Smith, S. J.; May, P. S.; Berry, M. T., Revisiting the NIR-to-Visible Upconversion Mechanism in beta-NaYF<sub>4</sub>:Yb<sup>3+</sup>,Er<sup>3+</sup>. *J Phys Chem Lett* **2014**, *5* (1), 36-42.
103. Berry, M. T.; May, P. S., Disputed Mechanism for NIR-to-Red Upconversion Luminescence in NaYF<sub>4</sub>:Yb<sup>3+</sup>,Er<sup>3+</sup>. *Journal of Physical Chemistry A* **2015**, *119* (38), 9805-9811.
104. Wang, F.; Liu, X., Upconversion Multicolor Fine-Tuning: Visible to Near-Infrared Emission from Lanthanide-Doped NaYF<sub>4</sub> Nanoparticles. *Journal of the American Chemical Society* **2008**, *130* (17), 5642-5643.
105. Wang, J.; Deng, R.; MacDonald, M. A.; Chen, B.; Yuan, J.; Wang, F.; Chi, D.; Andy Hor, T. S.; Zhang, P.; Liu, G.; Han, Y.; Liu, X., Enhancing multiphoton upconversion through energy clustering at sublattice level. *Nature Materials* **2013**, *13*, 157.
106. Gao, D.; Zhang, X.; Chong, B.; Xiao, G.; Tian, D., Simultaneous spectra and dynamics processes tuning of a single upconversion microtube through Yb<sup>3+</sup> doping concentration and excitation power. *Physical Chemistry Chemical Physics* **2017**, *19* (6), 4288-4296.
107. Xue, X. J.; Uechi, S.; Tiwari, R. N.; Duan, Z. C.; Liao, M. S.; Yoshimura, M.; Suzuki, T.; Ohishi, Y., Size-dependent upconversion luminescence and quenching mechanism of LiYF<sub>4</sub>: Er<sup>3+</sup>/Yb<sup>3+</sup> nanocrystals with oleate ligand adsorbed. *Opt Mater Express* **2013**, *3* (7).
108. Wei, W.; Zhang, Y.; Chen, R.; Goggi, J.; Ren, N.; Huang, L.; Bhakoo, K. K.; Sun, H. D.; Tan, T. T. Y., Cross Relaxation Induced Pure Red Upconversion in Activator- and Sensitizer-Rich Lanthanide Nanoparticles. *Chemistry of Materials* **2014**, *26* (18), 5183-5186.
109. Wang, Y.; Liu, K.; Liu, X. M.; Dohnalova, K.; Gregorkiewicz, T.; Kong, X. G.; Aalders, M. C. G.; Buma, W. J.; Zhang, H., Critical Shell Thickness of Core/Shell Upconversion Luminescence Nanoplatfrom for FRET Application. *J Phys Chem Lett* **2011**, *2* (17), 2083-2088.
110. Vetrone, F.; Naccache, R.; Mahalingam, V.; Morgan, C. G.; Capobianco, J. A., The Active-Core/Active-Shell Approach: A Strategy to Enhance the Upconversion Luminescence in Lanthanide-Doped Nanoparticles. *Advanced Functional Materials* **2009**, *19* (18), 2924-2929.
111. Liu, G. K., Advances in the theoretical understanding of photon upconversion in rare-earth activated nanophosphors. *Chemical Society Reviews* **2015**, *44* (6), 1635-1652.
112. Bogdan, N.; Vetrone, F.; Ozin, G. A.; Capobianco, J. A., Synthesis of Ligand-Free Colloidally Stable Water Dispersible Brightly Luminescent Lanthanide-Doped Upconverting Nanoparticles. *Nano Letters* **2011**, *11* (2), 835-840.
113. Liu, L.; Jiang, H. L.; Chen, Y. J.; Zhang, X. L.; Zhang, Z. G.; Wang, Y. X., Power dependence of upconversion luminescence of Er<sup>3+</sup> doped Yttria nanocrystals and their bulk counterpart. *Journal of Luminescence* **2013**, *143*, 423-431.
114. Wu, S.; Ning, Y.; Chang, J.; Zhang, S., Upconversion photoluminescence enhancement and modulation of NaYF<sub>4</sub>:Yb, Er through using different ligands. *Journal of Luminescence* **2013**, *143* (0), 492-497.
115. Würth, C.; Grabolle, M.; Pauli, J.; Spieles, M.; Resch-Genger, U., Relative and absolute determination of fluorescence quantum yields of transparent samples. *Nat Protoc* **2013**, *8* (8), 1535-1550.

## Bibliography

---

116. Würth, C.; Grabolle, M.; Pauli, J.; Spieles, M.; Resch-Genger, U., Comparison of Methods and Achievable Uncertainties for the Relative and Absolute Measurement of Photoluminescence Quantum Yields. *Analytical Chemistry* **2011**, *83*, 3431–3439.
117. Tikhomirov, V. K.; Adamo, G.; Nikolaenko, A. E.; Rodriguez, V. D.; Gredin, P.; Mortier, M.; Zheludev, N. I.; Moshchalkov, V. V., Cathodo- and photoluminescence in Yb<sup>3+</sup>-Er<sup>3+</sup> co-doped PbF<sub>2</sub> nanoparticles. *Opt. Express* **2010**, *18* (9), 8836-8846.
118. Pollnau, M.; Gamelin, D. R.; Luthi, S. R.; Gudel, H. U.; Hehlen, M. P., Power dependence of upconversion luminescence in lanthanide and transition-metal-ion systems. *Physical Review B* **2000**, *61* (5), 3337-3346.
119. Liu, H. C.; Xu, C. T.; Lindgren, D.; Xie, H. Y.; Thomas, D.; Gundlach, C.; Andersson-Engels, S., Balancing power density based quantum yield characterization of upconverting nanoparticles for arbitrary excitation intensities. *Nanoscale* **2013**, *5* (11), 4770-4775.
120. Kraft, M.; Würth, C.; Muhr, V.; Hirsch, T.; Resch-Genger, U., Particle-size-dependent upconversion luminescence of NaYF<sub>4</sub>: Yb, Er nanoparticles in organic solvents and water at different excitation power densities. *Nano Research* **2018**, *11* (12), 6360-6374.
121. Pilch, A.; Würth, C.; Kaiser, M.; Wawrzyńczyk, D.; Kurnatowska, M.; Arabasz, S.; Prorok, K.; Samoć, M.; Strek, W.; Resch-Genger, U.; Bednarkiewicz, A., Shaping Luminescent Properties of Yb<sup>3+</sup> and Ho<sup>3+</sup> Co-Doped Upconverting Core–Shell β-NaYF<sub>4</sub> Nanoparticles by Dopant Distribution and Spacing. *Small* **2017**, *13* (47), 1701635.
122. Liu, H.; Huang, K.; Valiev, R. R.; Zhan, Q.; Zhang, Y.; Ågren, H., Photon Upconversion Kinetic Nanosystems and Their Optical Response. *Laser & Photonics Reviews* **2018**, *12* (1), 1700144.
123. Hossan, M. Y.; Hor, A.; Luu, Q.; Smith, S.; May, S.; Mary, B., *Explaining the Nanoscale Effect in the Upconversion Dynamics of β-NaYF<sub>4</sub>:Yb<sup>3+</sup>,Er<sup>3+</sup> Core and Core-Shell Nanocrystals*. 2017; 121.
124. Gai, S. L.; Li, C. X.; Yang, P. P.; Lin, J., Recent Progress in Rare Earth Micro/Nanocrystals: Soft Chemical Synthesis, Luminescent Properties, and Biomedical Applications. *Chemical Reviews* **2014**, *114* (4), 2343-2389.
125. Shen, J.; Chen, G.; Ohulchanskyy, T. Y.; Kesseli, S. J.; Buchholz, S.; Li, Z.; Prasad, P. N.; Han, G., Tunable Near Infrared to Ultraviolet Upconversion Luminescence Enhancement in (α-NaYF<sub>4</sub>:Yb,Tm)/CaF<sub>2</sub> Core/Shell Nanoparticles for In situ Real-time Recorded Biocompatible Photoactivation. *Small* **2013**, *9* (19), 3213-3217.
126. Chen, G.; Shen, J.; Ohulchanskyy, T. Y.; Patel, N. J.; Kutikov, A.; Li, Z.; Song, J.; Pandey, R. K.; Ågren, H.; Prasad, P. N.; Han, G., (α-NaYbF<sub>4</sub>:Tm<sup>3+</sup>)/CaF<sub>2</sub> Core/Shell Nanoparticles with Efficient Near-Infrared to Near-Infrared Upconversion for High-Contrast Deep Tissue Bioimaging. *ACS Nano* **2012**, *6* (9), 8280-8287.
127. Chen, G.; Ohulchanskyy, T. Y.; Kachynski, A.; Ågren, H.; Prasad, P. N., Intense Visible and Near-Infrared Upconversion Photoluminescence in Colloidal LiYF<sub>4</sub>:Er<sup>3+</sup> Nanocrystals under Excitation at 1490 nm. *ACS Nano* **2011**, *5* (6), 4981-4986.
128. D.S. Yasyrkina, S. V. K., A.V. Ryabova, D.V. Pominova, V.V. Voronov, R.P. Ermakov, P.P. Fedorov, Dependence of quantum yield of up-conversion luminescence on the composition of fluorite - typesolid solution NaY<sub>1-x-y</sub>Yb<sub>x</sub>Er<sub>y</sub>F<sub>4</sub>. *NANOSYSTEMS: PHYSICS, CHEMISTRY, MATHEMATICS* **2013**, *4* (5), 648–656.
129. Liu, Q.; Sun, Y.; Yang, T.; Feng, W.; Li, C.; Li, F., Sub-10 nm Hexagonal Lanthanide-Doped NaLuF<sub>4</sub> Upconversion Nanocrystals for Sensitive Bioimaging in Vivo. *Journal of the American Chemical Society* **2011**, *133* (43), 17122-17125.
130. Xu, C. T.; Svenmarker, P.; Liu, H.; Wu, X.; Messing, M. E.; Wallenberg, L. R.; Andersson-Engels, S., High-Resolution Fluorescence Diffuse Optical Tomography Developed with Nonlinear Upconverting Nanoparticles. *ACS Nano* **2012**, *6* (6), 4788-4795.
131. Li, X.; Wang, R.; Zhang, F.; Zhao, D., Engineering Homogeneous Doping in Single Nanoparticle To Enhance Upconversion Efficiency. *Nano Letters* **2014**, *14* (6), 3634-3639.
-

132. Fischer, S.; Bronstein, N. D.; Swabeck, J. K.; Chan, E. M.; Alivisatos, A. P., Precise Tuning of Surface Quenching for Luminescence Enhancement in Core–Shell Lanthanide-Doped Nanocrystals. *Nano Letters* **2016**, *16* (11), 7241-7247.
133. Wang, F.; Wang, J. A.; Liu, X. G., Direct Evidence of a Surface Quenching Effect on Size-Dependent Luminescence of Upconversion Nanoparticles. *Angewandte Chemie-International Edition* **2010**, *49* (41), 7456-7460.
134. Naccache, R.; Vetrone, F.; Mahalingam, V.; Cuccia, L. A.; Capobianco, J. A., Controlled Synthesis and Water Dispersibility of Hexagonal Phase NaGdF<sub>4</sub>:Ho<sup>3+</sup>/Yb<sup>3+</sup> Nanoparticles. *Chemistry of Materials* **2009**, *21* (4), 717-723.
135. Sudarsan, V.; van Veggel, F.; Herring, R. A.; Raudsepp, M., Surface Eu<sup>3+</sup> ions are different than "bulk" Eu<sup>3+</sup> ions in crystalline doped LaF<sub>3</sub> nanoparticles. *Journal of Materials Chemistry* **2005**, *15* (13), 1332-1342.
136. Wang, Y.; Smolarek, S.; Kong, X. G.; Buma, W. J.; Brouwer, A. M.; Zhang, H., Effect of Surface Related Organic Vibrational Modes in Luminescent Upconversion Dynamics of Rare Earth Ions Doped Nanoparticles. *J Nanosci Nanotechnol* **2010**, *10* (11), 7149-7153.
137. Boyer, J. C.; Manseau, M. P.; Murray, J. I.; van Veggel, F., Surface Modification of Upconverting NaYF<sub>4</sub> Nanoparticles with PEG-Phosphate Ligands for NIR (800 nm) Biolabeling within the Biological Window. *Langmuir* **2010**, *26* (2), 1157-1164.
138. Wilhelm, S.; Kaiser, M.; Würth, C.; Heiland, J.; Carrillo-Carrion, C.; Muhr, V.; Wolfbeis, O. S.; Parak, W. J.; Resch-Genger, U.; Hirsch, T., Water dispersible upconverting nanoparticles: effects of surface modification on their luminescence and colloidal stability. *Nanoscale* **2015**, *7* (4), 1403-1410.
139. Quintanilla, M.; Cantarelli, I. X.; Pedroni, M.; Speghini, A.; Vetrone, F., Intense ultraviolet upconversion in water dispersible SrF<sub>2</sub>: Tm<sup>3+</sup>, Yb<sup>3+</sup> nanoparticles: the effect of the environment on light emissions. *Journal of Materials Chemistry C* **2015**, *3* (13), 3108-3113.
140. Arppe, R.; Nareoja, T.; Nylund, S.; Mattsson, L.; Koho, S.; Rosenholm, J. M.; Soukka, T.; Schaferling, M., Photon upconversion sensitized nanoprobe for sensing and imaging of pH. *Nanoscale* **2014**, *6* (12), 6837-6843.
141. Mai, H. X.; Zhang, Y. W.; Sun, L. D.; Yan, C. H., Size- and phase-controlled synthesis of monodisperse NaYF<sub>4</sub>: Yb,Er nanocrystals from a unique delayed nucleation pathway monitored with upconversion spectroscopy. *J Phys Chem C* **2007**, *111* (37), 13730-13739.
142. Xu, D.; Liu, C.; Yan, J.; Yang, S.; Zhang, Y., Understanding Energy Transfer Mechanisms for Tunable Emission of Yb<sup>3+</sup>-Er<sup>3+</sup> Codoped GdF<sub>3</sub> Nanoparticles: Concentration-Dependent Luminescence by Near-Infrared and Violet Excitation. *The Journal of Physical Chemistry C* **2015**, *119* (12), 6852-6860.
143. Liao, J. S.; Nie, L. L.; Liu, S. H.; Liu, B.; Wen, H. R., Yb<sup>3+</sup> concentration dependence of upconversion luminescence in Y<sub>2</sub>Sn<sub>2</sub>O<sub>7</sub>:Yb<sup>3+</sup>/Er<sup>3+</sup> nanophosphors. *Journal of Materials Science* **2014**, *49* (17), 6081-6086.
144. Zhao, J.; Sun, Y.; Kong, X.; Tian, L.; Wang, Y.; Tu, L.; Zhao, J.; Zhang, H., Controlled Synthesis, Formation Mechanism, and Great Enhancement of Red Upconversion Luminescence of NaYF<sub>4</sub>:Yb<sup>3+</sup>, Er<sup>3+</sup> Nanocrystals/Submicroplates at Low Doping Level. *The Journal of Physical Chemistry B* **2008**, *112* (49), 15666-15672.
145. Zhu, H.; Lin, M.; Jin, G.; Lu, T. J.; Xu, F., A modified energy transfer model for determination of upconversion emission of β-NaYF<sub>4</sub>:Yb,Er: Role of self-quenching effect. *Journal of Luminescence* **2017**, *185*, 292-297.
146. Li, D.; Qin, W.; Zhao, D.; Aidilibike, T.; Chen, H.; Liu, S.; Zhang, P.; Wang, L., Tunable green to red upconversion fluorescence of water-soluble hexagonal-phase core-shell CaF<sub>2</sub>@NaYF<sub>4</sub> nanocrystals. *Opt Mater Express* **2016**, *6* (1), 270-278.

## Bibliography

---

147. Soukka, T.; Kuningas, K.; Rantanen, T.; Haaslahti, V.; Lovgren, T., Photochemical characterization of up-converting inorganic lanthanide phosphors as potential labels. *Journal of Fluorescence* **2005**, *15* (4), 513-528.
148. Ylihärsilä, M.; Harju, E.; Arppe, R.; Hattara, L.; Hölsä, J.; Saviranta, P.; Soukka, T.; Waris, M., Genotyping of clinically relevant human adenoviruses by array-in-well hybridization assay. *Clinical Microbiology and Infection* **2013**, *19* (6), 551-557.
149. Li, Z.; Zhang, Y.; Jiang, S., Multicolor Core/Shell-Structured Upconversion Fluorescent Nanoparticles. *Advanced Materials* **2008**, *20* (24), 4765-4769.
150. Würth, C.; Pauli, J.; Lochmann, C.; Spieles, M.; Resch-Genger, U., Integrating Sphere Setup for the Traceable Measurement of Absolute Photoluminescence Quantum Yields in the Near Infrared. *Analytical Chemistry* **2012**, *84* (3), 1345-1352.
151. Resch-Genger, U.; Bremser, W.; Pfeifer, D.; Spieles, M.; Hoffmann, A.; DeRose, P. C.; Zwinkels, J. C.; Gauthier, F.; Ebert, B.; Taubert, R. D.; Voigt, J.; Hollandt, J.; Macdonald, R., State-of-the Art Comparability of Corrected Emission Spectra. 2. Field Laboratory Assessment of Calibration Performance Using Spectral Fluorescence Standards. *Analytical Chemistry* **2012**, *84* (9), 3899-3907.
152. Bergstrand, J.; Liu, Q.; Huang, B.; Peng, X.; Würth, C.; Resch-Genger, U.; Zhan, Q.; Widengren, J.; Ågren, H.; Liu, H., On the decay time of upconversion luminescence. *Nanoscale* **2019**, *11* (11), 4959-4969.
153. MacDougall, S. K. W.; Ivaturi, A.; Marques-Hueso, J.; Richards, B. S., Measurement procedure for absolute broadband infrared up-conversion photoluminescent quantum yields: correcting for absorption/re-emission. *Rev Sci Instrum* **2014**, *85* (6), 063109.
154. C., d. M. J.; Felix, W. H.; H., F. R., An improved experimental determination of external photoluminescence quantum efficiency. *Advanced Materials* **1997**, *9* (3), 230-232.
155. Tian, B.; Fernandez-Bravo, A.; Najafiaghdam, H.; Torquato, N. A.; Altoe, M. V. P.; Teitelboim, A.; Tajon, C. A.; Tian, Y.; Borys, N. J.; Barnard, E. S.; Anwar, M.; Chan, E. M.; Schuck, P. J.; Cohen, B. E., Low irradiance multiphoton imaging with alloyed lanthanide nanocrystals. *Nature Communications* **2018**, *9* (1), 3082.
156. Marciniak, L.; Waszniewska, K.; Bednarkiewicz, A.; Hreniak, D.; Strek, W., Sensitivity of a Nanocrystalline Luminescent Thermometer in High and Low Excitation Density Regimes. *The Journal of Physical Chemistry C* **2016**, *120* (16), 8877-8882.
157. Brites, C. D. S.; Balabhadra, S.; Carlos, L. D., Lanthanide-Based Thermometers: At the Cutting-Edge of Luminescence Thermometry. *Advanced Optical Materials* **2019**, *7* (5), 1801239.
158. Fafara, A. Near-Infrared Spectroscopic Measurement of Tissue Temperature, In-Vivo. Dissertation, Mc Gill University, 2000.
159. Lappi, S. E.; Smith, B.; Franzen, S., Infrared spectra of H(2)16O, H(2)18O and D(2)O in the liquid phase by single-pass attenuated total internal reflection spectroscopy. *Spectrochimica Acta Part A: Molecular and Biomolecular Spectroscopy* **2004**, *60* (11), 2611-2619.
160. Fischer, S.; Ivaturi, A.; Fröhlich, B.; Rüdiger, M.; Richter, A.; Kramer, K. W.; Richards, B. S.; Goldschmidt, J. C., Upconverter Silicon Solar Cell Devices for Efficient Utilization of Sub-Band-Gap Photons Under Concentrated Solar Radiation. *IEEE Journal of Photovoltaics* **2014**, *4* (1), 183-189.
161. Zhao, J.; Lu, Z.; Yin, Y.; McRae, C.; Piper, J. A.; Dawes, J. M.; Jin, D.; Goldys, E. M., Upconversion luminescence with tunable lifetime in NaYF<sub>4</sub>:Yb,Er nanocrystals: role of nanocrystal size. *Nanoscale* **2013**, *5* (3), 944-52.
162. Hudry, D.; Busko, D.; Popescu, R.; Gerthsen, D.; Abeykoon, A. M. M.; Kubel, C.; Bergfeldt, T.; Richards, B. S., Direct Evidence of Significant Cation Intermixing in Upconverting Core@Shell Nanocrystals: Toward a New Crystallochemical Model. *Chemistry of Materials* **2017**, *29* (21), 9238-9246.
163. Duhnen, S.; Haase, M., Study on the Intermixing of Core and Shell in NaEuF<sub>4</sub>/NaGdF<sub>4</sub> Core/Shell Nanocrystals. *Chemistry of Materials* **2015**, *27* (24), 8375-8386.
-

164. Kaiser, M.; Würth, C.; Kraft, M.; Soukka, T.; Resch-Genger, U., Explaining the influence of dopant concentration and excitation power density on the luminescence and brightness of  $\beta$ -NaYF<sub>4</sub>:Yb<sup>3+</sup>,Er<sup>3+</sup> nanoparticles: Measurements and simulations. *Nano Research* **2019**, 12 (8), 1871-1879.



## List of Publications

### First-author publication related to the upconversion research field referred in the text with capital roman numerals

- P1. M. Kaiser, C. Würth, M. Kraft, I. Hyppänen, T. Soukka, U. Resch-Genger  
**„Power-dependent upconversion quantum yield of NaYF<sub>4</sub>: Yb<sup>3+</sup>, Er<sup>3+</sup> nano-and micrometer-sized particles – measurements and simulations“**  
*Nanoscale*, **2017**, 9, 10051-10058  
DOI: 10.1039/C7NR02449E
- P2. C. Würth\*, M. Kaiser\*, S. Wilhelm, B. Grauel, T. Hirsch, U. Resch-Genger  
**„Excitation power dependent population pathways and absolute quantum yields of upconversion nanoparticles in different solvents“**  
*Nanoscale*, **2017**, 9, 4283-4294  
DOI: 10.1039/C7NR00092H  
\*equally contributed
- P3. M. Kaiser, C. Würth, M. Kraft, T. Soukka, U. Resch-Genger  
**“Explaining the influence of dopant concentration and excitation power density on the luminescence and brightness of  $\beta$ -NaYF<sub>4</sub>:Yb<sup>3+</sup>,Er<sup>3+</sup> nanoparticles: Measurements and simulations”**  
*Nanoresearch*, **2019**, 12, 1871-1879

### First-author publication unrelated to the upconversion research field

- P4. M. Müller\*, M. Kaiser\*, G.M. Stachowski, U. Resch-Genger, N. Gaponik, A. Eychmüller  
**“Photoluminescence Quantum Yield and Matrix-Induced Luminescence Enhancement of Colloidal Quantum Dots Embedded in Ionic Crystals”**  
*Chemistry of Materials*, **2014**, 26 (10), 3231-3237  
DOI: 10.1021/cm5009043  
\*equally contributed

### Co-authored publications related to the upconversion research field

- P5. S. Wilhelm, M. Kaiser, C. Würth, J. Heiland, C. Carrillo-Carrion, V. Muhr, O.S. Wolfbeis, W.J. Parak, U. Resch-Genger, T. Hirsch  
**“Water dispersible upconverting nanoparticles: effects of surface modification on their luminescence and colloidal stability”**  
*Nanoscale*, **2015**, 7, 1403-1410  
DOI: 10.1039/c4nr05954a

- P6. R. Arppe, I. Hyppänen, N. Perälä, R. Peltomaa, M. Kaiser, C. Würth, S. Christ, U. Resch-Genger, M. Schäferling, T. Soukka  
**"Quenching of the upconversion luminescence of NaYF<sub>4</sub>: Yb<sup>3+</sup>, Er<sup>3+</sup> and NaYF<sub>4</sub>: Yb<sup>3+</sup>, Tm<sup>3+</sup> nanophosphors by water: the role of the sensitizer Yb<sup>3+</sup> in non-radiative relaxation"**  
*Nanoscale*, **2015**, 7, 133-143  
DOI: 10.1039/C5NR02100F
- P7. A. Pilch, C. Würth, M. Kaiser, D. Wawrzyńczyk, M. Kurnatowska, S. Arabasz, K. Prorok, M. Samoć, W. Strek, U. Resch-Genger, A. Bednarkiewicz  
**"Shaping Luminescent Properties of Yb<sup>3+</sup> and Ho<sup>3+</sup> Co-Doped Upconverting Core-Shell  $\beta$ -NaYF<sub>4</sub> Nanoparticles by Dopant Distribution and Spacing"**  
*Small*, **2017**, 13, 1701635  
DOI: 10.1002/sml.201770246

### Co-authored publications unrelated to upconversion research field

- P8. C. Würth, D. Geißler, T. Behnke, M. Kaiser, U. Resch-Genger  
**"Critical review of the determination of photoluminescence quantum yields of luminescent reporters"**  
*Analytical and bioanalytical chemistry*, **2015**, 407, 59-78  
DOI: 10.1007/s00216-014-8130-z
- P9. S. Hatami, C. Würth, M. Kaiser, S. Leubner, S. Gabriel, L. Bahrig, V. Lesnyak, J. Pauli, N. Gaponik, A. Eychmüller, U. Resch-Genger  
**"Absolute photoluminescence quantum yields of IR26 and IR-emissive Cd<sub>1-x</sub>Hg<sub>x</sub>Te and PbS quantum dots—method and material-inherent challenges"**  
*Nanoscale*, **2015**, 7, 133-143  
DOI: 10.1039/C4NR04608K
- P10. M.M. Lezhnina, H. Kätker, M. Kaiser, L. Stegemann, E. Voss, U. Resch-Genger, C. Strassert, U. Kynast  
**"Absolute Quantum Efficiencies and Chemical Behaviour of Lanthanide Borate Phosphors and Glazes"**  
*Journal of Luminescence*, **2016**, 70, 387-394  
DOI: 10.1016/j.jlumin.2015.05.005
- P11. M.R. Wagner, G. Callsen, J.S. Reparaz, J.-H. Schulze, R. Kirste, M. Cobet, I.A. Ostapenko, S. Rodt, C. Nenstiel, M. Kaiser, A. Hoffmann, A.V. Rodina, M.R. Phillips, S. Lautenschläger, S. Eisermann, B.K. Meyer  
**"Bound excitons in ZnO: Structural defect complexes versus shallow impurity centers"**  
*Physical Review B*, **2011**, 84 (3), 035313  
DOI: 10.1103/PhysRevB.84.035313
-

## List of publications

---

- P12. B.K. Meyer, J. Sann, S. Eisermann, S. Lautenschlaeger, M.R. Wagner, M Kaiser, G. Callsen, J.S. Reparaz, A. Hoffmann  
**"Excited state properties of donor bound excitons in ZnO"**  
*Physical Review B*, **2010**, 82 (11), 115207  
DOI: 10.1103/PhysRevB.82.115207
- P13. G. Durkaya, M. Bügler, R. Atalay, I. Senevirathna, M. Alevli, O. Hitzemann, M. Kaiser, R. Kirste, A. Hoffmann, N. Dietz  
**"The influence of the group V/III molar precursor ratio on the structural properties of InGaN layers grown by HPCVD"**  
*physica status solidi (a)*, **2010**, 207 (6), 1379-1382  
DOI: 10.1002/pssa.200983622
- P14. G. Durkaya, M. Alevli, M. Bügler, R. Atalay, S. Gamage, M. Kaiser, R. Kirste, A. Hoffmann, M. Jamil, I. Ferguson, N. Dietz  
**"Growth temperature-phase stability relation in  $\text{In}_{1-x}\text{Ga}_x\text{N}$  epilayers grown by high-pressure CVD"**  
*MRS Proceedings*, **2009**, 1202, 1202-I05-21  
DOI: 10.1557/PROC-1202-I05-21

## Conference Talks and Posters

This list concludes all first-author conference talks and poster presentations.

- C1. M. Kaiser, C. Würth, I. Hyppänen, E. Palo, T. Soukka, U. Resch-Genger **“Optical conversion efficiency of up-conversion nanoparticles as new class of luminescent reporters”** *ICL 2014*, Wroclaw, Poland, **2014**
- C2. M. Kaiser, C. Würth, I. Hyppänen, E. Palo, T. Soukka, U. Resch-Genger **“Upconversion quantum yields of rare earth doped nanoparticles dependent on dopant concentration”** *78th DPG Spring Meeting 2014*, Dresden, Germany, **2014**
- C3. M. Kaiser, C. Würth, U. Resch-Genger, I. Hyppänen, T. Soukka **“Integration Sphere Setup for the Absolute Determination of Upconversion Quantum Yields of Lanthanide Doped Nanoparticles”** *iNOW2013 International Nano Optoelectronics Workshop*, Cargese, France, **2013**
- C4. M. Kaiser, S. Wilhelm, C. Würth, J. Heiland, O.S. Wolfbeis, T. Hirsch, U. Resch-Genger **“Luminescence Properties of Upconverting NaYF<sub>4</sub>(Yb,Er) Nanoparticles in water and heavy water”** *13th Conference on Methods and Applications of Fluorescence (MAF 13)*, Genoa, Italy, **2013**
- C5. M. Kaiser, C. Würth, U. Resch-Genger, I. Hyppänen, T. Soukka **“Upconversion nanoparticles as new class of fluorescent reporters – Tools to characterize their signal-relevant optical properties”** *Biosensor Symposium*, Berlin, Germany, **2013**
- C6. M. Kaiser, C. Würth, U. Resch-Genger, I. Hyppänen, T. Soukka **“Tools for the characterization of the signal-relevant properties of upconversion nanoparticles as new class of fluorescent reporters”** *ANAKON*, Essen, Germany, **2013**
- C7. M. Kaiser, J. Heiland, M. Kraft, C. Würth, S. Wilhelm, V. Muhr, N. Leibl, O. S. Wolfbeis, T. Hirsch, U. Resch-Genger **“Optical characterization of lanthanide doped up-converting nanoparticles”** *BAM Wissensbörse*, Berlin, Germany, **2013**
- C8. M. Kaiser, C. Würth, U. Resch-Genger, I. Hyppänen, T. Soukka **“Absolute Photoluminescence Quantum Yield of Hexagonal NaYF<sub>4</sub>:Er<sup>3+</sup>,Yb<sup>3+</sup> Upconversion Nanoparticles”** *77th DPG Spring Meeting 2013*, Regensburg, Germany, **2013**
- C9. M. Kaiser, C. Würth, M. Vorsthove, T. Felbeck, U. Kynast, U. Resch-Genger **“Luminescence Properties of Cer-dotierten Yttrium-Aluminium-Garnet (YAG:Ce) Nanoparticles - Absolute Quantum Yields and Influence of Particle Size”** *Nano-Additive*, Berlin, Germany, **2012**

- C10. M. Kaiser, C. Würth, T. Felbeck, M. Vorsthove, U. Kynast, U. Resch-Genger  
**"Influence of the Particle Size on the Optical Properties of YAG:Ce"**  
*Photochemie Tagung*, Potsdam, Germany, **2012**
- C11. M. Kaiser, U. Resch-Genger, C. Würth, U. Kynast, T. Felbeck, M. Vorsthove  
**"Luminescence Properties of Cer-dotierten Yttrium-Aluminium-Garnet (YAG:Ce) Nanoparticles"** *Upcore Joint Seminar 2012*, Regensburg, Germany, **2012**
- C12. M. Kaiser, U. Resch-Genger, C. Würth, U. Kynast, T. Felbeck, M. Vorsthove  
**"Luminescence Properties of Cer-dotierten Yttrium-Aluminium-Garnet (YAG:Ce) Nanoparticles - Absolute Quantum Yields and Influence of Particle Size"** *76th DPG Spring Meeting 2012*, Berlin, Germany, **2012**
- C13. M. Kaiser, M. R. Wagner, G. Callsen, A. Hoffmann, S. Lautenschläger, S. Eisermann, B. K. Meyer **"Excitons and their excitation channels in a-plane and c-plane ZnO"** *74th DPG Spring Meeting 2010*, Regensburg, Germany, **2010**

### Acknowledgement

First of all I want to express my gratitude to **Prof. Dr. Axel Hoffmann** from the *Technical University of Berlin* (TU - Berlin) for supervising this work. He sharpened my scientific view on the essential scientific findings. I am very thankful for him providing me a workplace and allowing me to regularly present my results in his workgroup meetings.

Many thanks to **Dr. Ute Resch-Genger** from the *Federal Institute for Materials Research and Testing* (BAM) for supervising this work. I am very thankful for the great trust in my ideas of the design and development of the UC integrating sphere setup measurement technique. Thanks for her permanent support and motivating words, which helped me finishing this work.

Special thanks to **Dr. Christian Würth** from the BAM, who contributed by discussing the physical processes behind the UC emitters in a critical and constructive manner, which helped to select the best fruits from a manifold of ideas. Unforgettable for me is the time at the first upconversion meeting in Regensburg, where we also later enjoyed the beer tents and fun fair attractions.

Great thanks to **Prof. Dr. Soukka** from the University of Turku for fruitful physical discussions and a friendly cooperation. Many thanks to **Dr. Emilia Palo** for the synthesis of high-quality upconversion nanoparticles with different dopant concentrations, **Dr. Iko Hypänen** for fruitful discussions as well as to **Dr. Rikka Arppe** and **Dr. Satu Lithanen** for a great time in Poland at ICL 2014 in Wroclaw.

A lot of thanks to **Dr. Thomas Hirsch** from the University of Regensburg and his former workgroup members: **Prof. Dr. Stefan Wilhelm** for the synthesis of bright upconversion particles in different solvents and **Dr. Josef Heiland** for his assistance for the characterization of the excitation beam profiles.

Great thanks to all former and current work group members from the Biphotonics group (BAM) of Dr. Ute Resch Genger for the good working atmosphere:

Thanks to **Dr. Jutta Pauli** for introducing me to the spectrometers, **Dr. Katrin Hoffmann** for friendly chats, **Arne Güttler** for technical help, **Nils Handelsmann** for programming, **Dr. Markus Grabolle** for fruitful physical discussions and always having an

## Acknowledgement

---

open ear and **Dr. Soheil Hatami** for lunch times, sharing office lab work and sharing frustrations. A lot of thanks to **M.Sc. Florian Frenzel** and **M.Sc. Florian Weigert** for nice conversations. Thanks to **Dr. Marco Kraft** for finding the reason for the seeming avalanche effect measurement artefact, for the  $\Phi_{UC}$  measurements of the  $\text{Yb}^{3+}$ ,  $\text{Er}^{3+}$  concentration series, and a great time in Poland at the ICL 2014. Thanks to **M.Sc. Bettina Grauel** for providing me with the Matlab program for the rate equation analysis and thanks to **M.Sc. Melissa Monks** for doing ICP-OES measurements. Many thanks to **Dr. Daniel Geißler**, **Dr. Christian Würth** and **M.Sc. Bettina Grauel** for careful proof reading of this thesis.

Also many thanks to all former and current work group members from the group of Prof. Dr. Hoffmann for helpful feedbacks and a nice atmosphere:

Thanks to **Dr. Christian Nenstiel**, who was a great help with UC lifetime measurements with the dye laser as well as to **Dipl. Phys. Dipl. Kfm. Thomas Kure** and **Dr. Felix Nippert** for nice chats and good advice. Great thanks to **Dr. Maximilian Ries** being a great help with the last corrections of my PhD presentation. Special thanks to **Dr. Max Bügler** for his good friendship and the exciting billiard matches.

A lot of thanks to my close friends **David, Einar, Fabian, Jan, Loic, Max, Murat and Rachel** for always having an open ear for me, helping me in difficult situations and having good times together.

Special thanks to **my mother Petra** for her great support. Huge thanks to **my daughter Sophie** giving me inner strength and a high motivation to achieve my goals.

## Contributions to the Manuscripts

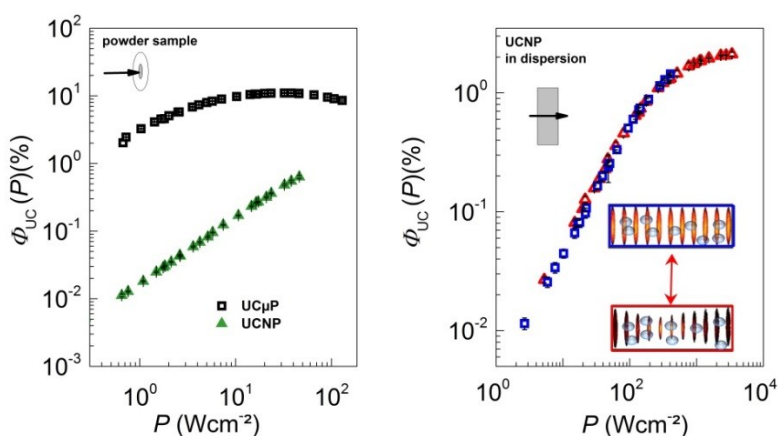
### Publication I

#### Manuscript Title:

Power-dependent upconversion quantum yield of  $\text{NaYF}_4:\text{Yb}^{3+},\text{Er}^{3+}$  nano- and micrometer-sized particles – Measurements and simulations

#### List of Authors:

Martin Kaiser, Christian Würth, Marco Kraft, Iko Hyppänen, Tero Soukka, Ute Resch-Genger



#### Substantial contributions:

A newly custom-built integrating sphere setup was designed, built up and calibrated. I performed all measurements including excitation power density-dependent absolute upconversion luminescence (UCL), upconversion quantum yield ( $\Phi_{\text{UC}}$ ), and lifetime measurements, did the analysis of the data and created all graphics. New approaches for the analysis of the data as  $P$ -dependent slope factor and relative contribution were developed. I experimentally realized and characterized the Top Hat and Gaussian beam profiles. I validated the experimental results with respect to the influence of the beam profile on  $\Phi_{\text{UC}}$  with theoretical simulations by using the formula of the Andersson-Engels group for ideal biphotonic converters. I wrote the manuscript in close corporation with Dr. Ute Resch-Genger and Dr. Christian Würth.



## Publication II

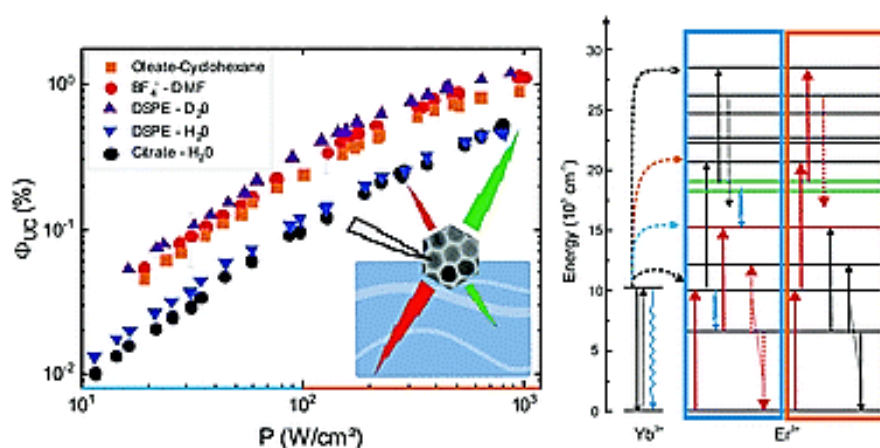
### Manuscript Title:

Excitation power dependent population pathways and absolute quantum yields of upconversion nanoparticles in different solvents

### List of Authors:

Christian Würth\*, Martin Kaiser\*, Stefan Wilhelm, Bettina Grauel, Thomas Hirsch, Ute Resch-Genger

*\*Equally contributed*



### Substantial contributions:

I performed all measurements including excitation power density-dependent absolute upconversion luminescence (UCL), upconversion quantum yield ( $\Phi_{UC}$ ), and lifetime measurements. I developed a  $\Phi_{UC}$  measurement strategy for upconversion nanoparticles (UCNPs) dispersed in water and did the analysis of all  $\Phi_{UC}$  and lifetime data and created many of the graphics of the manuscript. Interpretations of the luminescence quenching and change in the luminescence emission band ratios were concluded with Dr. Christian Würth. I proposed that the increasing green-to-red intensity ratio at low  $P$  is an argument for the population of the red emissive  $^4F_{9/2}$  energy level via  $^4I_{13/2}$  level. I drafted the paper in close corporation with Dr. Christian Würth and Dr. Ute Resch-Genger.

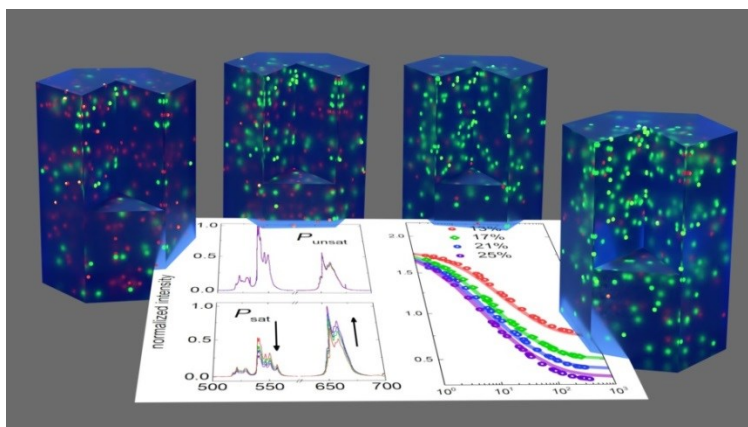
### Publication III

#### Manuscript Title:

Explaining the influence of dopant concentration and excitation power density on the luminescence and brightness of  $\beta\text{-NaYF}_4\text{:Yb}^{3+},\text{Er}^{3+}$  nanoparticles: Measurements and simulations

#### List of Authors:

Martin Kaiser, Christian Würth, Marco Kraft, Tero Soukka, Ute Resch-Genger



#### Substantial contributions:

I guided Marco Kraft at measuring the excitation power density-dependent absolute upconversion luminescence (UCL) and upconversion quantum yield ( $\Phi_{\text{UC}}$ ) for the differently doped  $\beta\text{-NaYF}_4\text{:Yb}^{3+},\text{Er}^{3+}$  nanoparticles. I performed all luminescence lifetime measurements, did the analysis of all data, and performed a rate equation analysis with a 9-level  $\text{Er}^{3+}$  rate equation model. I did the photophysical interpretation, which was discussed with Dr. Christian Würth. I wrote the manuscript in close corporation with Dr. Ute Resch-Genger.